LEIBNIZ-INSTITUTE OF ATMOSPHERIC PHYSICS

CUMULATIVE DISSERTATION

for the degree of

Doctor rerum naturalium (Dr. rer. nat.)

at the Faculty of Mathematics and Natural Sciences,
University of Rostock, Germany

Lidar observations of the Fe layer and temperatures in the polar mesopause region

by

Timo P. Viehl

Leibniz-Institute of Atmospheric Physics (IAP)
at the University of Rostock in Kühlungsborn, Germany

Abstract: Lidar observations of the mesospheric Fe layer and temperatures have been performed at Davis, Antarctica (69°S) and ALOMAR, Norway (69°N). Large-scale transport is the primary cause of the seasonal variation of the Fe layer, which shows a dynamic uplift during the summer months. An uptake of metal atoms on ice particles, as well as temperature-dependent chemistry, play secondary roles for the seasonal variation. The regular bottomside extension of the Fe layer in the upper mesosphere and lower thermosphere (MLT) is caused by the direct photolysis of FeOH ($J(\mathrm{FeOH}) = (6\pm3)\,10^{-3}\,\mathrm{s}^{-1}$). Temperature and Fe density observations reveal unexpectedly strong tidal modulations in the polar MLT of up to ±6 K and ±40%, respectively. In the Southern Hemisphere, the MLT can experience sudden mesopause jumps in early summer, leading to an elevated summer mesopause with very low temperatures. These changes to the global meridional circulation cause significant hemispheric differences in the occurrence of mesospheric ice particles observable as PMC/NLC or PMSE.

Schlossstr. 6
18225 Kühlungsborn
Germany

IAP Kühlungsborn
6 February 2017
IAP-No. 49/2017
ISSN 1615–8083

urn:nbn:de:gbv:28-diss2017-0074-3

Universität Rostock

Traditio et Innovatio

Lidar observations of the Fe layer and temperatures in the polar mesopause region

by
Timo P. Viehl

This scientific report has been accepted as a dissertation at the
Faculty of Mathematics and Natural Sciences, University of Rostock, Germany.

Reviewer: Prof. Dr. Franz-Josef Lübken
Leibniz-Institute of Atmospheric Physics (IAP), University of Rostock,
Kühlungsborn, Germany

Prof. Dr. Otto Schrems
Alfred-Wegener-Institute (AWI), Helmholtz-Centre for Polar and Marine Research,
Bremerhaven, Germany

Submitted: 28 October 2016
Public defence: 27 January 2017

Science is the one human activity that is truly progressive.
The body of positive knowledge is transmitted from generation to generation.

—Edwin P. Hubble, 1936

Preface

The region of the upper mesosphere and lower thermosphere (MLT) has unique physical and chemical characteristics. MLT observations at polar regions, in particular, allow drawing far-reaching conclusions about the physics and chemistry of the whole system of Earth's atmosphere. Recent international and national programmes such as SCOSTEP's scientific project "Role of the Sun and the Middle Atmosphere in Climate" (ROSMIC) or the Leibniz Association's Senate Competition project "Mixing and Turbulence in the Mesosphere and Lower Thermosphere" (MaTMeLT) emphasise the importance of such investigations.

Of particular interest in these middle atmospheric research programmes are the coupling of atmospheric layers and the role of the upper layers in global climate models. The quantification of the solar variability and its importance for long-term variations in the middle atmosphere, trends in the thermal and dynamical structure, as well as atmospheric composition, can provide crucial information to the overall system of the atmosphere.

High-resolution observations, as presented in this thesis, provide insights into the dynamical coupling of atmospheric layers through gravity waves and tides, the effects of middle atmospheric circulation on the lower atmosphere, and trends in dynamic coupling. Such observations help to determine to what extend the middle atmosphere can have an influence on the climate through a change in dynamics, the radiative budget, and chemistry, or how it can be used as a proxy to monitor lower atmospheric processes and anthropogenic climate change.

This thesis presents results obtained from high-resolution lidar observations at polar latitudes, which are of particular importance for the whole system of Earth's atmosphere. Their exemplary location in the global circulation, as well as a lack of observations due to the inaccessibility and difficult environmental conditions, place the polar regions among the last frontiers in atmospheric science.

Observations with the mobile IAP Fe lidar provide temperatures, metal layer densities, and aerosol data in the particularly inaccessible MLT region. The continuous observations are among the most accurate measurements with high resolution in the middle and upper atmosphere. Modern resonance lidar systems can be further used to study a variety of other topics, such as the mixing of trace species. Although mesospheric metals have been observed by different means for several decades, some aspects of their dynamics and chemistry are still unknown. Several dynamical and chemical features of the MLT region (in particular at polar latitudes) and the whole atmosphere will in the near future be understood significantly better through an enhanced understanding of the mesospheric metals. The results of this thesis enable to understand the physics and chemistry of the MLT region better and to improve the knowledge about the middle atmosphere in the global context.

An integral part of the doctoral research summarised in this thesis has been the preparation and execution of two major measurement campaigns with the mobile IAP Fe lidar to Antarctica and the Arctic. In addition to the expeditionary preparation in Germany and Australia, this involved two journeys to Antarctica, including three summer seasons and one winter (a total of around 22 months) at Davis Station. On one hand, such measurement campaigns require routine observations, instrument and infrastructure maintenance and improvement, and ongoing data analyses. On the other hand it is necessary for all expeditioners at a mid-sized station with year-round personnel such as Davis to help out with other experiments and projects, and to keep the general station alive.

The expeditions have not only been truly invaluable experiences but yielded a series of new insights and surprising observations. The analyses of the observations are still ongoing, but several important results have already been published in peer-reviewed journals. 9 of these articles are cumulatively submitted in this thesis. The *Manuscripts* of the publications are an integral part of this doctoral research.

This thesis additionally provides a review of the scientific subject and the results. The *Introduction* gives an overview of middle atmospheric science related to this work (Section 1), summarises important aspects about mesospheric metals and the Fe layer in particular (Section 2), describes the instrument and its capabilities (Section 3), and gives a brief overview of the measurement campaigns conducted (Section 4).

The *Summary of Results* describes the methods and results of the studies, and puts them into the context of the relevant literature. Sections 5 to 8 primarily deal with the chemistry of the mesospheric metals. Sections 9 to 11 discuss the influence of ice particles, temperatures, and transport on the Fe layer. Sections 12 and 13 present observations and model calculations of thermal tides in temperatures and metal densities in the MLT region. Sections 14 to 18 reveal insights into the coupling of atmospheric layers. These observations enable a new understanding of the winter to summer transition of the MLT region at polar latitudes. Together, these results obtained by a single instrument (as well as the comparison of the datasets with other instruments and models) have significantly enhanced our understanding of the chemistry and the dynamics of the MLT region. They have additionally provided new insights into the coupling of atmospheric layers, as well as hemispheric differences of the atmosphere.

Selected *Further Results* of the measurement campaigns, which have not yet been published, are briefly discussed in Sections 19 to 24, and concluded by an *Outlook* of ongoing and future measurements, as well as some important technical developments. A list of abbreviations, measurement statistics, chemical rate coefficients relevant to the mesospheric Fe layer, and copyright licenses are given in the *Appendix*. *References* are listed in the back of the thesis.

It is not possible to personally acknowledge all helping hands of the polar expeditions leading to the results presented here. The most significant contributions are summarised in the *Acknowledgement*.

Timo P. Viehl
October 2016

Table of Contents

Short Summary of Papers

This thesis is submitted as a cumulative work of papers published in peer-reviewed journals. The following pages give a short overview of the contributing papers authored by the candidate. Citations to these papers are given in ***bold*** throughout the text. The manuscripts are part of this thesis and collected on pages 63 to 126.

Viehl et al. [2016a]

The photolysis of FeOH and its effect on the bottomside of the mesospheric Fe layer

Viehl, T. P., *J. M. C. Plane, W. Feng, and J. Höffner*

Geophys. Res. Lett., *43*, 1373–1381, (2016)

Lidar observations of a mesospheric metal are for the first time combined with quantum chemical calculations and a 3D atmospheric chemistry model to derive an unknown photolysis rate. The inclusion of this photolysis rate leads to a considerable improvement in the ability of atmospheric chemistry models to describe the diurnal behaviour of the Fe layer. The results explain the regular bottomside extension of the Fe layer in the MLT region which is primarily caused by the direct photolysis of FeOH. Reactions of FeOH with H play a subordinate role. FeOH is depleted during polar summer. This may have implications for the formation and composition of meteor smoke particles.

Viehl et al. [2015]

Summer time Fe depletion in the Antarctic mesopause region

Viehl, T. P., *J. Höffner, F.-J. Lübken, J. M. C. Plane, B. Kaifler, and R. J. Morris*

J. Atmos. Solar-Terr. Phys., 127, 97–102, (2015)

Ice particles were previously thought to be a major cause of the seasonal change in Fe densities at polar latitudes. Lidar and radar observations at Davis, Antarctica show an anti-correlation of ice particle occurrence and Fe density. The centroid altitude of the Fe layer rises due to a dynamic uplift of the whole layer by vertical winds and not due to a scavenging effect of ice particles at lower altitudes. The temperature dependence of mean Fe densities during a very strong and unexpected depletion observed around summer solstice suggests that gas-phase chemical reactions have a dominating effect. An attempt is made to explain the substantial depletion around summer solstice with a simplified gas-phase chemistry partitioning between Fe and FeOH.

Viehl et al. [2016b]

Corrigendum to: Summer time Fe depletion in the Antarctic mesopause region, by Viehl et al. [2015]

Viehl, T. P., *J. Höffner, F.-J. Lübken, J. M. C. Plane, B. Kaifler, and R. J. Morris*

J. Atmos. Solar-Terr. Phys., 142, 150–151, (2016)

Due to a mathematical error, ***Viehl et al.*** [2015] incorrectly concluded that a simple gas phase chemistry scheme could explain the strong Fe depletion at Antarctic latitudes around the summer solstice. The correction of the mistake can no longer justify this conclusion, under the assumptions and simplifications made. Hence, vertical and horizontal transport must explain the depletion, also shown in the observed uplift of the layer. Simulations with an atmospheric chemistry model support this new interpretation.

Lübken et al. [2011]

First measurements of thermal tides in the summer mesopause region at Antarctic latitudes

Lübken, F.-J., J. Höffner, ***T. P. Viehl****, B. Kaifler, and R. J. Morris*

Geophys. Res. Lett., *38*, L24806, (2011)

Measurements with the mobile IAP Fe lidar have detected thermal tides in the summer polar mesopause region. These tides are much larger than existing model simulations predict, with modulations in temperature up to ±6 K and Fe number densities up to ±40%. Temperature tides show a semidiurnal and diurnal structure at different altitudes. In Fe densities, a strong diurnal tidal component seems to dominate at all altitudes. The downward tidal phase progression in temperatures and Fe densities is similar and correspond to vertical wavelengths of 30 km and 36 km, respectively.

Feng et al. [2015]

Diurnal variation of the potassium layer in the upper atmosphere
*Feng, W., J. Höffner, D. R. Marsh, M. P. Chipperfield, E. C. M. Dawkins, **T. P. Viehl**, and J. M. C. Plane*
Geophys. Res. Lett., *42*, 3619–3626, (2015)

Measurements of K atoms in the MLT at mid-latitudes in Kühlungsborn, Germany are compared to the 3D atmospheric chemistry model WACCM-K. Amplitude and phase of the diurnal and semidiurnal tide are captured well, even though some discrepancies between the model and the observations persist. The temperature influence is presumably not significant because of the chemistry of K. However, direct temperature comparisons are not yet possible.

Kaifler et al. [2015]

Lidar observations of gravity wave activity in the middle atmosphere over Davis (69°S, 78°E), Antarctica
*Kaifler, B., Lübken, F.-J., J. Höffner, R. J. Morris, and **T. P. Viehl***
J. Geophys. Res.: Atmos., *120*, 4506–4521, (2015)

Lidar observations in the stratosphere and the upper mesosphere and lower thermosphere (MLT) region at Davis, Antarctica are used to investigate gravity wave activity. The gravity wave potential energy density (GWPED) has a large seasonal variation with a semiannual oscillation in the MLT, consistent with selective critical-level filtering in the lower stratosphere. The identical structure of the MLT and stratosphere suggest that the wind field near the tropopause level controls the gravity wave flux reaching the MLT region.

Morris et al. [2012]

Experimental evidence of a stratospheric circulation influence on mesospheric temperatures and ice-particles during the 2010–2011 austral summer at 69°
*R. J. Morris, J. Höffner, F.-J. Lübken, **T. P. Viehl**, B. Kaifler, and A. R. Klekociuk*
J. Atmos. Solar-Terr. Phys., 89, 54–61, (2012)

First IAP Fe lidar temperature measurements in the mesopause region at Davis, Antarctica are compared to the occurrence of ice particles detected as polar mesosphere summer echoes (PMSE) and the breakdown of the polar vortex. The timing of the annual breakdown of the southern polar stratospheric vortex seems to influence mesopause temperatures and the formation of PMSE early in the austral summer. Temperatures below mesopause altitudes in the 2010/2011 austral summer were unusually high.

Lübken et al. [2014]

Winter/summer mesopause temperature transition at Davis (69°S) in 2011/2012
*Lübken, F.-J., J. Höffner, **T. P. Viehl**, B. Kaifler, and R. J. Morris*
Geophys. Res. Lett., *41*, 5233–5238, (2014)

Quasi-continuous Fe lidar measurements at Davis, Antarctica are presented for the austral summer season 2011/2012. Mesopause altitudes and temperatures are similar to the Northern Hemisphere (NH) after the initial transition from the winter to the summer state. A significant elevation of the mesopause for a short period around the solstice follows the initial downward shift of the mesopause during the winter/summer transition. The mesopause is then higher and colder than typical NH values by ∼4 km and 10 K. Individual profiles show temperatures as low as 100 K. The temperature transition strongly correlates with zonal winds in the stratosphere. However, the impact of stratospheric winds on the occurrence of ice particles seems to be more complicated than previously assumed.

Lübken et al. [2015]

Winter/summer transition in the Antarctic mesopause region
*Lübken, F.-J., J. Höffner, **T. P. Viehl**, E. Becker, R. Latteck, B. Kaifler, D. J. Murphy, and R. J. Morris*
J. Geophys. Res.: Atmos., *120*, 12,394–12,409, (2015)

Temperature data obtained by the IAP Fe lidar in the Antarctic MLT are of unprecedented accuracy and resolution, and available for three consecutive seasons with a surprisingly different summer mesopause structure. The analysis of MF radar winds and PMSE ice particle detection shows that the occurrence of an 'elevated summer mesopause' (ESM) in some years is not only caused by changing breakdown conditions of the polar vortex, as previously thought. In such years, mesospheric winds are also shown to be relevant for the propagation of gravity waves and the subsequent shift in temperatures. Furthermore, comparison with results of a general circulation model shows that the filtering of gravity waves alone cannot explain the ESM. It is important to take the spectrum of gravity waves is into account to explain this feature of the MLT region.

Introduction

The following Sections 1 to 4 give a brief introduction in the scientific subject of this thesis, some technical details of the instrument and the data retrieval, and basic information about the two measurement campaigns to the polar regions of both hemispheres during which the observations were obtained. For more comprehensive information refer to the cited literature.

1 Earth's atmosphere

The atmospheric region of the upper mesosphere and lower thermosphere (MLT) has unique physical characteristics. Observations at polar latitudes allow drawing interesting conclusions about the physics and chemistry of the whole atmosphere. However, accurate observations with high resolution are challenging and still rare in the polar MLT region.

Earth's atmosphere can be divided into different altitude layers in relation to several physical characteristics. A common classification can be carried out according to the temperature structure. With increasing altitude, these layers are the troposphere, stratosphere, mesosphere, and thermosphere, which are separated by the tropopause, stratopause, and mesopause (Figure 1; for more details see *Houghton* [2002], *Schumann* [2012], *Brekke* [2013], or other atmospheric physics textbooks). The region of the stratosphere and mesosphere is often called the "middle atmosphere".

The wider area around the mesopause between approximately 70 km and 110 km altitude is referred to as the region of the upper mesosphere and lower thermosphere (MLT). For meteoroids entering Earth's atmosphere, air densities in the MLT become sufficiently large (around 0.001 hPa) to evaporate material through frictional heating. This evaporation creates layers of metal atoms such as the iron (Fe) layer. The Fe layer usually occurs between around 75 km and 100 km altitude and can occasionally extend down below 70 km and up to above 120 km altitude (see Figure 1 and Section 2).

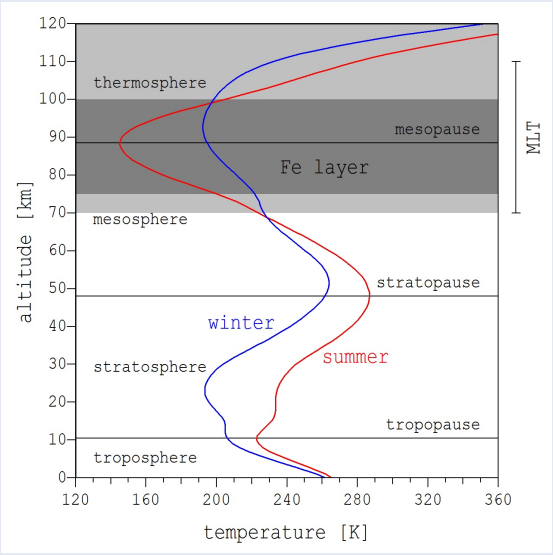

Figure 1: Earth's atmosphere. Different altitude levels can be classified according to the temperature structure. During summer (red), temperatures at the mesopause are lower than during winter (blue). Layers of metal atoms such as Fe are created through meteoric ablation in the region of the upper mesosphere and lower thermosphere (MLT) between approximately 75 and 100 km altitude (dark grey). The Fe layer can occasionally extend down below 70 km; Fe atoms are further observed in sporadic layers in the thermosphere above 100 km (light grey). *Temperature data from NRLMSISE-00* [*Picone et al.*, 2002]. *CC BY 4.0*

The MLT further exhibits a variety of unique physical and chemical processes and is therefore of particular interest for a broad branch of modern atmospheric research [*Smith*, 2012]. For example, temperatures in the MLT are generally lower during summer than during winter. This phenomenon is important for the understanding of the whole Earth atmosphere's dynamics. The polar MLT is also the home of the highest clouds on Earth (NLC, see Section 1.3). A potential extension of these ice clouds to lower latitudes as well as an increase in their brightness has been proposed as an indicator for a cooling of the MLT as well as an increase in water vapour levels through the photolysis of enhanced levels of methane (CH_4) [e.g., *DeLand and Thomas*, 2015; *Berger and Lübken*, 2015; *Hervig et al.*, 2016]. Both phenomena are directly linked to an increase

in greenhouse gases, which are associated with global warming in the troposphere.

1.1 The MLT region

Several reviews have outlined the current knowledge about the MLT and list open scientific questions [e.g., *Becker*, 2012; *Feofilov and Kutepov*, 2012; *Sinnhuber et al.*, 2012; *Smith*, 2012; *Plane et al.*, 2015]. The following sections summarise important physical and chemical aspects and concepts of the MLT which are relevant for this thesis.

Temperature anomaly

Temperatures in the polar summer MLT are lower than during winter although the solar irradiance is higher (Figures 1 & 2). In fact, temperatures during summer deviate by more than 100 K from a hypothetical state of radiative equilibrium of the atmosphere in which dynamical factors are neglected. Temperatures around summer solstice can fall below 100 K (–173°C) [e.g., ***Lübken et al.***, 2014], making the polar summer MLT the coldest naturally occurring place on Earth. The low summertime temperatures are caused by atmospheric waves which break in the mesopause region and cause a strong upwelling at polar latitudes (Section 1.2).

Major reactive chemical species

Solar electromagnetic radiation and energetic particles cause the photolysis and photoionisation of atmospheric constituents in the MLT and the higher atmosphere. Atomic oxygen (O) is the most important reactant in the MLT. Atomic O is created through the photolysis of the oxygen molecule (O_2) in the UV band below 242 nm, as well as through collisions with cosmic particles with energies larger than 5.2 eV. The concentration of atomic O controls many important chemical reactions in the MLT region, either directly, or indirectly through removal of ozone (O_3) or by controlling the creation of the odd-hydrogen (HO_x) radicals atomic hydrogen (H), hydroxyl (OH), and hydroperoxyl (HO_2).

The rate-determining step of the removal of atomic O is given through the recombination forming O_3 in collisions with O_2. This reaction is pressure dependent as it needs a moderating third body to carry excess collision energy and hence varies with $[O_2]^2$ at its low-pressure limit [*Plane et al.*, 2015].

The pressure range at higher MLT altitudes above ~90 km (<0.001 hPa) is too low for an efficient formation of O_3. Any O_3 found in this pressure range was primarily formed at lower altitudes and transported upwards through diffusive processes.

Atomic O has a pronounced diurnal variation below 80 km altitude, where it essentially disappears at night. However, there is nearly no diurnal variation above 84 km, where the time constant for the removal exceeds 12 h due to the low pressure and hence comparatively low amounts of molecular oxygen [O_2] [*Plane et al.*, 2015]. The exact representation of this atomic O shelf is important for atmospheric models analysing chemical reactions and the radiative budget in the MLT [e.g., *Feofilov and Kutepov*, 2012; ***Viehl et al.***, 2016a]. The absence of daytime photolysis causes a 10-fold increase of [O_3] throughout the MLT during the night [*Plane et al.*, 2015]. The increase of [O] and the decrease of [O_3] with altitude causes an inversion of the ratio [O]/[O_3] at around 75 km, with [O]/[O_3] then rapidly increasing from ~10 at 80 km to ~100,000 at 110 km altitude.

The large-scale upwelling at the summer poles (see Figure 2) transports minor constituents such as methane (CH_4) to the upper atmosphere. The photolysis of CH_4 by Lyman-α radiation at 121.6 nm (penetrating down to about 80 km altitude) and subsequent reaction with O_2 is the primary source of water vapour (H_2O) in the MLT region. As a result of the seasonal cycle of the residual meridional circulation and CH_4 upwelling, [H_2O] in the MLT increases by a factor of 3 from winter to summer and allows for sufficient growth of mesospheric ice particles during the summer months.

In the MLT, atomic H is primarily created through photolysis of H_2O at wavelengths shorter than 240 nm, as well as through the reaction of atomic O with H_2O. The resulting diurnal variation of atomic H largely follows the variation of atomic O at daytime concentrations of roughly [H]/[O]~0.01 at around 80 km and [H]/[O]~0.0003 at around 90 km. Particularly on a seasonal level, [H] further follows [H_2O] with a maximum in summer, at ratios of [H]/[H_2O] between ~1 and 10 000 throughout the MLT, increasing to higher altitudes [*Plane et al.*, 2015].

Figure 5 on page 10 and the reactions in Appendix B show the importance of O, H, and O_3 to the chemistry of the Fe layer (also see Section 2.3).

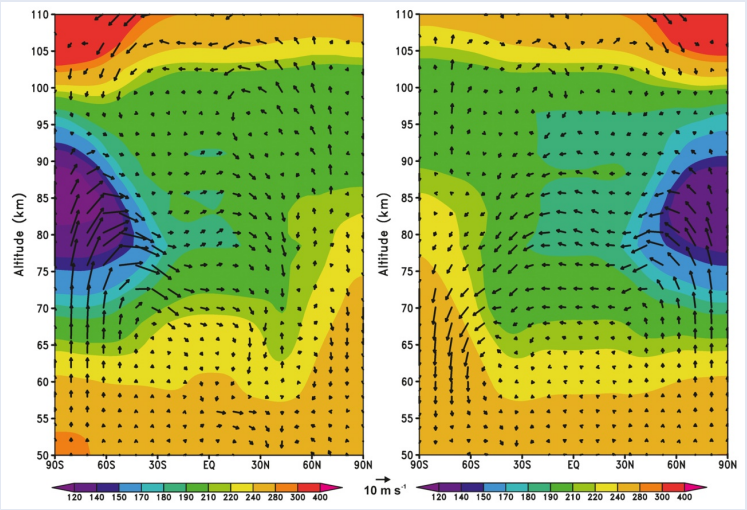

Figure 2: Temperatures [K] and wind vectors [m s^{-1}] in the MLT region for January (left) and July (right), WACCM simulations between 2004 and 2011. The residual circulation is seen in a summer pole upwelling, meridional transport at around 80 km altitude and winter pole downwelling. Adiabatic cooling of expanding air masses causes very low mesopause temperatures above the summer pole. Vertical wind components are multiplied by a factor of 500 to be comparable with meridional winds. *Reprinted from Plane et al.* [2015, Fig. 1], *Copyright 2015 American Chemical Society.*

1.2 Important waves in the MLT

Various atmospheric wave phenomena are important for the dynamic state of the MLT region [e.g., *Holton*, 2004; *Smith*, 2012]. For the scope of this thesis, gravity waves and thermal tides are of particular importance. The knowledge about both wave phenomena grows continuously and cannot be summarised here in its entirety. The following only lists some basic principles relevant to the discussions and conclusions in this thesis.

Gravity waves

Gravity waves are transversal atmospheric waves, with buoyancy acting as the restoring force. In the MLT, they are usually observed as variations in temperature, winds, or the movement of tracers such as ice particles or gradients in mesospheric metal layers. *Fritts and Alexander* [2003] have compiled a comprehensive review of gravity waves and their dynamics in the middle atmosphere.

Gravity waves are excited, for example, when air parcels are vertically displaced in the atmosphere and then restored in statically unstable conditions (i.e. the real atmospheric temperature gradient dT/dz is larger than the adiabatic lapse rate). Gravity waves, therefore, have intrinsic periods larger than the Brunt-Väisälä period, which depends on the temperature gradient and is around 5 min to 10 min throughout the middle atmosphere. On the other end of the spectrum, gravity waves are restricted to periods lower than the Coriolis parameter [e.g., *Fritts and Alexander*, 2003], which is around 13 h at 69° latitude. This shows that gravity waves can have a broad range of wavelengths and phase speeds. Typically, gravity waves have horizontal wavelengths between 100 km and 10 000 km, vertical wavelengths between 4 km and 20 km, and phase speeds between 20 m/s and 200 m/s.

Most atmospheric gravity waves are generated in the troposphere through flow over topographic features, convection, geostrophic adjustment, or wind shear [*Becker*, 2012]. However, secondary gravity waves can also be generated throughout the middle atmosphere, in particular through wave-wave interactions and wave breaking.

Gravity waves can propagate horizontally and vertically, transporting energy and momentum over large distances. When gravity waves propagate upwards, their amplitudes increase with decreasing air density, conserving the energy of the wave. Gravity waves are therefore more pronounced throughout the middle atmosphere than in the troposphere. Typical temperature disturbances of gravity waves are less than ±1 K in the troposphere but can reach more than ±20 K in the MLT.

With growing amplitudes and disturbances of the background temperature, gravity waves can become unstable. This occurs once the temperature gradient reaches the adiabatic temperature gradient and buoyant oscillations are no longer possible. When propagating upwards, gravity waves will therefore always break once they have reached regions of sufficiently low densities. This is commonly the case at MLT altitudes.

From the dispersion relation of gravity waves it follows that the vertical wavelength m is not only proportional to the Brunt-Väisälä frequency N but also to the difference between the background wind u

and the phase speed c, with $m = N/(c\text{-}u)$ [*Fritts and Alexander*, 2003]. This means that the wind field in the middle atmosphere has a significant influence on the breaking and filtering of gravity waves.

The turbulent dissipation of gravity waves in the troposphere and stratosphere is small. However, gravity wave breaking significantly affects the sensible heat budget of the MLT, where the effect is as strong as the net radiative heating [*Lübken*, 1997].

The largest effect of gravity waves in the MLT, however, is their influence on the momentum budget. The resulting residual meridional circulation from the summer to the winter pole causes the low temperatures during the polar summer [*Lindzen*, 1981]: winds in the polar middle atmosphere are predominantly eastward during winter. Gravity waves with eastward phase speeds are therefore mainly filtered before they reach the MLT. During the winter/summer transition, the zonal-mean zonal winds decrease and become westward. Gravity waves with eastward phase speeds can then propagate through the middle atmosphere and break in the MLT after becoming unstable. Gravity waves with westward phase speeds are simultaneously filtered in the lower middle atmosphere. The deposition of eastward momentum therefore dominates in the summer MLT. This momentum deposition exerts an eastward drag on the zonal wind. The Coriolis force deflects the resulting zonal wind equatorwards and induces a meridional flow from the summer to the winter pole. A strong upwelling compensates the associated mass flux at the summer pole. Rising air masses experience adiabatic expansion due to the exponentially decreasing air pressure. The resulting strong adiabatic cooling causes the low temperatures observed (Figure 2).

Atmospheric thermal tides

Thermal tides are large scale oscillations of the atmosphere, excited by the periodic diurnal change of solar irradiance around the globe [*Lindzen and Chapman*, 1969]. Tides are observable as variations in temperature, pressure, and horizontal and vertical winds. Although the Moon and the Sun exert a measurable gravitational force on Earth's atmosphere, these gravitational tidal effects are much smaller than tidal effects generated by solar heating. In this thesis, the term "tides" therefore only refers to solar thermal tides. Tidal oscillations have periods which are subharmonics of a solar day and can be grouped into two categories: migrating and non-migrating tides.

Migrating tides have the same phase speeds as Earth's angular velocity. To a stationary observer on the ground they appear to be travelling with the Sun, with their phases depending only on the local solar time but not on longitude. The frequencies of migrating tides equal their zonal wavenumbers, i.e. the 24 h (diurnal) tide has the wavenumber 1, the 12 h (semidiurnal) tide has the wavenumber 2, and so on. Migrating tides are excited by solar absorption of sources independent of longitude, such as tropospheric H_2O or stratospheric O_3 [e.g., *Smith et al.*, 2003b; *Smith*, 2012]. The local generation of tides in the MLT region is assumed to be small compared to the upwards propagating tidal components generated in the troposphere [*Smith et al.*, 2003b].

Non-migrating tides are excited by sources with an anisotropic longitudinal distribution, like convective latent heat release over tropical land masses. They can be further excited through non-linear wave-wave interactions, e.g., between quasi-stationary planetary waves and migrating tides [e.g., *Hagan and Forbes*, 2002, 2003]. The periods of non-migrating tides are also subharmonics of the solar day. However, they can have arbitrary wavenumbers and propagate westwards, eastwards at a phase speed different than the Earth's angular velocity, or be stationary.

Contrary to individual gravity waves, tides are globally present and not significantly affected by mean winds [*Lindzen*, 1981]. In the middle atmosphere, tidal variations in temperature and wind can be substantial and need to be taken into account in global models. Tides interact with other waves such as gravity waves, the Quasi-Biennial Oscillation, or the El Niño-Southern Oscillation [e.g., *McLandress*, 2002; *Gurubaran et al.*, 2005]. Upward propagating tides transport energy and momentum to the MLT. Tides can furthermore lead to significant observational biases for observations restricted to certain local times.

Importantly for the MLT, tides change the vertical temperature gradient of the atmosphere and horizontal wind speeds. These changes affect the breaking conditions for gravity waves and cause an additional influence on the global meridional circulation [e.g., *Fritts and Vincent*, 1987; *Mayr et al.*, 2005b; *Senf and Achatz*, 2011]. In particular, gravity waves with eastward phase speeds, which are re-

sponsible for the residual meridional circulation, can break well below the mesopause region during the eastward tidal phase of the zonal wind [*Becker*, 2012].

Observations by *Pancheva et al.* [2002] show that the dominating modes of the vertical wavelength of the semidiurnal tide are at least 35 km long. The vertical wavelength of the diurnal tide is shorter and only around 25 km long [*Smith*, 2012]. Shorter vertical wavelengths correspond to stronger gradients in temperature and winds. The diurnal tide is therefore expected to interact more strongly with gravity waves than the semidiurnal tide.

1.3 Ice particles in the MLT

Ice particles can form in the MLT when sufficient water vapour and nuclei for heterogeneous nucleation are present, and the temperature drops below the frost point (around 145 K). A common hypothesis for the source of condensation nuclei is the nucleation of meteor smoke particles (MSP) from meteoric material (see Section 2.3). During the polar summer months, water vapour and MSP are assumed to be present in sufficient quantities. The sole criterion for ice particle formation is therefore determined by absolute temperature. Water ice particles can nucleate around MSP under these conditions, forming the highest clouds in Earth's atmosphere at around 83 km altitude [e.g., *Hervig et al.*, 2001; *Rapp and Thomas*, 2006].

Noctilucent Clouds / Polar Mesospheric Clouds

In-situ observations of mesospheric ice particles are technically challenging and only possible with sounding rockets. Knowledge about the ice particles in the MLT has primarily been achieved through observations in the optical range. The best-known phenomenon related to ice particles in the MLT are noctilucent clouds (NLC). When ice particles grow to sufficient sizes (>20 nm), they reflect light in the visible spectrum at sufficient amounts to be detected by various means.

The clouds are high enough to reflect light of the Sun behind the horizon to a ground observer at mid-latitudes during conditions of twilight and darkness (solar elevation between -5 and -15°), illuminating them in the night sky (Figure 3). NLC were first observed and reported two years after the eruption of Krakatoa by *Leslie* [1885] and systematically studied by *Jesse* [1896].

When viewed from space, it becomes apparent that NLC are formed above the summer pole and extend equatorward, reaching mid-latitudes only under favourable conditions. Clouds of ice particles in the polar mesopause region have hence also become known as Polar Mesospheric Clouds (PMC). Studies by *Baumgarten et al.* [2012] have shown quantitatively that PMC and NLC describe the same ice particles, observed by different means.

On short time-scales, mesospheric ice particles act as nearly passive tracers when displaced vertically or horizontally. The formation conditions and the vertical displacement have been employed to study MLT dynamics (through gravity wave analyses) and temperatures [e.g., *Baumgarten and Fritts*, 2014].

Polar Mesosphere Summer Echoes

A further phenomenon related to mesospheric ice particles are Polar Mesosphere Summer Echoes (PMSE). These strong echoes observed with VHF radars are caused by small-scale structures in electron densities on the order of the radar's Bragg scale ($d = \lambda/2$). PMSE require the combined effect of neutral air turbulence, free electrons and charged ice particles [e.g., *Rapp and Lübken*, 2004; *Lübken*, 2013].

Turbulence can create lasting structures in mesospheric ice particle layers. The ice particles can be charged through uptake of free electrons. The presence of comparatively heavy charged ice particles reduces the diffusivity of the considerably lighter electrons. The resulting electron density structures constitute irregularities in the radar refractive index. Radio waves are reflected from the created structures like a grating when the Bragg condition is fulfilled.

Ice particles causing PMSE can usually be smaller than NLC particles and hence be subvisible to satellites or ground-based observers. While NLC usually occur around 83 km altitude (the lower part of the super saturated MLT region), PMSE can extend up to 94 km altitude where they are formed before sedimenting and growing through condensation growth. The reduced diffusivity decouples active neutral air turbulence and the irregularities in electron number density on temporal scales. PMSE therefore last for much longer than the turbulence creating the structures until the ice particles evaporate.

Figure 3: Noctilucent cloud (NLC) observed in north-eastern direction above Rostock, Germany (54°N, 12°E) on 10 July 2015 at 23:46 LT, solar elevation -12.3°. NLC are ice clouds formed in the MLT region at around 83 km altitude during the summer months when temperatures fall below ~ 145 K. When ice particles have grown to radii $\gtrsim$ 20 km they can reflect light from the sun below the horizon to a ground observer at mid-latitudes, making them shine at night. *CC BY-NC 4.0*

The radar echoes associated with PMSE hence give an indication of temperatures below the frost point, even in the absence of other observations. It must be noted though that low temperatures are only a necessary, but not sufficient, criterion for the observation of PMSE. The absence of PMSE must therefore not necessarily mean that temperatures are too high, but could be caused by a lack of free electrons or turbulence.

Observations of mesospheric ice particles are presumably the longest lasting observations in the MLT region. Trends analyses of their occurrence rates and geographic extension can, therefore, be used to study the long-term evolution of temperatures in the upper middle atmosphere [e.g., *DeLand et al.*, 2006, 2007]. Observations of the onset of ice particles in early summer measured as PMC or PMSE have furthermore been used to investigate the transition from the winter to the summer state of the polar MLT [e.g., *Karlsson et al.*, 2011]. However, as Sections 15 to 18 of this thesis show, processes are more complicated than previously assumed.

Heterogeneous chemistry of mesospheric ice

Ice particles in the MLT region interact with ambient chemical species. They can act as catalysts and change the composition of trace species, in particular of oxidants such as atomic O, O_3, and HO_x [*Thomas*, 1991]. Most importantly in the scope of this thesis, ice particles heterogeneously interact with the gas-phase mesospheric metal layers and can cause a scavenging uptake effect, lowering metal atom densities [e.g., *Plane et al.*, 2004; *Lübken and Höffner*, 2004; *Gardner et al.*, 2005].

Gardner et al. [2011] proposed this interaction as a qualitative explanation for differences in Fe layer observations at two Antarctic stations. However, to employ mesospheric metal layers for analytic purposes, the uptake effect needs to be quantitatively understood. Changes in metal layer densities can otherwise not be attributed to transport and dynamic displacements, temperature dependent (homogenous) gas-phase chemistry, or interactions with reactive species and charge transfer effects.

Laboratory and model investigations indeed point to discrepancies to the reported Fe layer depletions. The uptake coefficient of Fe atoms (but not K and Na atoms) on cubic ice has been shown to decrease at very low temperatures [*Murray and Plane*, 2005], and a dominating effect of transport processes for the seasonal variation of the mesospheric Na layer has been shown in model calculations [*Marsh et al.*, 2013b]. Observations by ***Viehl et al.*** [2015, 2016b], presented in Sections 9 to 11 of this thesis, investigate these effects further and conclude that the ice particle uptake effect is negligible for the mesospheric Fe layer.

2 Mesospheric metals

Layers of metal atoms are created in the MLT region as a result of meteoric ablation. They can be efficiently probed by resonance lidars to determine ambient temperatures with high accuracy and resolution. The observation of metal densities further allows the investigation of the physics and chemistry of the MLT region, providing information about cosmic dust input, middle atmosphere dynamics, ionospheric physics, fundamental chemical reactions, and the formation of meteor smoke particles influencing the nucleation of clouds in the middle atmosphere. It is important to understand the morphology and the chemical properties of the metal layers in more detail to achieve these goals.

When meteoroids enter Earth's atmosphere, they vaporise in the altitude region of the MLT due to frictional heating. The process of thermal ablation creates layers of the elements most prevalent in cosmic dust particles (the metals Fe, Mg, Na, K, and Ca as well as the metalloid Si) in atomic form [e.g., *Vondrak et al.*, 2008].

J. M. C. Plane and coworkers have published a series of comprehensive reviews of mesospheric metal studies since 1991 [*Plane*, 1991, 2003; *Plane et al.*, 2015]. The following sections give a brief summary of some important aspects of the origin, chemistry, physics, and observations of mesospheric metals with an emphasis on the Fe layer.

History of observation

Discovered by *Slipher* [1929] through the Na *D*-line emissions ($3^2P_J - 3^2S_{1/2}$) at 589 nm in the atmospheric nightglow, mesospheric metals were first studied with photometers [*Hunten*, 1954; *Hunten and Godson*, 1967] and then with resonance lidar systems (historically called "laser radars") [*Bowman et al.*, 1969]. Lidars proved to be advantageous due to their much higher spatial and temporal resolution as well as longer possible measurement durations than passive photometers, which can only operate during twilight. Moreover, lidar systems soon became able to determine temperatures through the probing of the metal atoms' hyperfine structure, and the derivation of the Doppler broadening of the resonance lines [*Gibson et al.*, 1979; *Fricke and von Zahn*, 1985; *Neuber et al.*, 1988]. A prime objective since then has been to develop more sophisticated lidar systems and acquire even more precise temperature measurements. Today, resonance lidar systems are the most accurate instruments for continuous MLT temperature measurements with high temporal and spatial resolution [e.g., ***Lübken et al.***, 2015].

2.1 Scientific interest

Several scientific topics and physical properties are related to the observations of mesospheric metals. Some important aspects are summarised here. In summary, the investigation of the metal layers can significantly improve our understanding of the thermal, chemical, and dynamic state of the MLT region, and thus the whole atmosphere. Furthermore, many interactions with the neutral and ionised atmosphere, as well as cosmic influences, can be investigated. However, a more detailed understanding of all processes involved is required. Parts of this thesis aim to improve our knowledge of the MLT region by gaining new insights about the mesospheric metal layers.

MLT temperatures

A major driver in the development of resonance metal lidars has been the need to derive temperatures in the otherwise inaccessible but important MLT region of the atmosphere. These temperature measurements have been very successful and provided deep insight into the structure of the MLT region and its dynamics [e.g., *von Zahn et al.*, 1996b; *Lautenbach et al.*, 2008; ***Lübken et al.***, 2011; *Kopp et al.*, 2015].

Cosmic dust evolution and atmospheric input

By comparing the abundances of various metals in the MLT, the composition and evolution of cosmic dust can be investigated. Lidar flux measurements of mesospheric metals are a promising approach to determine the absolute amount of meteoric input [*Gardner et al.*, 2014; *Huang et al.*, 2015]. However, these measurements require certain assumptions concerning the unknown vertical eddy diffusion coefficient, mean vertical winds, and the technical performance of the laser. Additionally, small metal layer density fluctuations on the order of

the laser sampling frequency can cause non-linear deviations from the mean state. An improved understanding of these processes is required.

MLT dynamics

Metal densities can be observed with much higher sensitivity and over a much larger altitude range than temperatures or winds in the MLT region. Metal layers have therefore been used to investigate transport processes and wave phenomena [e.g., *Eska and Höffner*, 1998; *Fricke-Begemann et al.*, 2002; *Fricke-Begemann and Höffner*, 2005; *Marsh et al.*, 2013b; *Suzuki et al.*, 2013] and have revealed unexpectedly strong tidal variations [***Lübken et al.***, 2011], see Section 12.

Gravity wave analyses in the MLT have been successfully performed using NLC observations [*Kaifler et al.*, 2013; *Ridder et al.*, 2016]. However, these ice clouds are only available during the 2 or 3 coldest summer months. In contrast, it is possible to observe metal layers all year round, and the bottomside of the metal layers is very sensitive to gravity wave distortions [***Viehl et al.***, 2016a].

Lidar observations of metal layers can therefore significantly increase the capabilities to study dynamic features. However, metal atoms are not passive tracers but are subject to a variety of temperature-dependent chemical reactions (see review by *Plane et al.* [2015] and the following Sections). It is therefore necessary to gain a thorough understanding of these chemical processes through laboratory studies and combining lidar density observations with the appropriate theoretical modelling.

Abundances of important reactive species

Mesospheric metals interact with reactive species such as atomic O and O_3. These species are important for the radiative budget of the MLT but cannot be easily measured [*Feofilov and Kutepov*, 2012]. By observing metal densities, and combining the observations with model calculations, it might in the future be possible to derive concentrations of atomic O and O_3. Calculating the abundances in this way would improve the understanding of the representation of reactive species in models as well as the influence on the radiative budget of the MLT.

Nucleation of meteor smoke particles

Some of the metal compounds chemically created in the MLT condensate to so-called meteor smoke particles (MSP). These particles are slowly transported to the surface of the Earth and act as nuclei for clouds in the middle atmosphere [e.g., *Hunten et al.*, 1980; *Megner and Gumbel*, 2009]. The formation of MSP is still not well understood, but the investigation of the metal layers is a crucial step in the process [*Plane et al.*, 2015].

Ionosphere physics

Ionised metal species are strongly related to sporadic *E* layers (E_S) in the ionosphere [*Delgado et al.*, 2012]. E_S are thought to be constituted from positively charged Fe and Mg ions, interacting with the Earth's magnetic field and gravity waves or wind shear [*MacDougall et al.*, 2000]. These transient ionisation enhancements influence long distance HF radio communication and can also have an effect on the transmission of GPS signals. However, the formation process of E_S is not yet well understood. The phenomenon cannot be predicted accurately, although a relationship to solar thermal tides is known [e.g., *Haldoupis et al.*, 2004; *Pignalberi et al.*, 2014]. Sporadic layers appear in Fe lidar observations. Sporadic or sudden Fe layers (Fe_S) have been observed to occur with surprising regularity by the mobile IAP Fe lidar at Davis, Antarctica (69°S). The phenomenon has also been observed at ALOMAR, Norway (69°N), but less often. This is briefly addressed in Section 25.

Chemical reaction rates

The metal layers experience a variety of changes through different interactions (chemistry and photochemical effects, ionisation, transport dynamics). This allows investigation of chemical reactions by analysing high-resolution observations. ***Viehl et al.*** [2016a] correlate the change in an external variable (solar insolation) with observed changes in metal layer density. The authors thereby derive chemical reaction rate coefficients which had so far not been deducted successfully in laboratory studies, see Sections 5 & 6.

2.2 Origin

Mesospheric metals are created by the meteoric ablation of cosmic dust particles (meteoroids). The two primary cosmic dust sources are collisions between asteroids in the asteroid belt between Mars and Jupiter as well as the sublimation of comets approaching the Sun [*Ceplecha et al.*, 1998]. The exact amount of the daily cosmic dust input into the Earth's atmosphere is unknown and current estimations range from 5×10^3 kg d^{-1} to 2.7×10^5 kg d^{-1} globally [*Plane*, 2012]. However, it is known that the constant background stream of sporadic meteoroids entering the atmosphere every second causes a much larger average mass influx than even strong meteor showers such as the Perseids and Leonids [*Höffner at al.*, 1999; *Höffner and Friedman*, 2004; *Nesvorný et al.*, 2010]. Most of these constantly entering small meteoroids have masses in the range of 10^{-12} g to 1 g. Of those, particles of around 10 μg and a diameter of ~200 μm provide the largest contribution to the daily mass input [*Plane*, 2012].

Meteoroids entering the atmosphere exhibit very high velocities between 11.5 km s^{-1} for particles in the same orbit as the Earth, and 72.5 km s^{-1} for particles in a retrograde orbit [*Baggaley*, 2002]. Significant frictional heating due to collisions with air molecules then occurs at these velocities when the particles encounter pressures of ~0.001 hPa at around 90 km altitude. Temperatures above the melting point of ~1 800 K are reached, causing the particles to evaporate and create layers of atomic metals [*Vondrak et al.*, 2008]. Particles with a mass of less than 10^{-5} g fully ablate in this process, and only larger particles are deposited on the surface as meteorites [*Flynn*, 2002].

A variety of meteorites are found on Earth, but it is generally assumed that a majority of the meteoroids entering the atmosphere have a composition of ordinary chondrites similar to the orthosilicate olivine, i.e. a complete solid solution from forsterite (Mg_2SiO_4) to fayalite (Fe_2SiO_4) [*Anders and Ebihara*, 1982; *Plane*, 2012]. Hence, the metals Fe and Mg (as well as the metalloid Si) are expected to be the most abundant ablated species in the MLT region, with important minor constituents Al, Ca, Na, Cr, K, Mn, and Ni at a mass ratio of 5–10% relative to Si [*Alpers*, 1993a]. Element ratios satisfactorily matching some of these model predictions have been found in various studies [*Plane*, 2003].

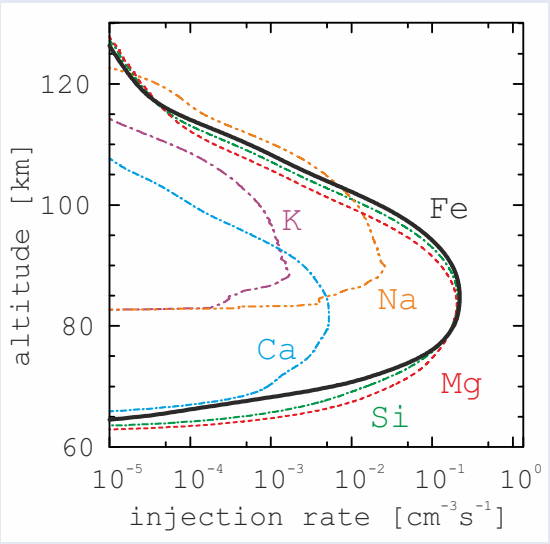

Figure 4: Model calculations of total meteoric injection rates for a distribution of chondritic meteoroids. The most abundant species are Fe, Mg, and Si. The peak of Fe ablation is calculated to occur around 85 km altitude. *Adapted from Vondrak et al.* [2008, Fig. 11], *CC BY 3.0*.

Figure 4 shows results of the Chemical Ablation Model (CABMOD) by *Vondrak et al.* [2008] for expected meteoric injection rates of chondritic meteoroids with masses from 5×10^{-18} g to 5×10^{-3} g entering the atmosphere at velocities of 11.5 km s^{-1} to 72.5 km s^{-1}. The peak injection rates of the abundant elements are calculated to occur around 85 km altitude. The shape of the resulting atomic layers will have a slightly different altitude distribution, as the elements are not only subject to dynamic transport and mixing processes, but also to rapid chemical reactions [e.g., *Alpers et al.*, 1993b].

2.3 Chemistry

Nearly all results presented in this thesis have been obtained from the analysis of Fe lidar observations. A brief introduction to the basic gas-phase chemistry of mesospheric Fe (see Figure 5) will allow a better understanding of these results. The following simplified discussion follows a more detailed analysis by *Plane et al.* [2015] and focusses on the aspects relevant to this work.

Laboratory studies have provided a broad insight into many of the relevant reactions shown in Figure 5 and determined most of the reaction rate coefficients [e.g., *Plane*, 2003; *Self and Plane*, 2003]. The important rate coefficients corresponding to the reactions are listed in Appendix B on page 59.

Fe ion-molecule chemistry

Meteoric ablation creates Fe and Fe^+, with ionisation probabilities ranging between 2% and 80% for meteoroids entering at velocities between 15 km s^{-1} and 70 km s^{-1}, respectively [*Vondrak et al.*, 2008]. Fe can further be ionised to Fe^+ by charge transfer with NO^+ and O_2^+.

Fe^+ can react with O_2 and O_3 to form FeO_2^+ and FeO^+, respectively. However, the reaction with O_2 requires a third body and is thus pressure-dependent. Reaction with O_3 therefore dominates in the lower ionospheric *E* region [*Plane et al.*, 2015]. The abundance of FeO^+ is controlled by reaction with atomic O, which recycles the oxide back to Fe^+. The ratio $[O]/[O_3]$ therefore controls the abundance of the ionospheric species. As $[O]/[O_3]$ is ~100 at 90 km and increases rapidly with altitude, the lifetime of the ionic species increases from a few minutes at 90 km to several days above 100 km. [*Plane et al.*, 2015]. Consequently, FeO^+ becomes a significant ionic reservoir at higher altitudes. This is important, as FeO^+ can be converted to Fe by recombination with e^- a lot more efficiently than Fe^+ [*Bones et al.*, 2015]. Only the efficient pathway $FeO^+ + e^- \longrightarrow Fe + O$ can explain the fast recombination of Fe-containing ions in descending sporadic layers, which can cause strong sudden increases within the metal layer [*MacDougall et al.*, 2000].

Neutral Fe chemistry

Neutral Fe atoms in the MLT region rapidly react with O_3. The lifetime of a neutral Fe atom at 90 km altitude against this oxidation to FeO is on the order of 20 seconds. However, the oxide is recycled back to Fe at nearly every collision with atomic O [*Plane et al.*, 2015]. As [O] is generally more abundant than $[O_3]$ by 1 to 2 orders of magnitude at the peak of the layer at around 87 km, the turnover lifetime is quicker than the subsequent higher oxidations to FeO_2 and FeO_3 (Figure 5 and Table 1). While some higher oxides continuously form, the majority of Fe atoms will hence usually be present in the neutral atomic form.

Reaction with H_2O creates $Fe(OH)_2$ from both FeO and FeO_3, although the second pathway is much more efficient (Figure 5 and Table 1). Subsequent reaction of $Fe(OH)_2$ or FeO_3 with atomic H creates FeOH. *Self and Plane* [2003] conclude that FeOH appears to be the most significant reservoir for

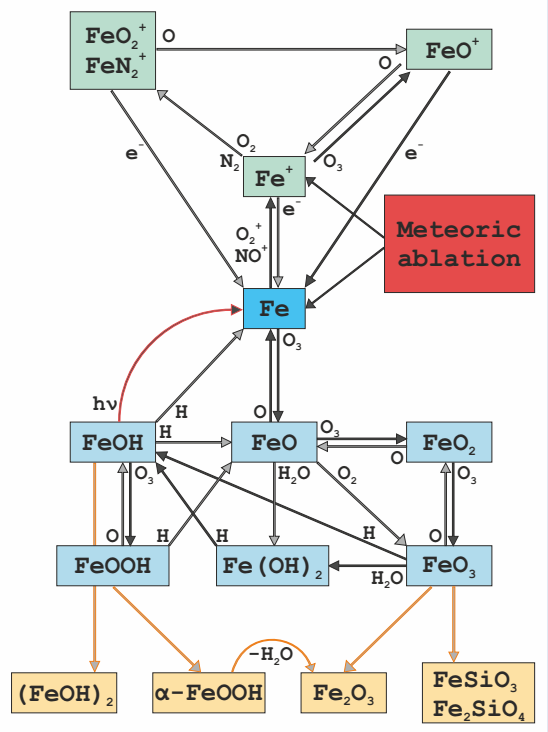

Figure 5: Simplified chemistry schematic of Fe in the MLT region following *Plane et al.* [2015]. Meteoric ablation creates layers of Fe and Fe^+ which react with the neutral and ionised atmosphere, forming oxides and hydroxides. The reactions are temperature dependent and governed by the abundance of atomic oxygen, which further controls the abundances of the reactants $[O_3]$ and atomic [H]. The meteoric influx (source) is compensated by the removal (sink) of Fe atoms through the condensation of meteoric smoke particles (MSP) such as goethite (α−FeOOH), hematite (Fe_2O_3), pyroxene ($FeSiO_3$), and fayalite (Fe_2SiO_4). *CC BY 4.0*

Fe atoms, as the reaction back to Fe has a much higher activation energy than the reactions creating FeOH, and is thus slower in the cold MLT region. The reaction further requires atomic H which is present only at abundances of around 1% of atomic O [*Plane et al.*, 2015]. However, ***Viehl et al.*** [2016a] show that this conclusion is only true under nighttime conditions, as the photolysis $FeOH + h\nu \longrightarrow Fe + OH$ is very efficient (Sections 5 & 6).

The equilibrium between all reactions depends on the ambient temperature and the abundances of atomic O and H as well as O_3. Furthermore, meridional and vertical transport processes can cause considerable deviations from one-dimensional considerations [*Marsh et al.*, 2013b]. Additionally, the Earth's magnetic field can concentrate ionised species in certain regions [e.g., *Höffner*, 1994] and

recombination can then create sudden enhancements in density [*MacDougall et al.*, 2000; *Bones et al.*, 2015]. However, for a given set of atmospheric conditions, mean abundances can be calculated by 3D atmospheric chemistry models employing the reaction rate coefficients in Appendix B.

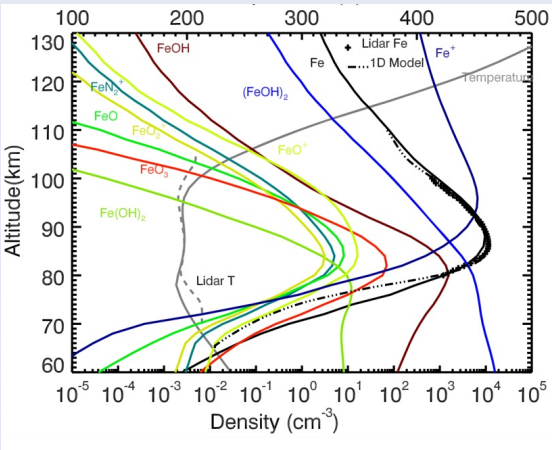

Figure 6: Number densities of Fe, Fe^+, and important oxides and hydroxides. Below 90 km altitude, FeOH is the dominant reservoir from which Fe can be released. At higher altitudes Fe^+ dominates. Model output of WACCM-Fe. *Reproduced from Feng et al.* [2013, Fig. 5], *CC BY 3.0*

Figure 6 shows mid-latitude model calculations by the Fe chemistry version of the Whole Atmosphere Community Climate Model (WACCM-Fe) which was developed by *Feng et al.* [2013]. The peak of the Fe layer (black) occurs around 87 km altitude. Above the peak of the layer, Fe^+ (navy blue) is the dominant species. Below the layer peak, FeOH (maroon) is the main reservoir from which Fe can be released, exceeding the abundance of FeO_3 (red) by at least an order of magnitude. The creation of the dimer $(FeOH)_2$ (medium blue) is parameterised to occur with high efficiency upon every collision of two FeOH molecules. The model treats the dimer as an inert sink, accumulating to lower altitudes.

Although the chemistry of other meteoric metals is similar to Fe in many respects, some aspects differ considerably, in particular for K [*Plane et al.*, 2014]. However, only Section 13 of this thesis briefly deals with K and a detailed understanding of its chemistry is not required in that context. For an in-depth discussion of K and other metals refer to the review by *Plane et al.* [2015] and the references therein.

Meteor smoke particles

Figure 5 shows that the nucleation of stable metal oxides and hydroxides (orange boxes) balances the meteoric input of the metal layers. Such particles formed from meteoric metals have become known as "meteor smoke particles" (MSP) [*Hunten et al.*, 1980]. MSP are important as nucleation seeds for polar mesospheric clouds in the mesopause region [*Turco et al.*, 1982; *Gumbel and Megner*, 2009; *Saunders et al.*, 2010]. On average, it takes the particles around 4 years to reach the Earth surface [*Plane et al.*, 2015]. During winter, however, the residual circulation can rapidly funnel MSP down to the stratosphere, where they reside in the air masses encircled by the polar vortex. Primarily within the stratospheric polar vortex, the particles are thought to interact with sulphuric acid and nitric acid, removing the vapours from the gas phase [*Mills et al.*, 2005; *Saunders et al.*, 2012; *Frankland et al.*, 2015]. Hence, MSP may be not only important condensation nuclei for polar mesospheric ice particles (e.g., noctilucent clouds) but also for polar stratospheric clouds (nacreous clouds).

While investigating MSP nucleation pathways for Fe species, *Saunders and Plane* [2006] note that FeOH can be oxidised by O_3 to form anhydrous iron(III) oxide-hydroxide (FeOOH), see Section 7. The crystalline form α–FeOOH (goethite) has been identified by *Rietmeijer* [2001] as one of the most plausible candidates for MSP. Fe can also form α–Fe_2O_3 (hematite) and add to silica particles and be heterogeneously oxidised to $FeSi_2O_6$ (pyroxene) and Fe_2SiO_4 (fayalite) [*Self and Plane*, 2003]. A possible further sink for Fe is the dimerisation of FeOH, whereafter $(FeOH)_2$ could be picked up by other embryonic MSP.

However, several factors about the nucleation of MSP are still largely unknown. For example, the oxidation of FeOH to form goethite has not yet been investigated under laboratory conditions. A better understanding of these processes is required and can be achieved through further laboratory studies and via the comparison of lidar observations and 3D model calculations.

2.4 Spectral properties and observations

Even the more abundant mesospheric metals have relatively low absolute number densities of around $5{\times}10^2$ cm^{-3} to $5{\times}10^4$ cm^{-3} compared to the am-

bient atmosphere (~6×10^{14} cm^{-3} to 1×10^{12} cm^{-3} in the MLT between 75 km and 110 km altitude). However, their extremely large resonant scattering cross-sections allow efficient detection with ground-based lidar systems [*Alpers et al.*, 1990; *Gardner*, 2004]. Atomic Fe is particularly suited for year-round observation for a variety of reasons:

First, Fe exhibits high abundances in the MLT region, matched only by Mg and Si [*Plane*, 1991]. Second, the lower atmosphere is relatively transparent for the strong Fe resonance lines at 386 nm and 372 nm with a transmissivity of around 35%. In contrast, the resonance lines of Mg at 285 nm or 203 nm, and Si at 251 nm or 221 nm are located in the Hartley bands. They are fully absorbed by atmospheric O_3 and can only be observed from satellites [*Alpers*, 1993a; *Langowski et al.*, 2015]. Third, the linewidth of the resonance scattering of Fe is a lot narrower than the dominant resonance lines of Na at 589 nm or K at 770 nm, for three reasons: (a) the Doppler broadening is wavelength dependent and hence comparatively smaller at lower wavelengths, (b) Fe exhibits a much narrower hyperfine structure than the alkali metals, and (c) the isotope broadening is weaker for Fe [e.g., *Lautenbach and Höffner*, 2004; *Höffner and Fricke-Begemann*, 2005]. Narrower optical filters can therefore be used to observe Fe, which reduces the solar background detected and increases the overall daytime signal-to-noise ratio (SNR) of Fe over Na and K. Finally, the Fe resonance at 386 nm is located in a particularly deep Fraunhofer line, at which the solar flux is considerably low. This further reduces the solar background and increases the SNR, in particular during daylight conditions [*Höffner and Lautenbach*, 2009].

The peak scattering cross-section of Fe is approximately an order of magnitude lower than that of Na [*Gardner*, 2004]. However, because of the reasons listed above, Fe can be observed with a much higher SNR overall. The mesospheric Fe layer has consequently been investigated by several ground-based lidar systems, providing a variety of insights into the physics and chemistry of the MLT region [e.g., *Alpers et al.*, 1990; *Lautenbach et al.*, 2005; *Gardner et al.*, 2011; *Chu et al.*, 2011b; ***Viehl et al.***, 2015].

While Fe is particularly suited to determine temperatures thoughout the full diurnal and seasonal cycle, other metals (mainly Na and K) have also been observed with lidar instruments in order to obtain density and night-time temperature measurements [e.g., *Clemesha et al.*, 1982; *von Zahn and Höffner*, 1996a; *Höffner and Friedman*, 2005; *Höffner and Lübken*, 2007]. Additionally, satellite observations of metal densities (Na, Mg, and K) became available through analyses of OSIRIS/ODIN as well as GOMOS and SCIAMACHY/Envisat measurements [*Fussen et al.*, 2004; *Scharringhausen et al.*, 2008; *Dawkins et al.*, 2014; *Langowski et al.*, 2015]. These observations can provide a unique near-global image of the metal layers and continuous climatological records. However, a fundamental limitation of satellite observations is their reduced vertical and temporal resolution. Several satellite experiments such as OSIRIS/ODIN can provide individual profiles with higher resolution, but published global data is often limited to a spatial resolution of about 10° (geographical) and ~1.7 km vertically, as well as 1-month averages [e.g., *Fussen et al.*, 2010].

The best overall picture of the mesospheric metals can, therefore, be obtained by combining high-resolution lidar measurements with global-scale satellite observations, and by interpreting the observations with models such as WACCM-Fe [*Feng et al.*, 2013].

3 The mobile IAP Fe lidar

The mobile IAP Fe lidar is an instrument for middle atmospheric temperature, metal atom density, and aerosol measurements. The main operational principle is based on an Alexandrite ring laser system scanning the Doppler broadened Fe resonance line at 386 nm. The precise high-power laser, a narrow field-of-view, and high-resolution optical filters allow high accuracy observations of MLT temperatures, Fe densities, and NLC in full daylight.

The Leibniz-Institute of Atmospheric Physics at the University of Rostock (IAP) in Kühlungsborn, Germany, has developed and operates a transportable Fe resonance lidar (mobile IAP Fe lidar) for MLT research. Measurements with this system provide the primary dataset analysed in this thesis. This section briefly summarises some technical details about the system and the data retrieval.

The first transportable lidar of this kind has been built into an insulated single customised 20' shipping container suitable for polar expeditions (Fig-

Figure 7: The mobile IAP Fe lidar at Davis, Antarctica (69°S) in March 2011. The system is housed in a single insulated 20' container, designed to be transported to remote polar regions. *CC BY-NC 4.0*

ure 7) at the University of Bonn in 1989. Since then it has continuously undergone a series of substantial and incremental improvements [e.g., *Höffner*, 1994; *Schmitz*, 1994; *von Zahn and Höffner*, 1996a]. The system has been operated by IAP since 1994 and measuring on an Fe line since 2004 [*Lautenbach and Höffner*, 2004]. Nearly background-free MLT measurements with high accuracy are possible due to the unique combination of diffraction limited high power laser, active beam stabilisation, narrow telescope field of view, and narrowband detection optics as well as real-time signal processing.

3.1 Laser system

At its core the system uses an Alexandrite ring laser with two flash lamp pumped chambers operating at 33 Hz pulse repetition rate [e.g., *Schmitz*, 1994; *Schmitz et al.*, 1994] (see Figure 8 for a simplified schematic). The unidirectional Q-switched laser achieves a spectral bandwidth of less than 20 MHz with nearly 100% of the pulses in TEM_{00} mode [*Lautenbach and Höffner*, 2004]. The fundamental wavelength of the Alexandrite ring laser is tuned to 771.9820 nm (in air; hereafter: 772 nm) by injection seeding of a tunable distributed feedback (DFB) diode laser.

An external-cavity Lithium triborate (LBO) nonlinear crystal is then used as a frequency doubling unit, generating the second harmonic wavelength. The lidar can thereby probe the $a^5D_4 \rightarrow z^5D_4^0$ transition of the neutral Fe atom at 385.9910 nm (in air; hereafter: 386 nm) [*Lautenbach and Höffner*, 2004]. The mobile IAP Fe lidar can be operated at pulse energies between 100 and 140 mJ. Measurements are commonly performed at around 120 mJ to optimise between signal strength and optical deterioration.

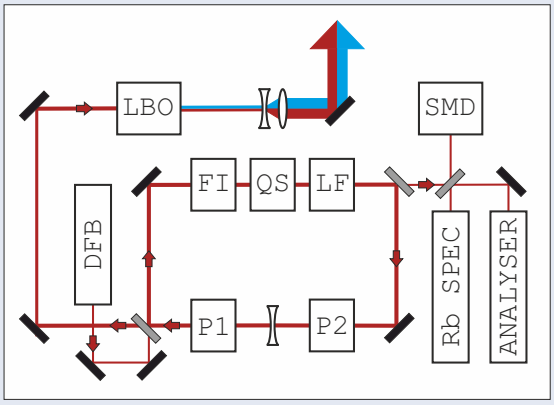

Figure 8: Simplified schematic of the mobile IAP Fe lidar's Alexandrite ring laser system at 772 nm with two pump chambers (P1 & P2), Faraday isolator (FI), Q-switch (QS) with single mode device (SMD), and a Lyot filter (LF) for intra-cavity mode tuning. The ring laser is injection seeded by a distributed feedback (DFB) laser. A spectrum analyser system examines each pulse and compares the frequency to a Rb saturation spectroscopy. An LBO crystal is used for the second harmonic generation to the Fe resonance line at 386 nm. *CC BY 4.0*

The DFB seeder laser is then continuously scanned in a range of ±600 MHz (±1.2 pm at 772 nm) to probe the Doppler broadening of the resonance scattering on the order of the FWHM of the Fe line width (±1 000 MHz, i.e. ±0.5 pm at 386 nm) [*Höffner and Lautenbach*, 2009]. Due to effects inherent to all solid state laser systems (e.g., thermal lensing), the resulting frequency of the ring laser differs from the injection seeded frequency. A patented spectrum analyser system therefore measures the frequency and the mode structure of each laser pulse in real time [*Höffner*, 2015]. Each emitted pulse is compared to a compact Rubidium saturation spectroscopy unit with a resolution better than 100 kHz (≪0.0002 pm at 772 nm) and the signal recorded. The signals of pulses not in TEM_{00} mode are discarded from the measurements.

The pulsed laser is vertically emitted into the atmosphere. A telescope retrieves the scattered light and transfees it to a detection bench. The altitude resolution is given by the time delay of the light detection, with photons from the MLT region arriving approximately 0.5–0.7 ms after their emission.

3.2 Telescope

The system is equipped with a Newtonian telescope composed of a purpose made 80 cm parabolic primary mirror with a focal ratio of $f/2.4$ and a flat secondary mirror with $R{\approx}90\,\%$. The primary mirror is made from Aluminium coated Zerodur with $R{\approx}86\,\%$ at both 386 nm as well as 772 nm and a surface quality better than $\lambda/10$, enabling good preservation of the Gaussian beam. The retrieved light is directly focussed into an optical fibre at the focal point of the telescope and guided to the detection bench (right panel of Figure 9).

An additional camera system operating at $f{\neq}1$ behind the secondary mirror uses ~10% of the signal to determine the walk-off of the laser beam in the field of view (FOV). The offset is fed back to a piezo mounted mirror of the main laser. This setup can stabilise the laser at the pulse repetition rate of 33 Hz and minimise the impact of tropospheric turbulence and other disturbances on the signal [*Eixmann et al.*, 2015].

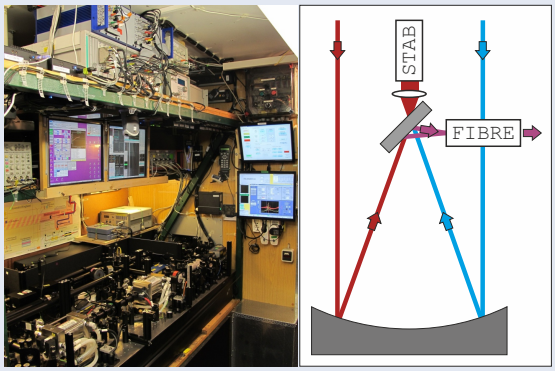

Figure 9: (left) Interior of the mobile IAP Fe lidar container: the Alexandrite ring laser table and electronics system shelf. (right) Schematic of the Newtonian telescope system. Both wavelengths are directly focussed into an optical fibre. A camera system behind the secondary mirror analysis about 10% of the detected light to stabilise the laser in the field-of-view. *CC BY 4.0*

The telescope's narrow FOV of ~60 μrad is an essential component of the system's daylight capability as it reduces the total background radiation received [*Höffner and Lautenbach*, 2009]. It is furthermore optimised to the divergence of the diffraction limited laser. This results in the highest signal-to-noise ratio (SNR) possible with the outgoing laser power. A further reduction of FOV and laser divergence would decrease the signal strength due to seeing which depends on atmospheric turbulence and cause local saturation in the Fe layer [*Alpers*, 1993a]. The telescope system is nearly fully made from carbon fibre materials to eliminate deforming by temperature variations.

3.3 Detection bench

The optically sealed detection bench comprises a spectral beam splitter and two separate detection branches for the UV and IR signals at 386 nm and 772 nm (Figure 10). Both branches use two narrowband plane-parallel Fabry-Perot interferometers (etalons) with high finesse to separate the retrieved signal from direct and diffuse solar as well as other optical background radiation [*Höffner and Lautenbach*, 2009]. The FWHM of the etalons are 10 600 MHz and as 4 200 MHz at 386 nm (~5.3 pm and 2.1 pm), as well as 2 600 MHz and 500 MHz at 772 nm (~5.2 pm and 1 pm). Additionally, interference filters with a bandpass of <0.3 nm are used at the detectors.

The narrow FOV of the telescope results in a small divergence of the collimated signal, allowing to parallelise the beam to a width of less than 18 mm and hence an overall very compact and efficient construction of the detection optics. The near-Gaussian beam quality results in an efficiency of the etalons' transmission and reflectivity of more than 98%. The etalons are equipped with thermally stable Zerodur spacers and are pressure stabilised to the respective central frequencies. The IR channel additionally contains an actively stabilised confocal Fabry-Perot interferometer (CFPI) with a free spectral range of ~1 000 MHz and a finesse 40 designed to detect aerosols with high precision [*Viehl*, 2010].

High-performance photomultiplier tubes (PMT) and avalanche photodiodes (APD) in Geiger-mode detect the UV and IR signals, respectively [*Höffner and Lautenbach*, 2009]. The PMTs and APDs are specifically chosen to exhibit a dark count rate of less than 20 Hz. Hence, at an altitude resolution of 200 m and a pulse repetition rate of 33 Hz the dark count rate accounts for less than 0.1 counts per altitude bin and 4 000 pulses (~2 min). The detectors are read out by a purpose built counter and electronics system designed by IAP operating at 6 MHz. The system creates around 50 MB of data per second overall which is compressed during the hard drive writing process by a specifically devel-

oped and patented packing algorithm to data files of around 4 MB per 2-Minute integration [*Höffner*, 2015]. A mechanical shutter wheel (chopper) with 4 wings rotating at ~8 000 rpm blocks the strong Rayleigh and Mie signals of the lowest 14–20 km to avoid blurring of the sensitive detectors. The current setup of the chopper limits the overall detection altitude to ~208 km. The data algorithm, however, currently only analyses files up to ~145 km.

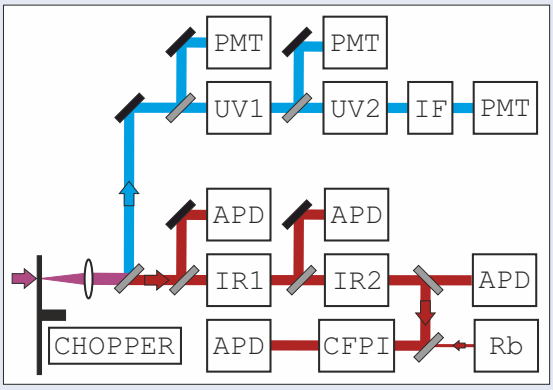

Figure 10: Simplified schematic of the detection bench of the mobile IAP Fe lidar. A chopper wheel blocks the high signal of the lower atmosphere before the parallelised beam is split into a UV and an IR branch. Both branches contain two etalons (UV1/2, IR1/2) as well as several single photon detectors (PMTs, APDs) to analyse each etalon's filter curve. The UV branch has an additional flip mirror interference filter (IF) for daytime operation. The IR branch uses as narrow confocal etalon (CFPI) stabilised to a Rb saturation spectroscopy for high-resolution aerosol detection. *CC BY 4.0*

Contrary to common Rayleigh-Mie-Raman (RMR) lidar systems, the Rayleigh scattering of the neutral atmosphere (predominantly of N_2 and O_2) is currently not used to determine temperatures with the mobile IAP Fe lidar. While this is technically possible and has been successfully demonstrated by *Kaifler* [2014], the spectral properties of the laser and the detection bench are not optimised for this purpose. However, the exponentially decreasing Rayleigh signal in the middle atmosphere is indirectly used as an intensity reference for the resonance backscatter from the Fe layer and the Mie scatter of aerosols in the lower stratosphere.

3.4 Fe density retrieval

The retrieved lidar signal power needs to be compared to the outgoing laser power, as well parameters of atmospheric transmission and atomic backscatter, to determine absolute Fe densities in the MLT region. As *Alpers* [1993a] has shown, the Rayleigh signal in the stratosphere can be used to normalise the outgoing laser intensity. This approach simplifies the wavelength dependent lidar equation, as terms of the transmissivity of the atmosphere and the outgoing laser power can be substituted by a term dependent on the Rayleigh signal, assuming hydrostatic equilibrium. The detected background intensity is simultaneously determined at altitudes well above the Fe layer. With the approach described by *Alpers* [1993a], the Fe density can then be deduced from the lidar equation considering the remaining geometric factor and atomic physical factors including Hanle effect, Zeeman effect, Stark effect, and isotopic effect. Metal lidars may suffer from the so-called "saturation effect" and resonant extinction when stimulated emission of an already excited Fe atom occurs or emitted photons are reabsorbed within the metal layer [e.g., *Simonich and Clemesha*, 1983]. However, while these effects need to be considered for other metals such as K, they are negligible for Fe at the power densities of the mobile IAP Fe lidar [*von der Gathen*, 1990; *Alpers*, 1993a].

The measurement uncertainty depends on several factors, including atmospheric seeing and the intensity of the atmospheric (mainly solar) background radiation. However, it is roughly equal for different densities at different altitudes within the Fe layer. Typical uncertainties of the Fe density retrieval are on the order 2–5% at 1 km resolution and 15 min integration.

The altitude resolution is given by the time of flight measurement. The uncertainty of the altitude resolution mainly depends on the trigger of the counter electronics as well as detector dead time and is a lot smaller than 25 m.

3.5 Temperature retrieval

The mobile IAP Fe lidar determines MLT temperatures by spectrally scanning the Doppler broadened resonance scattering of atoms in the Fe layer. The raw data of 4 000 laser pulses (i.e. ~2 min integration at 33 Hz) is integrated at an altitude resolution between 200–1 000 m. Although the main isotope ^{56}Fe accounts for 91.72 % of the abundance, the isotopes ^{54}Fe, ^{57}Fe, and ^{58}Fe also need to be considered when analysing the combined spec-

tral shape of the resonance scattering [*Lautenbach and Höffner*, 2004]. The filter function of each etalon is determined during each measurement by the mobile IAP Fe lidar at stratospheric altitudes [*Höffner and Lautenbach*, 2009]. With the knowledge of the combined theoretical spectrum of the 4 Fe isotopes, the laser linewidth as well as the filter function, the Doppler broadening can then be deconvoluted, giving a direct measure of the kinetic temperature of the metal atoms [*Höffner and Fricke-Begemann*, 2005]. As local thermodynamic equilibrium (LTE) can be assumed to exist throughout the atmosphere up to the turbopause at around 107 km, this temperature corresponds to the neutral gas temperature at the respective altitude. Potential deviations from the LTE as well as the hyperfine structure and the observed isotope composition as well as higher order effects like the relaxation pathway can be detected and considered by the algorithm through the spectral analysis and comparison with a theoretical model.

The photon statistic of the temperature retrieval depends on several factors, including the outgoing laser power, the atmospheric seeing, and the absolute density of the Fe layer. The uncertainty at the peak of the layer will therefore always be lower than at the layer's edges. Typical uncertainties within the RMS width of the layer are on the order 0.5–1 K for mean daily temperatures and 2–5 K after 1-hour integration [e.g., *Lautenbach and Höffner*, 2004; ***Viehl et al.***, 2015]. A comparative study of Fe and K lidars [*Lautenbach et al.*, 2005] and comparison of K lidars and falling spheres released from sounding rockets [*Höffner and Lübken*, 2007] as well as a comparison with SOFIE temperature observations by the AIM satellite [*Stevens et al.*, 2012] have shown the validity of the temperature soundings. The low uncertainty and high spatial and temporal resolution make the mobile IAP Fe lidar the most accurate temperature sounding instrument for the polar MLT region, in particular during the crucial summer months with 24 h sunlight [***Lübken et al.***, 2015].

3.6 Aerosol retrieval

The mobile IAP Fe lidar can observe aerosols by detecting and analysing the fundamental Alexandrite wavelength at 772 nm and determining the peak of the Mie scattering. Light of this wavelength is always simultaneously emitted, as the extra-cavity frequency conversion to 386 nm is never fully efficient.

Contrary to the UV wavelength, the IR line does not exhibit resonance scattering but only Rayleigh and Mie scattering (in this context the term "Rayleigh scattering" is used for the small particle approximation of the Mie theory while "Mie scattering" refers to the aerosol scattering of particles [e.g., *van de Hulst*, 1981]). As *Viehl* [2010] has shown, the separation of the much narrower and more intense Mie scattering ("Mie peak") from the broader Rayleigh background can be performed by employing a very narrow band CFPI. The CFPI can be stabilised to the same Rb saturation spectroscopy that is used to analyse the frequency of the emitted laser pulse (see Section 3.1).

Using this method, common NLC can be detected within 1 integrated profile (i.e. 2 min of observations). The system can detect very faint NLC at 15 or 30 minute integration time. The probability of missing an average NLC with a mean brightness of $\ll 1 \times 10^{-10} \mathrm{m}^{-1}\mathrm{sr}^{-1}$ and lasting for more than 10 minutes can be approximated to be less than 0.01 %

In addition to the analysis at 772 nm, it is further possible to deconvolve the components of Rayleigh, resonance, and Mie scattering of the retrieved spectra at 386 nm and determine aerosol backscatter from this wavelength at MLT altitudes. As both signals are independently recorded and analysed, they can provide an independent confirmation of each other. The Mie scattering of the NLC at 386 nm is higher than at 772 nm, and less influenced by thin tropospheric clouds. However, the detection with the CFPI at 772 nm has a much larger SNR through the much stronger background suppression. The high SNR makes the detection of (a) smaller particles and especially (b) under unfavourable measurements conditions such as strong solar background or unfavourable atmospheric viewing more accurate and efficient on the IR wavelength. The aerosol (NLC) data presented in this thesis has been obtained with the CFPI at 772 nm.

4 Measurement campaigns

The mobile IAP Fe lidar has been in operation at Davis, Antarctica (69°S) from 2010–2012 and at ALOMAR, Norway (69°N) from 2008–2009 and again since 2014. The measurements have yielded a dataset of more than 4 800 hours of temperature and Fe density observations with unprecedented resolution and accuracy. This unique dataset and the co-located operation of further instruments present a rare opportunity to study the polar MLT region.

The emphasis of this thesis lies on the analysis of a new and unique set of lidar observations and their comparison with other instruments and model studies. This section provides an overview of the two measurement campaigns, conducted respectively in opposing polar regions, during which the lidar data discussed in this thesis has been obtained.

4.1 Davis, Antarctica (69°S)

Davis is an Antarctic research station with year round personnel, very good infrastructure for operating a containerised instrument as well as technical and scientific support allowing continuous measurements. The mobile IAP Fe lidar was transported to Davis (68°34'35"S, 78°58'20"E) in 2010. It was operated there for slightly more than two years in close collaboration with the Australian Antarctic Division (AAD). Additionally, several other instruments for middle atmospheric research are stationed at Davis. The resulting joint datasets of various physical parameters can provide invaluable insights for the understanding of the atmosphere at different altitude levels.

Co-located instruments

Among the instruments operated at Davis are two radars: a VHF mesosphere-stratosphere-troposphere (MST) radar providing PMSE observations at 55 MHz [e.g., *Morris et al.*, 2004; *Alexander et al.*, 2013], and an MF radar providing middle atmosphere wind data at 1.94 MHz [e.g., *Murphy et al.*, 2006; *Morris et al.*, 2006; *Murphy et al.*, 2012]. Furthermore, a Lowe digisonde continuously records sporadic *E* and *F* layers in the ionosphere as well as electron density profiles from about 90 km upwards.

Figure 11: Davis is located on the coast of East Antarctica, 2 381 km north of the Geographic South Pole (SP) and approximately 2 500 km north of the South Magnetic Pole (SMP). *Adapted from Australian Antarctic Data Centre Map No. 13641, CC BY 3.0 Commonwealth of Australia, 2009.*

The AAD has been operating a Rayleigh-Mie-Raman (RMR) lidar at Davis since 2005 [e.g., *Klekociuk et al.*, 2008]. The AAD RMR lidar has been recording temperature and aerosol data from the troposphere up to the upper mesosphere. It has been providing valuable statistics about the occurrence of ice particles in the mesopause region (NLC) and the stratosphere (Junge layer and Polar Stratospheric Clouds) as well as allowing temperature and gravity wave analyses [e.g., *Alexander et al.*, 2011]. As for most RMR lidars, the temperature retrieval does not cover the mesopause region due to the exponential decrease of neutral air density and the resulting loss of signal towards higher altitudes. A combination of RMR and metal resonance lidars therefore enables the investigation of the full temperature structure from the ground to the lower thermosphere. Moreover, MLT temperature observations as provided by the mobile IAP Fe lidar can improve the temperature retrieval of RMR systems by setting an accurate initial temperature for the downward integration [*Gerding et al.*, 2008].

Further instruments installed at Davis are a scanning Czerny-Turner hydroxyl (OH) spectrometer (providing average temperatures in the OH layer around 87 km during dark hours) [e.g., *French and Klekociuk*, 2011] as well as a narrow-field Fabry-Perot spectrometer (providing neutral thermo-

spheric winds from observations of the Doppler shift of auroral emissions) [e.g., *Dhadly et al.*, 2015]. The Space Weather Services section of the Australian Bureau of Meteorology (BOM) monitors the geomagnetic activity with the Southern Hemisphere Imaging Riometer Experiment (SHIRE) and a magnetometer at Davis [e.g., *Morris et al.*, 2005]. The BOM also launches standardised weather balloons with radiosondes twice a day and operates two weather stations at Davis and at Woop Woop, about 35 km from Davis on the Antarctic plateau. A host of further experiments are conducted at Davis but have no direct relation to the middle atmospheric measurements presented here.

Figure 12: Unloading of the 20' shipping container of the mobile IAP Fe lidar from the Australian icebreaker RSV Aurora Australis onto the fast ice at Davis, Antarctica (69°S, 78°E). *Photo courtesy of Dr J. Höffner.*

Mobile IAP Fe lidar campaign

The mobile IAP Fe lidar was shipped to Hobart, Tasmania (43°S) in August 2010 and loaded on board the Australian icebreaker Aurora Australis in October 2010. After a 4 week journey through the Southern Ocean, the system was set up at Davis (69°S) in November and December 2010, commencing first measurements in the MLT region on 14 December 2010 [***Lübken et al.***, 2011]. Measurements continued for more than 2 years until the end of the Antarctic summer season 2012/2013. The very successful first part of the campaign with considerably more measurement hours than expected resulted in stronger than usual deterioration of several laser components. Major maintenance on the main Alexandrite laser became necessary during the 2012 winter. No measurements were therefore obtained between June–September 2012. With this exception, the mobile IAP Fe lidar was in continuous operation whenever tropospheric weather permitted, performing the last measurements on 31 December 2012 [***Lübken et al.***, 2015].

The dataset obtained at Davis includes around 2 900 hours of high resolutive temperature and Fe density measurements in the MLT region. Figure 42 in Appendix C shows the distribution of measurements throughout the year and hours of the day. All months of the year were covered during the campaign, with a minimum of 129 hours obtained in September and a maximum of 381 hours in January, averaging around 241 hours per month. A slight minimum of observations is apparent in the early morning hours, mainly due to tropospheric weather conditions and, to a smaller extent, due to operator fatigue management considerations. However, a substantial amount of measurements has been obtained throughout all hours of the day, enabling representative full diurnal analyses for all months.

Although it had been planned to recover the instrument and the operator after the 2012 SH winter in November 2012, an unusually warm spring, as well as high quantities of dust, deteriorated the fast ice much quicker than usual. Additionally, the Aurora Australis encountered unexpectedly heavy pack ice which delayed progress. By the time of the ship's arrival, the fast ice had deteriorated to such an extent that no heavy cargo could be loaded. Weighing around 9 000 kg, the mobile IAP Fe lidar could not be transported to the icebreaker by alternative helicopter slinging or other means. Hence, the lidar container could only be recovered nearly 4 months later in the middle of summer once the sea ice had cleared, which gave the opportunity for an unplanned third season of measurements. As Section 17 shows, this turned out to be a scientifically very fortuitous coincidence, as the third season in a row showed a markedly different temperature structure in the MLT region compared to the previous two years [***Lübken et al.***, 2015].

In early February, the mobile IAP Fe lidar container was transported to the Aurora Australis via barge transfer and shipped back to Australia and then further to Kühlungsborn, Germany, where it arrived for maintenance at IAP on 12 June 2013.

4.2 ALOMAR, Norway (69°N)

After thorough maintenance and upgrade of several infrastructure components, the mobile IAP Fe lidar container was transferred to the Arctic Lidar Observatory for Middle Atmosphere Research (ALOMAR) in northern Norway in June 2014. ALOMAR is located on top of the Ramnan mountain on the island of Andøya (69°16'42"N, 16°00'31"E), 2 303 km south of the Geographic North Pole and approximately 2 700 km south of the North Magnetic Pole.

Figure 13: The mobile IAP Fe lidar container at the Arctic Lidar Observatory for Middle Atmosphere Research (ALOMAR) on Andøya, Norway (69°N, 16°E). Measurements at similar latitudes in the Arctic and Antarctica allow a unique comparison of the differences and similarities of both hemispheres. *Photo courtesy of R. Wörl.*

Co-located instruments

ALOMAR is mainly operated by personnel of the Andøya Space Centre (ASC) in Andenes, Norway. The observatory houses several instruments for middle atmosphere research. The largest and likely most visible instrument at ALOMAR is the steerable double-beam ALOMAR RMR lidar with two 1.8 m Cassegrain-design primary mirrors and a dual Nd:YAG laser system. The ALOMAR RMR lidar has been employed to study middle atmosphere temperatures, NLC properties, stratospheric winds, and gravity waves [e.g., *Schöch et al.*, 2008; *Baumgarten et al.*, 2012; *Hildebrand et al.*, 2012; *Baumgarten et al.*, 2015]. Further instruments at ALOMAR include an ozone lidar as well as a Na lidar [e.g., *Dunker et al.*, 2015]. ASC personnel allow year-round operation of the instruments. Observations are routinely conducted and supported by staff and students of IAP, in particular at nighttime and during the summer months crucial for NLC observations.

ASC further operates a facility to launch atmospheric sounding rockets. Sounding rocket campaigns studying the dynamics and chemistry of the MLT are frequently conducted [e.g., *Lübken*, 1999; *Rapp et al.*, 2012]. Lidar and rocket-borne measurements have also been combined to validate new measurement techniques and to provide more accurate observations overall [e.g., *Lübken et al.*, 2016]. Further important instruments for middle atmospheric research have been built close to ALOMAR and are operated by IAP personnel. The Middle Atmosphere ALOMAR Radar System (MAARSY) is a very recent and modern VHF radar operating at 53.3 MHz. It is set up as an active phased array antenna comprised of 433 three-element Yagi antennas and provides, amongst other measurements, PMSE data. The narrow-beam Saura MF radar system operating at 3.17 MHz provides wind and turbulence parameters between 50 km and 94 km at an altitude resolution of 1–1.5 km. Similarly to Davis, the combined dataset of various instruments at ALOMAR results in unique opportunities for atmospheric research.

Mobile IAP Fe lidar campaign

Figure 42 in Appendix C shows the measurement statistics of the mobile IAP Fe lidar at ALOMAR, combined for the years 2008–2009 as well as since July 2014. During the first deployment of the lidar in 2008–2009, around 400 hours of observations were obtained at ALOMAR. Since July 2014, an additional 1 500 hours of Fe density and temperature observations have been acquired, adding to a total of around 4 800 hours in both hemispheres. The measurement uncertainties at ALOMAR are equal to those from the observations at Davis, Antarctica.

As for the measurements in Antarctica, the statistics show a small decline in observations during the early morning hours. Similarly to the conditions at Davis, this is mainly caused by tropospheric weather. However, on some occasions, measurements efforts were hampered, as the system cannot be operated entirely autonomously at ALOMAR due to aviation safety considerations and technical challenges. As ASC operators or IAP personnel are not always available, especially during weekends, public holidays and at night, valuable measurement opportunities are so far occasionally missed.

Summary of Results

The following Sections 5 to 18 summarise the main results of this thesis published in peer-reviewed journals. The individual chapters give an overview of the previously existing knowledge, the methods and results of the studies, and the insights gained from the analyses. Where applicable, some open questions or relations to other studies are briefly mentioned. Citations to papers authored by the candidate are given in ***bold***. For further details refer to the manuscripts reprinted on pages 63 to 126.

5 Bottomside extension of the Fe layer during daylight

The mesospheric Fe layer shows a pronounced extension of the bottomside during periods of daylight. Observations of this extension in both hemispheres are quantitatively analysed. A lower limit to the reaction creating Fe at the bottomside is derived. The analysis suggests that only the direct photolysis of FeOH can be fast enough to explain the observations.

A regular downward extension of the mesospheric Fe layer has been observed at ALOMAR, Norway and McMurdo, Antarctica [*Yu et al.*, 2012]. The phenomenon is caused by solar irradiance: whenever the MLT region is sunlit (solar elevation $\gtrsim -5°$), the Fe layer shows a pronounced downward extension of the bottomside (Figure 14). *Yu et al.* [2012] analyse the altitude change $\frac{\Delta z}{\Delta t}$ of a defined bottomside contour at different times of the year and demonstrate that this effect depends on the timing of the solar irradiation. *Self and Plane* [2003] show that iron(I) hydroxide (FeOH) is a significant reservoir for Fe at the respective altitudes below 90 km (see Section 2). It is further known that FeOH can react with H to form Fe [*Plane et al.*, 1999]. Based on these principles, *Yu et al.* [2012] give a qualitative explanation of a possible chemical nature of the bottomside extension, suggesting that the photolytic creation of H in the MLT and reaction with FeOH could cause the observed behaviour.

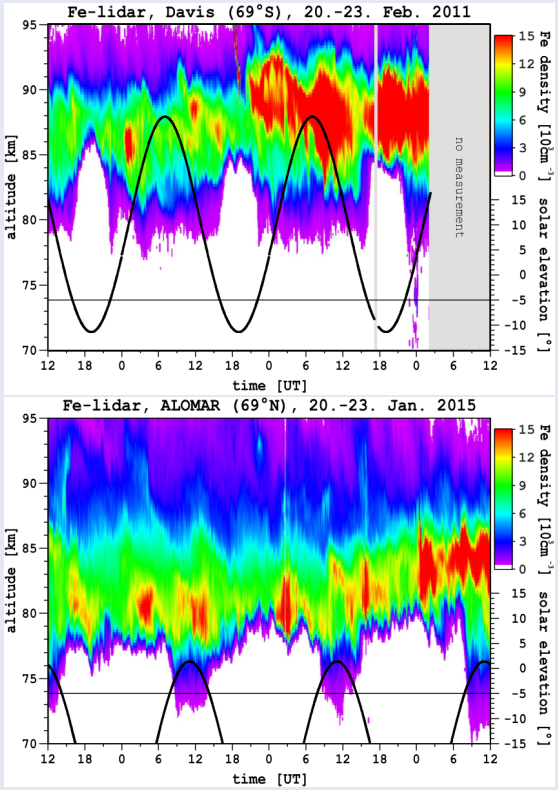

Figure 14: The Fe layer at Davis, 69°S (top) and ALOMAR 69°N (bottom) during 3 cycles of sunrise and sunset. The bottomside of the Fe layer is extended whenever the MLT region is sunlit. *Reprinted with permission from **Viehl et al.*** [2016a, Fig. 1], *Copyright 2016 John Wiley & Sons, Inc.*

A different quantitative approach can be made to analyse the effect in more detail. ***Viehl et al.*** [2016a] investigate the rate of increase $\frac{\Delta[\mathrm{Fe}]}{\Delta t}$ at each altitude rather than the altitude change of the defined bottomside contour, thereby quantifying the rate of increase of Fe at the respective time of apparent sunrise. An example of the analysis is shown in Figure 15. As ***Viehl et al.*** [2016a] show, a first approximation to the reaction creating Fe can then be derived by assuming a full conversion of the reservoir FeOH to Fe. However, Fe is not only created but simultaneously rapidly oxidised via O_3 and O_2 to FeO, FeO_2 and FeO_3, which then react with H_2O and H to $Fe(OH)_2$ and ultimately back to FeOH again. The rate determined from the observations, therefore, sets a lower limit to the rate of the reaction producing Fe.

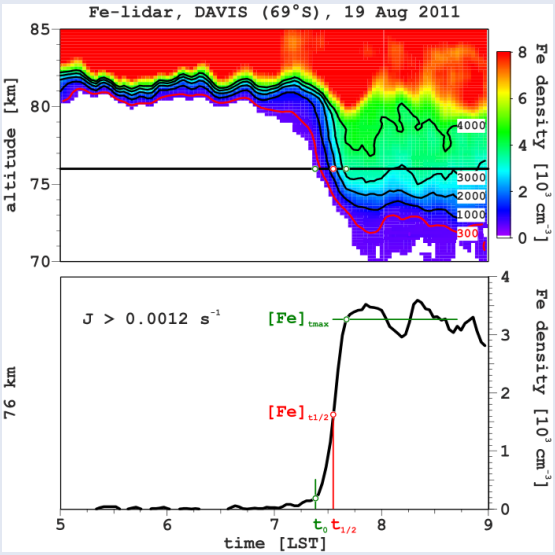

Figure 15: Analysis of the bottomside extension. The observed rate of increase sets a lower limit to the photolysis coefficient. *Reprinted with permission from* [***Viehl et al.***, 2016a, Fig. 2] *Copyright 2016 John Wiley & Sons, Inc.*

Viehl et al. [2016a] analyse all available cases of the bottomside extension observed at Davis (69°S) and ALOMAR (69°N), averaging the rates of increase obtained at all altitudes and days to average out the influence of gravity waves, which could distort the analysis through quick vertical transport and temperature changes. The analysis yields a rate of increase larger than $(1.2 \pm 0.4) \times 10^3\ s^{-1}$ and shows that there is no discernible difference between the hemispheres [***Viehl et al.***, 2016a]. This rate is a lot faster than what was expected of both the reactions of FeOH with H as well as the direct photolysis of FeOH. However, it was so far not possible to measure the photolysis rate J(FeOH) under laboratory conditions. A value much larger than the low level of $J = 1 \times 10^{-5}\ s^{-1}$ hitherto assumed is well possible. On the other hand, a discussion in the literature shows uncertainty regarding the reaction rate coefficients and relative importance of the reactions $FeOH + H \longrightarrow Fe + H_2O$ and $FeOH + H \longrightarrow FeO + H_2$ [*Jensen and Jones*, 1974; *Rumminger et al.*, 1999; *Self and Plane*, 2003]. However, even the fastest assumptions don't seem to be able to reproduce the observations as the modelling work by *Feng et al.* [2013] shows. Hence, after the analysis of the lidar observations, it appears more likely that the direct photolysis of FeOH causes the bottomside extension instead of the reaction of FeOH with photolytically created atomic H.

A further indication of the relative dominance of the direct photolysis of FeOH over the reactions with H is the diurnal cycle of atomic H in the polar summer MLT region. While H is mainly created through photolysis of H_2O at sunrise, its abundance increases until sunset and only slowly decreases thereafter with sufficient H for potential reaction with FeOH remaining for several hours. As the bottomside extension rapidly retracts at sunset, the diurnal cycle of H argues against a dominating contribution of the reactions of FeOH with H. However, the abundance of ozone which is responsible for the oxidation of Fe simultaneously increases at sunset. As all reaction rates depend on the abundances of several non-steady species, only a full chemical model including all reactions and abundances such as presented by *Feng et al.* [2013] can quantitatively examine the relative importances adding to the observed effect.

Section 6 examines the possible pathways from FeOH to Fe closer and gives new insights on their importance for the Fe chemistry in the MLT region.

6 Photolysis of FeOH and reactions with H

The combination of mesospheric lidar observations, quantum chemical calculations, and 3D atmospheric modelling is used to derive a photolysis rate. Two previously not well-known reaction rate coefficients are re-evaluated. Implementation of the new photolysis rate and reaction rate coefficients markedly improves the modelling of the mesospheric Fe layer.

Laboratory studies have provided a broad insight into the gas phase metal chemistry of the MLT region [e.g., *Helmer et al.*, 1998; *Rollason and Plane*, 2000; *Self and Plane*, 2003; *Vondrak et al.*, 2006]. However, not all molecules have a suitable electronic transition for probing with laser-induced fluorescence, which means that some important and relevant reactions with metal-containing species cannot be directly investigated in the laboratory. The recent use of photo-ionisation combined with Time-of-Flight mass spectrometry has enabled some new species to be detected, and their kinetics studied directly [*Goméz-Martín et al.*, 2015]. Nevertheless, the photolysis rate of FeOH cannot currently be examined with either technique. It had been assumed to be negligible and set to a low

level of $J(\mathrm{FeOH}) = 1 \times 10^{-5}\ \mathrm{s}^{-1}$ in atmospheric model calculations [*Feng et al.*, 2013; *Plane et al.*, 2015].

Analyses performed by ***Viehl et al.*** [2016a] show both that the photolysis of FeOH most likely causes the bottomside extension and that the photolysis rate seems to be larger than $(1.2 \pm 0.4) \times 10^{-3}\ \mathrm{s}^{-1}$ (Section 5). Subsequently, ***Viehl et al.*** [2016a] perform quantum chemical calculations to test this assumption and to determine a plausible value of the photolysis rate. The range-separated CAM-B3LYP functional introduced by *Yanai et al.* [2004] is used with the 6-311+g(2d,p) basis set to optimise the geometry of FeOH in the Gaussian 09 suite of programs [*Frisch et al.*, 2009]. The time-dependent density functional method [*Scalmani et al.*, 2006] is then used to compute the necessary energy transitions to calculate the photolysis cross section shown in Figure 16. The thermodynamic threshold for FeOH had been determined to be at around 370 nm [*Schröder*, 2008].

However, ***Viehl et al.*** [2016a] point to two pieces of evidence that the broad band between ~300 nm and 400 nm most likely does not lead to photolysis. First, FeOH has a very similar absorption cross section to iron(I) chloride (FeCl) for which experimental data is available for comparison and which, moreover, is electronically analogous. It has been observed that FeCl does not photolyse between 315 nm and 400 nm, but to produce fluorescence instead [*Delaval et al.*, 1980; *Lei and Dagdigian*, 2000]. Second, the Mulliken electron populations show that the excited states of FeOH remain ionic like the ground state until the 8^{th} and higher states which are covalent in nature and more likely to dissociate. This transition is calculated to occur at 300 nm [***Viehl et al.***, 2016a].

Allowing for a slight red-shift for internal excitation, ***Viehl et al.*** [2016a] then integrate over the absorption cross section and the solar flux from 150 nm to 305 nm, yielding a photolysis rate of $J(\mathrm{FeOH}) = (6 \pm 3) \times 10^{-3}\ \mathrm{s}^{-1}$. This is more than 500 times faster than previously assumed [*Plane et al.*, 2015]. However, it is only about 5 times larger than the lower limit set by the analysis of lidar observations (Section 5) and hence constitutes a reasonable result which can be tested further.

Viehl et al. [2016a] employ a recent 3D global atmospheric chemistry model to test the implications of the newly determined photolysis rate. On the basis of the Whole Atmosphere Community Climate Model (WACCM), *Feng et al.* [2013] have designed WACCM-Fe for the global investigation of the mesospheric Fe layer. The background chemistry scheme is based on that of *Kinnison et al.* [2007] with the addition of more than 120 gas phase reactions [*Plane et al.*, 2015]. The model further considers the meteoric input through a combination of a cosmic dust astronomical model with a chemical ablation model [*Fentzke and Janches*, 2008; *Plane*, 2004; *Vondrak et al.*, 2008]. More information on the model can be found in *Marsh et al.* [2013a, b].

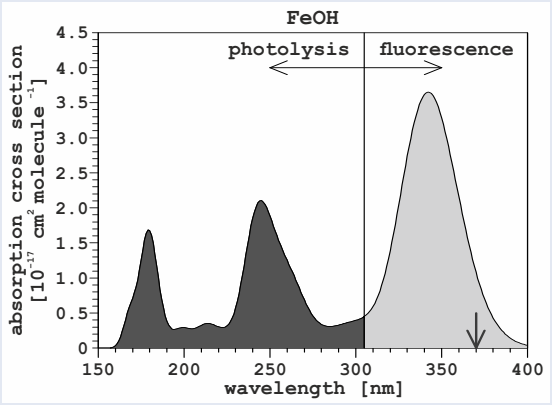

Figure 16: Absorption cross section of FeOH as calculated by hybrid TD/CAM-B3LYP density functional theory. Wavelengths shorter than 305 nm lead to photolysis. *Reprinted with permission from* ***Viehl et al.*** [2016a, Fig. 3] *, Copyright 2016 John Wiley & Sons, Inc.*

Viehl et al. [2016a] use the method of *Merkel et al.* [2009] to increase the vertical resolution of WACCM-Fe in the MLT region from ~3.5 km to ~0.5 km. This is an important step to give a more accurate representation of the crucial distribution of atomic H and O at the bottomside of the Fe layer.

The results of the model simulations are compared to lidar observations (black) in Figure 17. The existing model run by *Feng et al.* [2013] shows a slight increase in Fe density during the day (red). However, absolute daytime densities are underestimated compared to observations and high Fe levels are predicted during the night, when no Fe is observed by lidar. The increased model resolution employed by ***Viehl et al.*** [2016a] results in a more pronounced daytime enhancement and nighttime depletion (orange). Nevertheless, the timing of the observed increase is not captured well. When employing a photolysis rate of $J(\mathrm{FeOH}) = 6 \times 10^{-3}\mathrm{s}^{-1}$ (cyan and blue), the sudden increase of Fe at sunrise is captured very well by the model. The good agreement in the comparison of lidar and mod-

elling work shows that the calculations performed by ***Viehl et al.*** [2016a] were reasonable and seemed to have produced the correct value for the photolysis rate. Hence, the novel combination of quantum chemical calculations and comparison of a global 3D atmospheric model with mesospheric Fe lidar measurements was successfully used to determine the photolysis rate of FeOH.

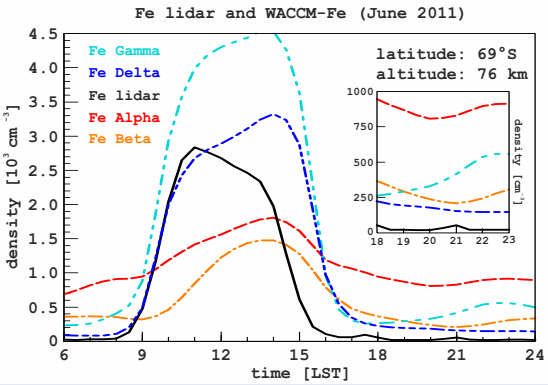

Figure 17: Various WACCM-Fe model runs compared to lidar observations (black). Previous model runs underestimated the increase at sunrise and predicted high Fe densities during nighttime periods (red and orange). With the implementation of a new photolysis rate of FeOH deduced from quantum chemical calculations and lidar observations, the representation of the increase at sunrise as well as the absolute abundance of Fe is markedly improved (cyan and blue). The use of two new rate coefficients for reactions of FeOH with H reproduces the low nighttime densities observed (blue). *Adapted with permission from* ***Viehl et al.*** [2016a, Fig. 4], *Copyright 2016 John Wiley & Sons, Inc.*

However, the model still shows discrepancies to the observed metal layer which can be investigated further. As it turns out, the high nighttime densities of Fe calculated by the model and shown in Figure 17 are nearly exclusively caused by the reactions of FeOH with H (cyan). ***Viehl et al.*** [2016a] review the dispute about these reactions mentioned in Section 5. Reinterpreting the results from flame and modelling work by *Jensen and Jones* [1974] and *Rumminger et al.* [1999] as well as the results summarised by *Self and Plane* [2003], an alternative interpretation of the data is drawn. Instead of adopting a single very high coefficient $k_{12a} = 3.0 \times 10^{-10}$ exp(-1264/T) [*Feng et al.*, 2013] and neglecting k_{12b}, the rate coefficient $k_{12a} = 2.0 \times 10^{-12}$ exp(-600/T) can be taken from *Jensen and Jones* [1974] while the pre-exponential factor and activation energy can be altered slightly from $k_{12b} = 5.0 \times 10^{-11}$ exp(-800/T) to $k_{12b} = 6.0 \times 10^{-11}$ exp(-1200/T) [***Viehl et al.***, 2016a]. The changes to k_{12b} are modest when considering the extrapolation over the wide temperature range from the flame work (> 2000 K) and the reactions at typical MLT temperatures between 135 K and 250 K.

When employing both reactions with the described rate coefficients (blue) instead of only considering the presumed $k_{12a} = 3.0 \times 10^{-10}$ exp(-1264/T) (cyan), ***Viehl et al.*** [2016a] find a considerable improvement of the Fe layer description (see inlay in Figure 17). Some discrepancies persist in the evening hours. These may be caused by an incorrect representation of [H] and [O] in WACCM or by a further overestimation of k_{12a} and k_{12b}. However, to reduce the rate coefficients further would have been incompatible with the flame work by *Jensen and Jones* [1974] and beyond the scope of the paper. More laboratory work regarding these reactions is required.

Indeed, ***Viehl et al.*** [2016a] point out that the high spatial and temporal resolution of a resonance metal lidar puts a stringent test to 3D atmospheric chemistry models. If all reactions rates were known precisely from laboratory measurements, the comparison of lidar observations and model predictions could provide valuable information about the overall validity of the transport processes of the model as well as the distribution of the crucial reactants H and O. These reactants, in turn, are of high importance for the abundances of O_3, CO_2, and other species that are crucial for the energy budget of the middle atmosphere.

The analysis by ***Viehl et al.*** [2016a] shows that J(FeOH) is more than 2 orders of magnitude larger than previously assumed. To the knowledge of the authors, this is the first time a mesospheric metal was used to determine a photolysis rate in a "natural laboratory" by the novel combination of techniques. A re-evaluation of reaction rate coefficients discussed in the literature allows slight changes to the rate coefficient of the reaction FeOH + H $\longrightarrow$ FeO + H_2 and results in a significantly improved representation of the mesospheric Fe layer in a 3D climate chemistry model. The bottomside extension shown in Figure 14 can now be explained by the photolysis of FeOH and not by reaction of FeOH with atomic H. The strong importance of photodissociative processes influences the overall diurnal behaviour of the Fe layer and hence tidal effects as reported by ***Lübken et al.*** [2011].

7 Depletion of FeOH during sunlit periods

Mesospheric FeOH is nearly entirely photolysed whenever sunlight is present. FeOH can therefore not be a major reservoir for Fe in the polar summer MLT region. This may have consequences for the formation and composition of meteoric smoke particles.

As discussed in Sections 2 and 5, FeOH is assumed to be the primary reservoir of Fe below 95 km [*Plane*, 2003; *Self and Plane*, 2003]. Figure 18 compares two high resolution WACCM-Fe model simulations without (run Beta) and with (run Delta) the implementation of the new rate coefficients determined in Section 6. The strongly increased photolysis leads to a nearly complete depletion of FeOH whenever sunlight is present. This changes the equilibrium between Fe and its reservoir species in the summer polar mesopause region [***Viehl et al.***, 2016b].

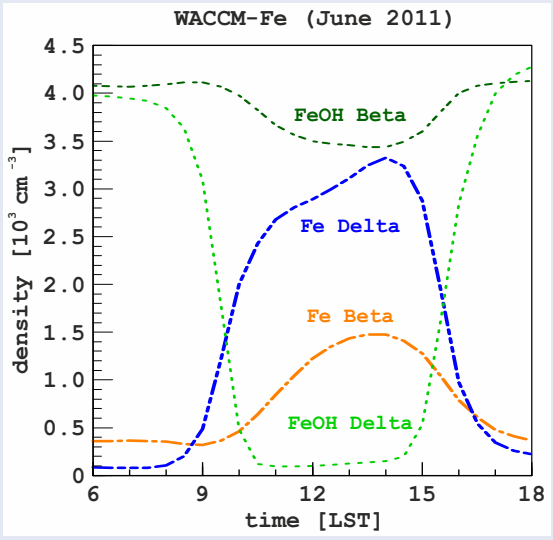

Figure 18: WACCM-Fe calculations of Fe and FeOH. After implementing the new photolysis rate, FeOH is now calculated to be nearly fully photolysed whenever sunlight is present. This may have implications for the formation and composition of MSP. *CC BY 4.0*

The nucleation of meteor smoke particles (MSP) balances the meteoric input creating the metal layers in the MLT region. ***Viehl et al.*** [2016a] note that FeOH can be oxidised by O_3 to form FeOOH. *Rietmeijer* [2001] has shown that the crystalline form goethite (α−FeOOH) is a plausible candidate for MSP. As the polar summer mesosphere is continuously sunlit, FeOH is unlikely to be present in significant concentrations and hence goethite is unlikely to be formed. Fe can still add to silica particles and be oxidised heterogenously and form hematite ($\alpha-Fe_2O_3$), pyroxene (e.g., $FeSi_2O_6$) or fayalite (Fe_2SiO_4) which removes Fe and balances the input [*Self and Plane*, 2003; *Plane et al.*, 2015]. However, *Saunders and Plane* [2006] note that goethite and hematite are the most likely stable solid species. The composition of meteoric smoke particles created in the summer polar regions could differ from regions with considerable periods of darkness. The unavailability of FeOH in the sunlit MLT hence changes the overall composition of expected MSP [***Viehl et al.***, 2016a].

Johnson [2001] proposed that the input of meteoric Fe into the oceans might play an important role for the fertilisation of phytoplankton. A modelling study by *Dhomse et al.* [2013] indicated that this could indeed be the case for the Southern Ocean, resulting in a significant impact on ocean productivity and hence global CO_2 drawdown. A recent idea has been to couple a whole atmosphere model of meteoric metals to an ocean biogeochemistry model to evaluate these processes [*Plane et al.*, 2015]. The changed speciation of MSP which can be expected from the results of ***Viehl et al.*** [2016a] could potentially influence the solubility and availability of Fe in this process.

8 Definition of the metal layer bottomside

The Fe layer's dependence on chemical reactions leads to ambiguous definitions of the layer bottomside. Care needs to be taken when defining and comparing absolute values.

Höffner and Friedman [2004] define the mesospheric metal layer "topside" as the metal and ion layers above 110 km. While analysing the diurnal behaviour of the Fe layer, *Yu et al.* [2012] define the "bottomside" of the layer as the lower 300 cm^{-3} contour and investigate its altitude variation with time. That study concluded that the time lag observed was in accordance with a time delay of the first solar insolation at different altitudes during dawn. Although the conclusion of a seasonal dependence is still valid in this case, ***Viehl et al.*** [2016a] note that care needs to be taken when defining the bottomside in such a way.

The photolysis causing the bottomside extension is a first order reaction. The observed rate of increase will hence depend on the photolysis rate and the abundance of the photolysed species [***Viehl et al.***, 2016a]. Both [FeOH] and subsequently [Fe] show a strong altitude dependence, with higher densities generally at higher altitudes throughout the bottomside extension.

The same absolute amount of [Fe] will therefore generally be reached more quickly at higher altitudes, even if solar irradiance simultaneously sets in at all altitudes. The altitude variation of the bottomside will therfore vary with the definition of different absolute values (compare, e.g., the different contours in the upper panel of Figure 15).

This effect can be significant on time scales comparable to the reaction rates. An alternative approach is to define the bottomside as a set fraction of the maximum density reached at each altitude, e.g., $\frac{1}{10}\,[\mathrm{Fe}]_{\mathrm{max}}\,(z)$ or similar. However, a suitable definition will depend on the application, and a set contour may well be used for time scales a lot larger than the rates of the chemical reactions.

9 Uplift of the Fe layer

The Fe layer at Davis (69°S) shows an uplift during the summer months. This uplift appears to be dynamically induced and not caused by the uptake on ice particles at lower altitudes. Very low densities are observed around summer solstice and coincide with very low mesopause temperatures.

Measurements with the mobile IAP Fe lidar at Davis (69°S) show that the Fe layer in the MLT is at significantly higher altitudes around summer solstice than during the rest of the year [***Viehl et al.***, 2015]. The centroid altitude of the layer (grey line in the upper panel of Figure 19) increases from around 85 km in September to over 90 km in December and then decreases towards 85 km in late March again. Moreover, not only the centroid altitude but the whole layer including the upper and lower edge (centroid altitude ± 0.5 × RMS width) follows this behaviour. The shift is distinctively observable at the 2 000 cm^{-3} and 4 000 cm^{-3} contours between October and February in Figure 19.

These observations question previous explanations of high Fe layer centroid altitudes at polar latitudes and differences between the two Antarctic stations Rothera (68°S) and the South Pole, which were attributed to the uptake of Fe atoms on ice particles at lower altitudes [*Gardner et al.*, 2011]. The measurements at Davis, the South Pole, and Rothera can only be compared to a certain extent, as a harmonic fit has been applied the latter datasets (see *Feng et al.* [2013, Fig. 9] for a direct comparison). However, general features in the observations by *Gardner et al.* [2005, 2011] are comparable to the observations by the IAP Fe lidar at Davis.

The Fe layer's centroid altitude at the South Pole and Rothera was observed to rise while the layer width decreased, similarly to the upper panel in Figure 19. NLC were observed at some distance below the main layer on several days. As several studies had reported an uptake of metal atoms on ice particles, *Gardner et al.* [2011] concluded the metal atoms in the lower part of the Fe layer at Antarctic latitudes had been removed by ice particles and the centroid altitude hence had been shifted upwards. Gaps between the observed large ice particles and the layer were explained by the presumed presence of small, sub-visible ice particles.

However, the altitude increase of the upper boundary of the layer observed at Davis, as well as the early onset of the uplift at low altitudes (in areas with temperatures too high for ice formation), suggest that the summertime upwelling at polar latitudes and the related meridional transport, as well as the temperature dependent metal chemistry, cause the overall uplift [***Viehl et al.***, 2015, 2016b; *Plane et al.*, 2015].

A similar point was made by *Marsh et al.* [2013b] in a modelling study of the global Na layer when comparing their results to lidar observations at the South Pole. Calculations with the global 3D atmospheric chemistry model WACCM-Na showed the uplift of the Na layer at polar latitudes during summer. The authors note that contrary to 1D model explanations of Na lidar observations [*Gardner et al.*, 2005], the PMC uptake was not included in their model and hence not necessary to explain this behaviour. However, *Marsh et al.* [2013b] argue that the average altitude of the Na layer is higher than the Fe layer. The scavenging uptake effect might therefore not be relevant for the Na layer, but possibly for the lower Fe layer. *Feng et al.* [2013] hence include the uptake effect in WACCM-Fe with an ice particle parameterisation as described by *Merkel et al.* [2009].

The summertime increase of the centroid altitude and the simultaneous decrease of RMS width seems to be a global phenomenon at polar latitudes in both hemispheres [*Feng et al.*, 2013, Fig. 15]. However, ***Viehl et al.*** [2016b] show new WACCM-Fe calculations for the months December and January with and without the inclusion of the uptake on ice particles and find no overall effect during the time of the uplift. The observed uplift and the model results provide strong evidence that the influence of ice particles is less relevant to the metal layers than assumed from singular 1D observations [e.g., *Plane et al.*, 2004; *Gardner et al.*, 2005]. It is important to consider the lower contribution of an ice uptake when evaluating the dynamics of 3D atmospheric chemistry models.

Although the uplift of the neutral atomic Fe layer might be qualitatively explained by the dynamical uplift of the residual circulation in the summer polar regions [***Viehl et al.***, 2016b], the net vertical displacement or an average vertical wind cannot be easily deduced from Fe density observations. Fe atoms in the MLT region are no passive tracers but subject to changing temperature dependent chemical equilibria with reservoir species and ionisation processes at different altitudes [*Plane et al.*, 2015]. In fact, the conversion from Fe to Fe^+ through charge transfer with NO^+ and O_2^+ on the topside of the layer should be increased in the sunlit polar summer MLT and suppress an uplift [***Viehl et al.***, 2015]. Moreover, the altitude region between ~90 km to 97 km, in which the increased altitude of the upperside of the layer is observed, has generally much lower temperatures during summer than during winter. As shown by *Plane et al.* [2015], a temperature decrease should move the chemical equilibrium from Fe towards the reservoir species.

These ion-molecule and neutral gas phase chemistry considerations make the observations of the elevated mid-summer Fe layer all the more striking. A quantification of the mean vertical uplift of the neutral atmosphere from Fe layer observations requires detailed 3D atmospheric chemistry modelling to separate transport and temperature-dependent gas phase and ion-molecule chemistry.

Indeed, the largest discrepancies between current WACCM-Fe simulations and lidar observations persist in the upper part of the polar MLT region, where the model predicts an “hourglass shape” of the Fe layer [*Feng et al.*, 2013, Fig. 9]. However, this

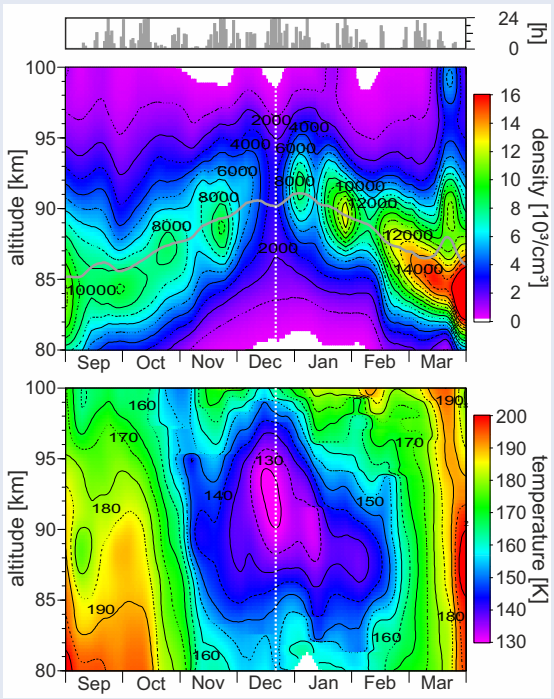

Figure 19: Lidar observations of the mesospheric Fe layer (top) and MLT temperatures (bottom) at Davis, Antarctica during the 2011/2012 summer. The Fe layer is lifted upwards during the summer months. Fe densities are generally lower towards summer solstice. Very low temperatures and an unusually high mesopause altitude coincide with the strongest Fe depletion. *Reprinted with permission from* [***Viehl et al.***, 2015, Fig. 1], *Copyright 2015 Elsevier Ltd.*

depression of the upper edge in the modelling results has not been observed. This may be caused by the known misrepresentation of summer polar MLT temperatures in WACCM changing the chemical reaction rates [*Smith*, 2012], a potentially incomplete understanding of dynamical processes [*Becker*, 2012], or uncertainty about the amount of important reactive trace species such as NO^+ and atomic O [*Pedatella et al.*, 2014]. In fact, due to the increasing knowledge about the metal layer chemistry [*Plane et al.*, 2015], resonance metal lidar observations in the MLT can provide invaluable means to investigate the results of these influences in 3D atmospheric chemistry models. The measurements hence improve the overall understanding of the physics and chemistry of the MLT region.

A further result by ***Viehl et al.*** [2015] shown in Figure 19 is the overlap of extremely low Fe densities of less than 1 000 cm^{-3} and very low summer mesopause temperatures at unusually high altitudes around the summer solstice. This behaviour

had not been observed before and is unknown in the Northern Hemisphere [***Lübken et al.***, 2014]. The coupling of low densities and low temperatures as well as the dynamics of this "elevated summer mesopause" will be analysed in more detail in Sections 11 and 17. The following Section 10 further investigates observations of the occurrence of ice particles and Fe densities.

10 Seasonal influence of ice particles on the Fe layer

Fe column densities at Davis (69°S) show a pronounced seasonal cycle with a minimum around the summer solstice. Simultaneous lidar and radar measurements of ice particles show surprisingly anti-correlated features, in particular in December and January.

Lidar observations by ***Viehl et al.*** [2015] show that the uptake of ice particles does not seem to cause the uplift of the Fe layer (Section 9). However, an overall depleting effect through ice particles might nevertheless be possible. Indeed, several observational studies had reported simultaneous observations of the depletion of metal atoms (Fe, Na, and K) and the occurrence of ice particles measured with radars as polar mesosphere summer echoes (PMSE) or lidars as noctilucent clouds (NLC). However, the duration of the reported Fe depletion by *Plane et al.* [2004] was comparatively short and the vertical extent limited. Model calculations suggesting a depleting effect of PMCs on the Fe layer at the South Pole were only one-dimensional and had to make a series of assumptions *Gardner et al.* [2005]. Reports by *She et al.* [2006] and *Thayer and Pan* [2006] for Na were not made on seasonal scales. The observations of a seasonal depletion reported by *Lübken and Höffner* [2004] were limited to K.

The data set obtained by the mobile Fe lidar at Davis [***Viehl et al.***, 2015] allows a seasonal analysis of the Fe layer and includes an unprecedented amount of measurements during the technically challenging sunlit summer period. Furthermore, the collocated measurements by the Davis MST radar allow the detection of PMSE. The observation of PMSE is a strong indication of the presence of ice particles, including small, sub-visible particles not detectable by optical instruments [*Rapp and Lübken*, 2004].

Figure 20 shows the occurrence of ice particles observed as PMSE (blue) and as NLC (red) as well as Fe column density (black) in the years 2011–2012. A general decrease of Fe column densities is observed from August onwards. During the onset period of ice particle occurrence in mid-November, the decrease pauses, even though a decline due to the uptake on ice particles would have been expected and was observed for K at Spitsbergen (78°N) [*Lübken and Höffner*, 2004]. Moreover, during the period of lowest Fe densities, nearly no NLC were observed at Davis which means the advected ice particles had not lasted long enough to grow to radii >20 nm. The most striking feature of Figure 20 however is the substantial increase in Fe column densities in late December and early January, when NLC were observed to occur 42.5% of the time during 94 h of lidar observation. In contrast, Fe densities were lowest before solstice when no NLC were observed during 130 h of observations during 9 days. Additionally, nearly no PMSE occurred during a local Fe minimum in February.

In summary, Fe column densities are generally lowest during the summer months, when temperatures are lowest, and ice particles can nucleate. However, several striking and unexpected anti-correlated features emerge when the behaviour of the Fe layer column densities before, during, and after the ice particle season are compared in more detail. The timing of onset and disappearence of ice particles does not coincide with drops and increases in Fe column density.

Raizada et al. [2007] have shown that a depletion at any altitude of the metal layer should affect the overall layer and therefore the column density. If ice particles were an important factor determining the behaviour of the Fe layer as suggested in a comparison of two Antarctic stations [*Gardner et al.*, 2011], the occurrence of ice particles would therefore necessarily need to lead to lower Fe column densities. A drop in Fe column densities at the beginning of the ice particle season, as well as a rapid recovery of the Fe layer towards then end, would be expected. However, such features are not observed. Furthermore, the increase of column densities during mid-summer contradicts the predictions of this hypothesis. Neither the meteoric Fe input [*Feng et al.*, 2013] nor the temperature dependence of the Fe chemistry during at low mid-summer temperatures [*Plane et al.*, 2015] can explain a sufficient increase to compensate a potential depleting effect

of ice particles. This anti-correlated behaviour of ice particle occurrence and Fe depletion reported by ***Viehl et al.*** [2015] is the first observational evidence that heterogeneous removal on ice particles is no dominant cause of the seasonal variation of Fe densities at Antarctic latitudes.

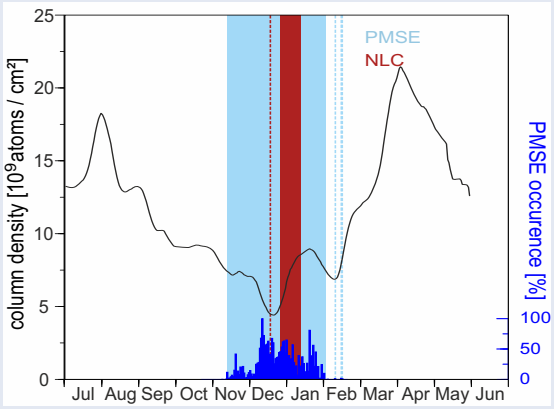

Figure 20: Fe column densities (black) during the 2011–2012 summer season at Davis, Antarctica. Column densities decline during autumn and reach a minimum around the summer solstice. No sharp drop in Fe density is observed at the beginning of the ice particle season (blue). A profound increase in column densities is observed when large ice particles (NLC, red) and PMSE are observed in late December and early January. The anti-correlated occurence of ice particles and low Fe densities on time scales of days questions a dominating effect of metal atom uptake for Fe. *Reprinted with permission from* ***Viehl et al.*** [2015, Fig. 2], *Copyright 2015 Elsevier Ltd.*

A possible explanation for the different behaviour of K and Fe on a seasonal scale might be the dimensionless uptake coefficients of the metal atoms on ice. *Murray and Plane* [2005] have shown that while they are larger than 0.05 and likely to be unity for K and Na, the uptake coefficient rapidly decreases towards 3×10^{-3} for Fe at temperatures below 135 K. These temperatures are common in the Antarctic MLT region around summer solstice and necessary for ice nucleation at this altitude [e.g., ***Viehl et al.***, 2015; ***Lübken et al.***, 2015]. Future studies will have a closer look at the intraday variability of the Fe layer and the interaction with ice particles observed as PMSE and NLC, see Section 22. It may therby be possible to quantify the heterogeneous removal for Fe and explain how an uptake effect might influence the layer locally [*Plane et al.*, 2004] while not being able to proceed to alter the layer on seasonal scales.

11 Temperature dependence of mean Fe density around summer solstice

The temperature dependence of the Fe layer is analysed during a period of substantial Fe depletion around the summer solstice. The high correlation between Fe densities and temperatures during mid-summer seems to be caused by the upwelling and divergence of adiabatically cooled Fe-poor air masses in polar regions.

The chemistry of the metal layers in the MLT region is temperature dependent (see Section 2). Low temperatures shift the equilibrium from Fe towards its oxides and hydroxides, so lower Fe densities are generally expected at lower temperatures [*Plane et al.*, 2015]. Figure 19 on page 27 showed a very strong depletion of Fe around summer solstice which coincided with very low temperatures. Ice particles had previously been held responsible for strong summer time depletions in the MLT region, but ***Viehl et al.*** [2015] show strong evidence against this assumption, see preceding Sections 9 and 10. A general change from high to low densities from winter to summer can be explained by meridional transport *Marsh et al.* [2013b]. However, transport calculations have so far not predicted the substantial depletion observed in Fe in the few weeks around summer solstice. To further investigate the strong depletion, ***Viehl et al.*** [2015] analyse the temperature dependence of the daily mean Fe densities during a ±40 day period around summer solstice in the 2011/12 season.

An Arrhenius-type plot of ln([Fe]) over T^{-1} in Figure 21 shows a nearly linear relation, suggesting the importance of chemical reactions in this process. ***Viehl et al.*** [2015, Sec. 3.3] then assume a temperature dependent partitioning between Fe and the assumed main reservoir FeOH and deduce an equation which can be fitted to the observations. The resulting fit satisfactorily reproduces the observations for approximate values of main atmospheric constituents. ***Viehl et al.*** [2015] then conclude that temperature-dependent chemistry can explain the strong depletion around the summer solstice.

However, in a corrigendum to the publication ***Viehl et al.*** [2016b] show that this conclusion was invalid for two reasons. First, the bottomside analysis by ***Viehl et al.*** [2016a] revealed that the reservoir FeOH

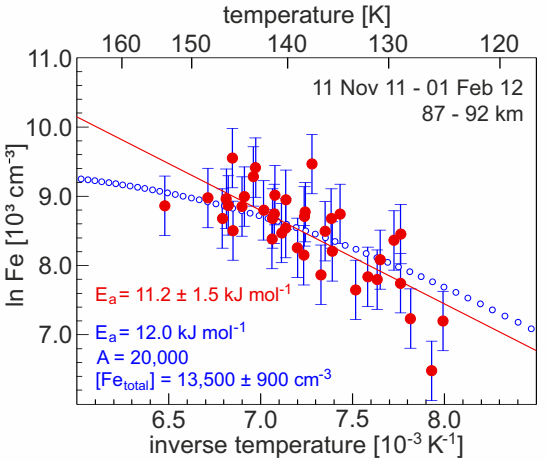

Figure 21: Fe lidar observations of the temperature dependence of daily mean Fe densities (red dots) in a period of ±40 days around the summer solstice. The approximate linearity in an Arrhenius type plot suggests the importance of chemical reactions (red line). An attempt to fit the data assuming a temperature dependent chemical equilibrium between Fe and FeOH seems successful (blue curve), but was only possible due to a mathematical error. *Reprinted with permission from* ***Viehl et al.*** [2015, Fig. 3], *Copyright 2015 Elsevier Ltd.*

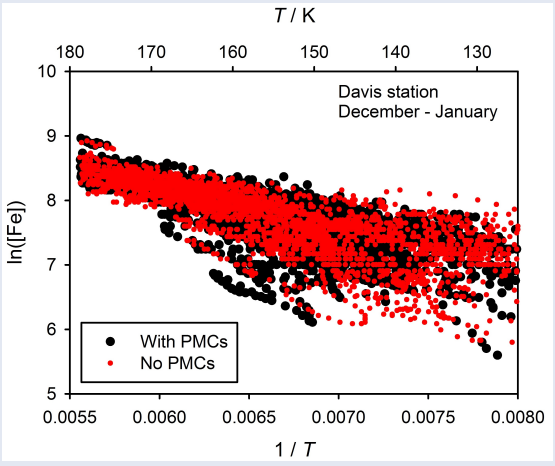

Figure 22: Temperature dependence of atomic Fe calculated by 3D atmospheric chemistry model WACCM-Fe with (black) and without (red) the inclusion of Fe uptake on ice particles. Fe densities are not significantly influenced by the uptake effect. *Reprinted with permission from* ***Viehl et al.*** [2016b, Fig. 1], *Copyright 2016 Elsevier Ltd.*

is nearly fully depleted in the polar summer MLT region. A temperature-dependent partitioning between Fe and FeOH as assumed by ***Viehl et al.*** [2015] therefore seems to be a questionable simplification as the equilibrium will shift to all other reservoir species (FeO_2, FeO_3 and others) as well as atomic Fe. The assumptions and simplifications made are hence no longer good estimates. Second, the fit obtained through the analysis in ***Viehl et al.*** [2015, Sec. 3.3] (blue curve in Figure 21) only matched the observations (red dots) due to an unfortunate mathematical error. ***Viehl et al.*** [2016b] correct this mistake and conclude that gas phase chemistry could no longer explain the depletion observed.

Viehl et al. [2016b] then give an alternative explanation of the observations, supported by calculations with WACCM-Fe shown in Figure 22. The temperature dependence simulated with WACCM-Fe [*Feng et al.*, 2013] is very similar to the observations, albeit at consistently lower absolute densities (black dots). In a comparative run, ***Viehl et al.*** [2016b] show results obtained under the same modelling conditions but without the inclusion of the respective PMC uptake modules (red dots). Both runs show the same temperature dependence of [Fe] around the summer solstice. Most strikingly, the linearity does not change at around 135±5 K, which is the approximate frost point temperature at the respective altitude (see ***Lübken et al.*** [2014] and cyan lines in the left panel of Figure 36 on page 46). However, a change of the temperature dependence would have been expected if ice particles had a substantial effect on the mean densities, as they would only exist and deplete Fe for temperatures lower than the frost point.

In an additional analysis, ***Viehl et al.*** [2016b] compare the temperature dependence of the total amount of all Fe species $[Fe]_{total}$, i.e. the combined abundance of Fe and all of its oxides, hydroxides and ionised species. The temperature dependence is nearly identical to Figure 22. Moreover, the fraction of Fe that is present in the atomic form remains constant at around 60% of $[Fe]_{total}$ over the whole temperature range. This means that the temperature change does on average not cause a shift from one Fe-containing species to another. The change during the two investigated months December and January is hence a simultaneous change of temperature and $[Fe]_{total}$.

As is well known [e.g., *Becker*, 2012], the upwelling at polar latitudes during summer is inherently linked to a strong adiabatic cooling effect. Hence, the only possible explanation for the simultaneous observation of low temperatures and low Fe densities is that both are results of the residual circulation [***Viehl et al.***, 2016b]: when Fe-poor air rises to

the mesopause region, it cools adiabatically and is then transported equatorwards. On the other hand, neither the meteoric input nor the chemical sinks change significantly over the investigated period and can hence not explain this behaviour.

An additional, presumably small uptake effect of Fe atoms and reservoir species on ice particles is not ruled out by this conclusion. However, the occurrence of ice particles at this altitude most likely seems to be a coincidence facilitated through the low temperatures and not a dominant driving factor of the seasonal change [***Viehl et al.***, 2015, 2016b].

12 First measurements of thermal tides in the Antarctic summer mesopause region

Fe lidar measurements at Davis (69°S) reveal the first observations of thermal tides in the polar summer MLT region. Surprisingly, tidal modulations are a lot larger than expected from model calculations. Tides in Fe density have similarities with tides in temperatures and can be observed over a larger altitude range into the lower thermosphere.

Atmospheric tides are present throughout the atmosphere and can play an important role for the thermal and dynamical state of the MLT region. As ***Lübken et al.*** [2011] point out, they can significantly modify gravity wave propagation and change composition due to transport. Atmospheric tides interact with gravity waves and larger scale motions, hence influencing wave breaking and the deposition of momentum [e.g., *McLandress*, 2002; *Mayr et al.*, 2005a, b]. In general, tides may affect the analysis of middle atmospheric trends [*Beig et al.*, 2003]. A precise knowledge of tides is needed to estimate a potential bias of trends in PMC satellite observations which cover only certain local times and change from year to year [*DeLand et al.*, 2007].

Predictions about solar thermal tides in the polar MLT region were rather small with amplitudes around 1–2 K [e.g., *Zhang et al.*, 2010; *Achatz et al.*, 2008]. Measurements were so far mostly limited to radar wind observations [e.g., *Oberheide et al.*, 2006; *Hoffmann et al.*, 2010]. Satellite-borne temperature measurements can provide analyses of thermal tides, even though the slow orbit precession (which requires an integration of several weeks for a full coverage of all local times) may hamper the observations. Nevertheless, satellite analyses have shown strong thermal tides at equatorial and mid-latitudes. During the dark hours of 3 winter months, these observations were shown to be compatible with K lidar soundings [*Shepherd and Fricke-Begemann*, 2004]. Amplitudes are strong around the equator, but weaker (<3 K) towards the polar circle. No measurements were available in the polar MLT [*Forbes and Wu*, 2006].

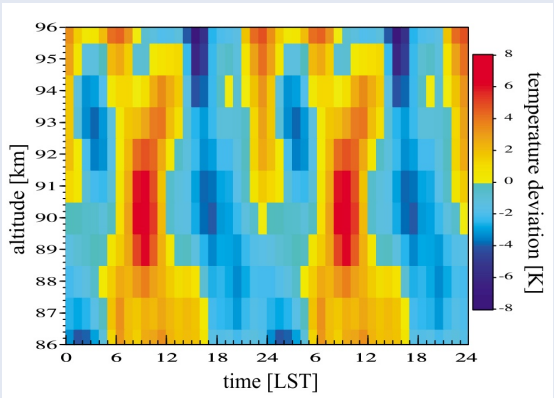

Figure 23: Average MLT temperature deviations from the seasonal mean plotted for a period of two days for better identification of the periodic features. A total of 171 hours of observations obtained during 12 days in January 2011 contribute to this plot. Observed temperature deviations are much stronger than predictions for polar latitudes. *Reprinted with permission from* ***Lübken et al.*** [2011, Fig. 2], *Copyright 2011 John Wiley & Sons, Inc.*

Lübken et al. [2011] report 171 hrs of temperature and Fe density measurements obtained during 12 days of measurement with the mobile Fe lidar at Davis, Antarctica (69°S) between 12–28 January 2011. Figure 23 shows the average temperature deviations in the polar summer MLT region, plotted for a period of 48 days for better visibility of the diurnal and semi-diurnal features. A diurnal variation is observed to dominate below 90 km altitude. Above 90 km, a strong semi-diurnal component becomes apperent. As the data set is large enough and the phase progression in Figure 24 shows consistency with altitude, gravity waves can be ruled out to produce this thermal behaviour due to their random orientation and overall destructive interference. Hence, the features observed by ***Lübken et al.*** [2011] indeed have to be attributed to thermal tides and present the first direct observation in the summer polar mesopause region.

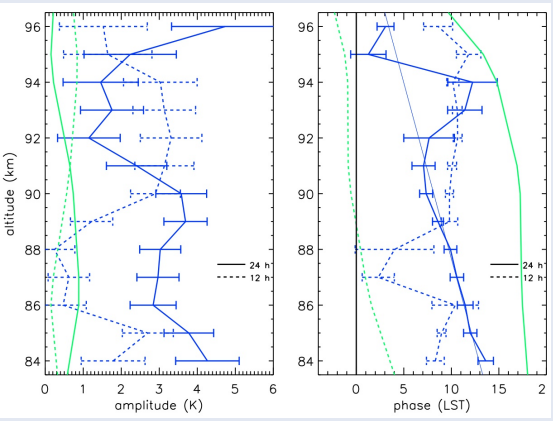

Figure 24: (left) Amplitudes and (right) phases of the diurnal (solid) and semi-diurnal (dotted) tidal components. Fe lidar observations are shown in blue, model predictions are shown in green. Between 84 and 92 km altitude, the phase of the observed diurnal tide can be represented by a vertical wavelength of –30 km. *Reprinted with permission from* ***Lübken et al.*** [2011, Fig. 3], *Copyright 2011 John Wiley & Sons, Inc.*

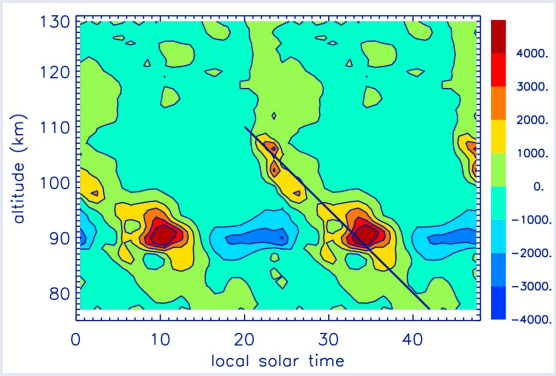

Figure 25: Fe density deviations from the seasonal mean shown for a period of two days. Between 75 km and 110 km altitude, the straight line indicates a phase progression corresponding to a vertical wavelength of –36 km. A diurnal tidal structure dominates this altitude range. Towards higher altitudes, the phase remains constant and shows a stronger semidiurnal component. The Fe layer can be observed over a larger altitude range and with higher accuracy than MLT temperatures. *Reprinted with permission from* ***Lübken et al.*** [2011, Fig. 1], *Copyright 2011 John Wiley & Sons, Inc.*

The analysis of the amplitude and phase structure of the diurnal and semi-diurnal tide in Figure 24 shows a similar phase of both components at most altitudes, leading to constructive interference. The amplitudes of the tidal modulation sum up to more than ± 6 K, which is considerably larger than what models such as the Global Scale Wave Model (GSWM) had so far predicted [*Zhang et al.*, 2010]. The observed diurnal tide is out of phase with GSWM, whereas the semi-diurnal tide matches the predicted phase at higher altitudes. The observations by ***Lübken et al.*** [2011] show that the global modelling of atmospheric tides is incomplete. Either not all tidal sources are yet well known, or the mathematical theory employed in global models is insufficient. The non-linear interactions of non-migrating tides and planetary waves, as well as gravity waves studied by *Mayr et al.* [2005a, b] and others, might play a role in explaining the differences between models and the new observations.

As a further result of ***Lübken et al.*** [2011], Figure 25 shows tidal features in Fe densities. Contrary to temperature measurements, Fe density observations don't require spectral decomposition. Considerably fewer laser pulses per data point are needed to achieve a comparable SNR. Therefore, Fe densities, as well as the tidal signals therein, can be observed in a far larger altitude range (between approximately 75 km and 140 km altitude) than any temperature observation.

The observed tidal modulation of up to ± 40% at the peak of the layer is very large and shows a similar tidal structure to the temperature observations. The vertical wavelength of around -36 km observed in Fe density variations below 110 km is similar to the phase progression of approximately -30 km observed in temperatures, see right panel of Figure 24. As temperatures and densities are derived independently from the lidar signal, this is further evidence for the conclusion that tides cause the observed modulations. ***Lübken et al.*** [2011] suggest that the temperature variation could have a crucial role for the tidal features observed in Fe densities, as the Fe chemistry is highly temperature dependent. However, the authors further note that other factors such as meteoric input, photochemical effects and transport play crucial roles as well.

Since the publication of ***Lübken et al.*** [2011], lidar measurements have covered all months of the year. A full analysis of the data set it currently being performed. Preliminary results in Section 20 show a very constant phase progression in Fe density variations throughout the year. This finding is surprising, as a study about tides in winds at Antarctic latitudes showed strong seasonal variations [*Murphy et al.*, 2006]. The following section attempts to find an approach to examine various influences on metal layer densities quantitively.

13 Tides in metal layers: comparison of lidar observations and a 3D atmospheric chemistry model

Lidar observations of K at 54°N are compared to model simulations. WACCM-K captures the general diurnal and semidiurnal variations of the metal layer satisfactorily. Photochemistry can explain most of the variability. Diurnal temperature variations and tidally driven vertical transport appear to play a minor role for K in the MLT region. A similar analysis for Fe at polar latitudes is possible and likely to show a larger temperature impact.

The lidar observations of strong temperature tides described in Section 12 were accompanied by tides in Fe density. While investigating the Na layer, *Clemesha et al.* [1982] found significant semi-diurnal variations at São José dos Campos, Brazil (23°S) as well as a strong diurnal component below 82 km which was attributed to photochemical effects. Later studies by *Zhou et al.* [2008] and *Yu et al.* [2012] report significant diurnal variations of the Fe layer at Arecibo, Puerto Rico (19°N) and McMurdo, Antarctica (78°S), respectively. Those variations are comparable to the tides reported by ***Lübken et al.*** [2011]. All studies indicate a combination of tidal and photochemical influences. However, direct comparisons of the observed and modelled response of the metal layers to atmospheric tides and the photochemistry in the MLT region had not been undertaken.

In contrast to the other results presented in this thesis focussing on Fe observations at polar latitudes, the analysis of model results by ***Feng et al.*** [2015] presented in this section were obtained by comparing with K (potassium) densities observed at mid-latitudes in Kühlungsborn, Germany (54°N). There were several motivations for this preference. Compared to the analyses of Na and Fe, no diurnal analysis of K had so far been published. As the seasonal variation of K is considerably different to that of Na and Fe [*Plane et al.*, 2014], a fundamental question hence was to investigate the diurnal variation closer and compare it to other metals. Moreover, as ***Lübken et al.*** [2011] have emphasised, the tidal features observed in Antarctica were considerably larger than predicted by GSWM (see Section 12). It therefore seems plausible to first

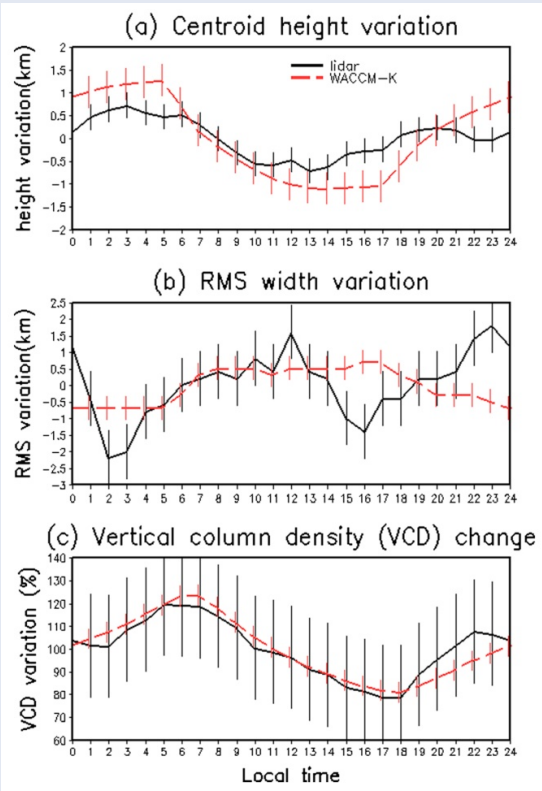

Figure 26: Diurnal variation of (a) centroid altitude, (b) RMS width [km], and (c) vertical column density of the K layer over 24 h. The error bars show the standard deviation of the mean K density. The model (red) reproduces most aspects of the lidar observations (black) reasonably well. *Reprinted from* ***Feng et al.*** [2015, Fig. 2], *CC BY 4.0, 2015 John Wiley & Sons, Inc.*

compare model results and observations at mid-latitudes (where tidal effects should be stronger) and prove the overall agreement, and then compare at more critical polar latitudes later.

Analogously to WACCM-Fe, WACCM-K has recently been developed to describe the neutral and ion-molecule chemistry of K in the MLT [*Plane et al.*, 2014]. Overall, WACCM-K simulates the observed K layer quite well and also captures the large differences between dawn and dusk [***Feng et al.***, 2015]. The production and loss of K at the bottomside is comparable to Fe and follows a similar behaviour as analysed by ***Viehl et al.*** [2016a], with potassium hydrogen carbonate ($KHCO_3$) taking the role of FeOH [*Plane et al.*, 2014]. Figure 26 compares key parameters of the modelled and observed K layer. ***Feng et al.*** [2015] discuss which aspects the model over- or underestimates in comparison to the observations. They conclude that the model satisfactorily captures the lidar observations albeit some

differences persist, which may be attributed to the limited measurement statistic of the observations.

Figure 27 shows altitude profiles of the amplitude and phase (diurnal and semidiurnal) of the measured and modelled K density. Although the maximum diurnal and semidiurnal K amplitudes from the model are at similar altitudes to the ones observed, the model largely overestimates the observed diurnal K amplitude maximum. The model captures the observed phase of the diurnal variation well and correctly predicts a phase of the semidiurnal component later than the diurnal component. ***Feng et al.*** [2015] then investigate the possible effect of atmospheric thermal tides on the diurnal cycle. The variation of the total density of K-bearing species (which is essentially the sum of K, K^+ and $KHCO_3$) varies as a function of altitude and local time and is almost constant at each altitude. These considerations suggest that vertical transport plays a minor role. *Plane et al.* [2014] show how K and K^+ follow a diurnal cycle above ~87 km, converting into each other through photolysis as well as cluster formation and dissociative recombination. Photochemistry also explains the buildup of neutral K atoms below 87 km from photolysis of $KHCO_3$, similarly to the process described by ***Viehl et al.*** [2016a].

The diurnal variation in temperature predicted by WACCM is around 4 K at each altitude between 80 and 100 km, which is comparable to results obtained by RMR and resonance lidar measurements by *Kopp et al.* [2015]. Since the temperature dependencies of the relevant reactions in the K chemistry scheme are comparatively small [*Plane et al.*, 2014], the diurnal variations in temperature do not play a significant role in the diurnal variation of the K layer [***Feng et al.***, 2015]. The analysis further shows that the modelled vertical wind at 54°N is small and corresponds to a tidally driven displacement of less than 1 km, explaining the near-constant total K density at each altitude. Using known reaction rates from *Plane et al.* [2014], ***Feng et al.*** [2015] show that the lifetime of K is short below 80 km (less than 10 min), although doubling effectively during the day because of the increased concentrations of atomic O and H and decresed O_3. The lifetime increases to around 1 day at 100 km altitude and becomes even larger in the thermosphere. These lifetime analyses explain why the in-situ photochemistry plays a much larger role for the diurnal variation of K than other tidal effects. Finally, ***Feng et al.*** [2015, Fig. 3 (c)–(f)] show a comparison of the tidal components in WACCM-K and GSWM. Both models are in good agreement at Kühlungsborn (54°), although WACCM underestimates tidal amplitudes in temperature and vertical wind.

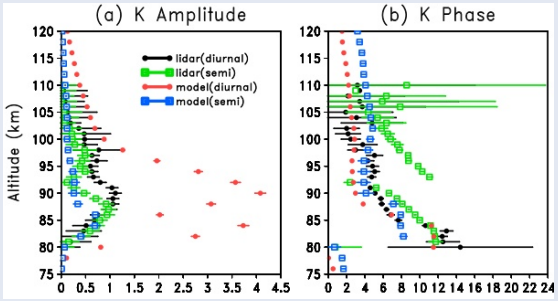

Figure 27: Amplitude and phase of diurnal and semidiurnal tidal phase for potassium lidar observations at Kühlungsborn and WACCM-K model simulations. The model strongly over-estimates the diurnal amplitude. However, absolute column densities, the semidiurnal component, and the phase progression of the metal layer are captured satisfactorily. *Reproduced from* ***Feng et al.*** [2015, Fig. 3], *CC BY 4.0, 2015 John Wiley & Sons, Inc.*

Overall, the analyses by ***Feng et al.*** [2015] show that WACCM can be usefully employed to study the tidal behaviour of mesospheric metal layers. Future studies will examine the validity of this analysis at other latitudes and seasons. A detailed comparison of WACCM-Fe simulations and lidar data might hence provide a deeper insight into the causes of the diurnal variations of Fe observed by ***Lübken et al.*** [2011] and *Yu et al.* [2012] at polar latitudes. A comparison of the temperature tide with the tidal signature in K lidar data was so far not possible due to instrument limitations, but will be in the upcoming analyses of Fe at polar latitudes. The temperature dependence of the Fe chemistry is larger than for K [*Plane et al.*, 2015], hence a different result regarding the relative importances of photochemistry, temperature dependent reactions and tidal transport can be expected. Section 20 shows some preliminary results of the analysis of tides in the Fe layer observed with the mobile Fe lidar at Davis, Antarctica with surprisingly constant tidal features during all months of the year.

14 Gravity wave activity in the middle atmosphere

2 310 h of lidar observations in the stratosphere and MLT region at Davis (69°S) are used to investigate gravity wave activity. The gravity wave potential energy density (GWPED) shows a considerable seasonal variation with a maximum in winter and a minimum in summer. During winter, the GWPED in the stratosphere and the MLT show a similar behaviour. This suggests that the wind field in the stratosphere controls the gravity wave flux to the MLT.

Gravity waves transport energy and momentum over large vertical and horizontal distances and are important for the global meridional circulation from the summer to the winter pole. Gravity wave studies have been performed through observations with radiosondes, radars, satellites, and various lidars [e.g., *Allen and Vincent*, 1995; *Zhang*, 2004; *Alexander and Barnet*, 2007; *Yamashita et al.*, 2009; *Nicolls et al.*, 2010; *Alexander et al.*, 2011]. The mobile IAP Fe lidar allows gravity wave analyses of high-resolution temperature data in the Antarctic MLT region and the stratosphere for a full annual cycle [***Kaifler et al.***, 2015]. These results have already been discussed in full detail in the PhD thesis of *Kaifler* [2014]. The following section presents only a short overview of some important points.

Kaifler et al. [2015] analyse 2 310 h of temperature data obtained by the mobile IAP Fe lidar at Davis, Antarctica between January 2011 and April 2012. The study evaluates the Rayleigh scattering in the stratosphere to derive temperatures between 25 km and 55 km in addition to the MLT temperatures obtained from the resonance scattering of the Fe layer. The stratospheric temperature profiles are sampled with 2 km vertical resolution at typical uncertainties of around 2 K at 40 km and 7 K at 55 km altitude in daytime conditions after 1 h integration. The impact of gravity waves can be characterised through the gravity wave potential energy density (GWPED), which is a measure of the potential energy per unit mass derived from the wave-induced temperature perturbation [*Alexander et al.*, 2011].

An example of this analysis is shown in Figure 28. The left panel shows temperature perturbations from lidar observations with predominantly downward phase progression in the MLT and the stratosphere, which implies an upward transport of energy. The middle panel in Figure 28 shows hourly perturbation amplitudes from around 0.5 K at 30 km altitude up to 15 K in the MLT. The GWPED calculated from these perturbations is shown in the right panel of Figure 28 and increases with altitude. The general increase of the GWPED up to 40 km in the stratosphere and up to 90 km in the MLT region in this example is an indicator for freely propagating waves. The reduced growth rate towards higher altitudes may be associated with wave breaking.

In a further step, ***Kaifler et al.*** [2015] then analyse the seasonal variation of the GWPED. Figure 29 shows the monthly mean GWPED in the stratosphere (blue) and the MLT (red). In the stratosphere, the GWPED shows an apparent maximum during the winter months and a minimum during the summer months, ranging from 0.8 J kg^{-1} to 5.4 J kg^{-1} between 30 km and 40 km. These findings confirm previous results by *Alexander et al.* [2011], who analysed data from the AAD RMR lidar and gave evidence for conservative wave propagation between 35 km and 39 km altitude. The similar results indicate low seasonal variability. In the MLT region, the GWPED is a lot larger than in the stratosphere (ranging from around 40 J kg^{-1} to above 100 J kg^{-1}) due to the exponential growth of the wave amplitudes and the stronger temperature perturbations. However, the GWPED remains below the growth rate of conservatively propagating waves, indicating energy loss rates on the order of 8% km^{-1}.

Large fluctuations in the MLT GWPED are observed during mid-summer, which may result from the temperature variability during summer. ***Kaifler et al.*** [2015] also note that the altitude range of the temperature derivation in the MLT changes throughout the year as the Fe layer is lifted upwards during the summer months [***Viehl et al.***, 2015]. ***Kaifler et al.*** [2015] further point to the apparent correlation between the GWPED in the stratosphere and MLT region, with the same double peak structure observable during winter (Figure 29). This correlation is an indication of the coupling between the atmospheric layers, caused by the selective filtering of waves by winds in the middle atmosphere. This coupling should be important at Davis (69°S), as the Antarctic polar vortex is usually strong and persistent during the winter months.

Figure 30 shows the GWPED in the stratosphere, calculated to 14 day means from spring (October 2011) to autumn (March 2012). Further shown are daily

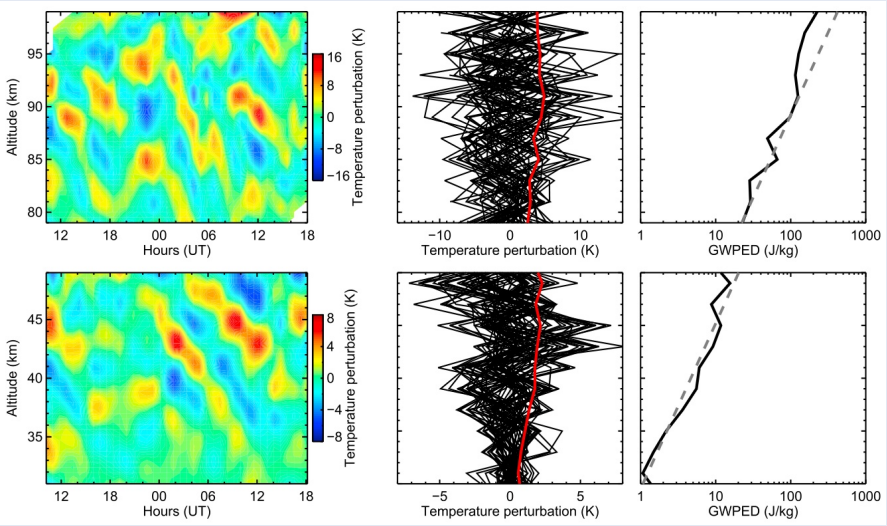

Figure 28: Calculation of the GWPED from temperature perturbations on 15/16 August 2011. (left) Temperature perturbations in the MLT region and the stratosphere. (middle) Hourly perturbation profiles. (right) Mean GWPED (solid) and conservative growth rate (dashed). *Reprinted with permission from* ***Kaifler et al.*** [2015, Fig. 1], *Copyright 2015 John Wiley & Sons, Inc.*

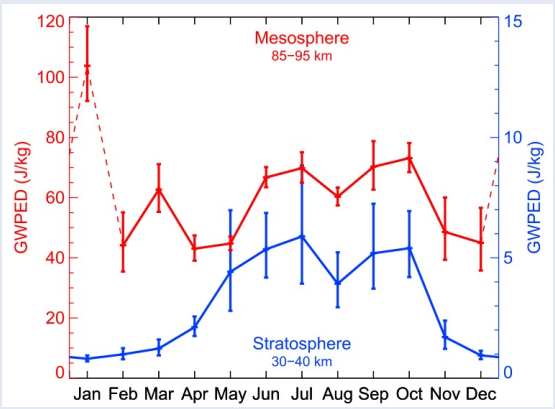

Figure 29: Seasonal variation of GWPED at 69°S. The stratosphere (blue) shows a pronounced double-peak maximum during winter and a minimum around the summer solstice. The MLT region (red) shows a very similar GWPED structure during winter, but a high variability during summer. Vertical bars denote the standard deviation from the mean. *Reprinted with permission from* ***Kaifler et al.*** [2015, Fig. 6], *Copyright 2015 John Wiley & Sons, Inc.*

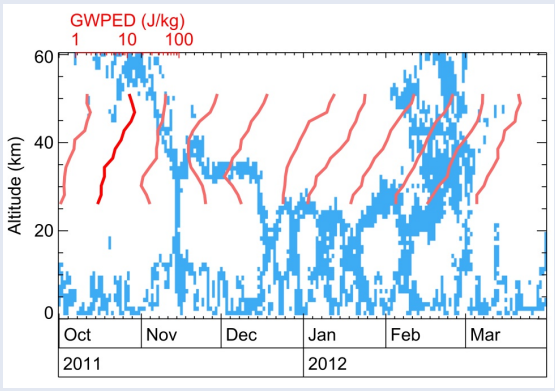

Figure 30: Interaction of gravity waves (GWPED, red) with the stratospheric background wind ($|u| < 2\,\mathrm{m\,s^{-1}}$, blue). The GWPED is reduced below the set wind level in November and December. *Reprinted with permission from* ***Kaifler et al.*** [2015, Fig. 8], *Copyright 2015 John Wiley & Sons, Inc.*

mean zonal winds $|u| < 2\,\mathrm{m\,s^{-1}}$ taken from ECMWF data. The wind reversal associated with the polar vortex breakdown can be seen as the downward progression of the blue shaded area from around 60 km altitude in October to around 20 km altitude in December and January. As a significant result, the GWPED in Figure 30 can be seen to decrease with altitude below the blue shaded area during November and December, which indicates strong wave filtering. From January onwards, the GWPED returns to approximately conservative wave progression conditions.

Using a simple model, ***Kaifler et al.*** [2015] reproduce the observations and conclude that the filtering of gravity waves in the lower stratosphere causes the major seasonal variation of the gravity wave activity at Davis. This is in line with conclusions by *Wilson et al.* [1991], who made similar observations at mid-latitudes. However, the situation during summer is more complicated than during winter. The reversal of the stratospheric winds after the breakdown of the polar vortex results in a selective filtering of gravity waves with small phase speeds. Waves with large phase speeds therefore have to dominate the MLT region, which results in the semi-annual oscillation reported at high and mid-latitudes in the NH [*Hoffmann et al.*, 2010].

15 Ice particles and temperatures after the winter/summer transition in the Antarctic MLT

The winter to summer transition of the MLT region at Davis is analysed using observations of ice particles and temperatures. Mesospheric ice particles (observed as PMSE and NLC) were strongly reduced at Davis (69°S) in the austral summer season 2010/2011. PMSE were further observed at unusually high altitudes. Measurements around summer solstice reveal an unexpectedly high mesopause.

The transition from the winter to the summer state of the MLT region is primarily characterised through a pronounced temperature change. Temperatures in the polar MLT are generally lower during summer than during winter. Most prominently, the altitude of the mesopause shifts from around 100 km during winter to around 88 km during summer [*Lübken and von Zahn*, 1991; *She et al.*, 1993]. These altitude levels are representative for the respective summer and winter hemispheres. The global "two level mesopause" was discovered with an earlier version of the mobile IAP Fe lidar [*von Zahn et al.*, 1996b]. Observations with the mobile IAP Fe lidar at Davis have again challenged our understanding of the MLT temperature structure with the discovery of "mesopause jumps" leading to an elevated summer mesopause [***Lübken et al.***, 2014, 2015]. Section 17 explains the phenomenon in detail and shows why it can only be observed in the Southern Hemisphere. The next two Sections follow the observations leading to the discovery more or less chronologically.

Mesospheric ice particles are an indicator of low summer temperatures in the MLT. Higher summer mesopause temperatures in the Southern Hemisphere (SH) compared to the Northern Hemisphere (NH) have been proposed to explain hemispheric differences in PMSE occurrence through limitations in ice particle formation. In general, mesospheric ice particles in the SH (as observed as PMSE, NLC, or PMC) have lower occurrence rates, occur towards higher altitudes on average, and are more variable than their counterparts in the NH [*DeLand et al.*, 2003; *Bailey et al.*, 2005, 2007; *Latteck et al.*, 2007; *Kirkwood et al.*, 2007, 2008; *Klekociuk et al.*, 2008].

Studies with the Leibniz-Institute Middle Atmosphere Ice (LIMA/ice) model by *Lübken and Berger* [2007, 2011] reproduce these mean characteristics, including the seasonal variation and altitude differences. However, these studies focus on multi-year trends and have so far not explained the details of the winter/summer transition process. The observed and modelled connection of the variation in ice particle occurrence to middle atmospheric dynamics as reported by *Siskind et al.* [2003]; *Kirkwood et al.* [2008]; *Karlsson et al.* [2011], and others had so far not been understood in detail.

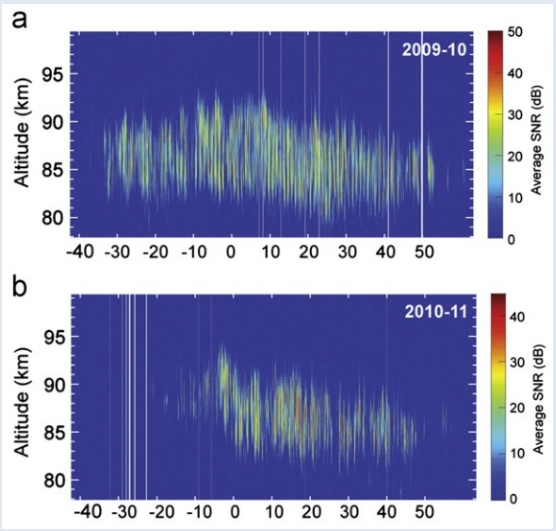

Figure 31: PMSE intensity versus altitude at Davis (69°S) for 2009/2010 (a) and 2010/2011 (b), days relative to solstice. PMSE occurrence was markedly reduced during the austral summer 2010/2011. Significant amounts of PMSE were observed less than 10 days before the summer solstice. The centroid altitude of early PMSE events was significantly higher than on average. *Reproduced with permission from* ***Morris et al.*** [2012, Fig. 1]*, Copyright 2012 Elsevier Ltd.*

Morris et al. [2012] present SH observations of PMSE by the Davis MST radar, and NLC as well as temperatures by the mobile IAP Fe lidar. During the first summer of measurements with the mobile IAP Fe lidar in 2010/2011, the occurrence rate of PMSE was strongly reduced compared to previous years. The first PMSE of the season were observed more than 2 weeks later than in 2009/2010, were unusually faint, and were covering a very limited altitude range (Figure 31). Significant amounts of PMSE were observed a month later than in the preceding year. Overall, the occurrence rate in 2010/2011 was reduced by 59 % compared to 2009/2010. The PMSE centroid altitude throughout the early season was the highest since the MST radar became operational in 2004 (upper panel of Figure 32).

In addition to the PMSE observations, significantly fewer NLC were observed in 2010/2011 compared to previous years [***Morris et al.***, 2012]. The mobile IAP Fe lidar detected NLC only 1.1 % of the time during 322 h of measurement between 18 December 2010 and 8 February 2011. The AAD RMR lidar, on the other hand, had observed NLC at around 19 % of the time during 266 h of measurement at the same location one year earlier between 22 November 2009 and 28 February 2010.

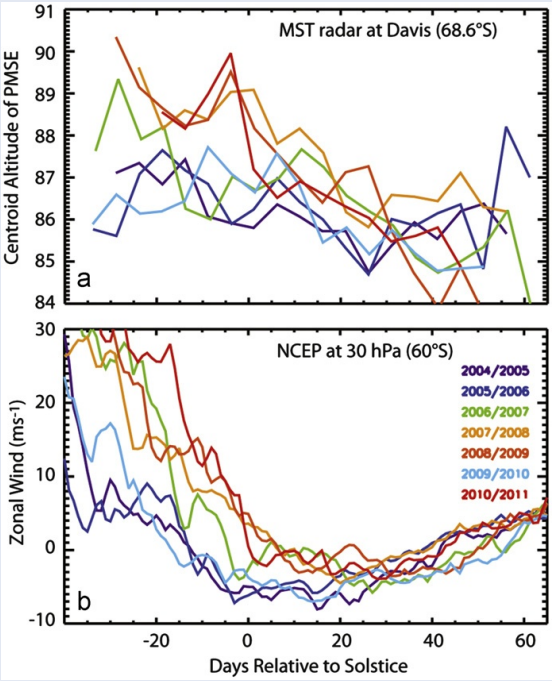

Figure 32: (top) Centroid altitude of PMSE observations during 7 austral summers at Davis, Antarctica (69°S). (bottom) NCEP data of zonal winds in the stratosphere at 30 hPa. The breakdown of the stratospheric polar vortex can be seen in the decrease of the zonal wind. Years with a late polar vortex breakdown are associated with high PMSE early in the season (red and orange). *Reprinted with permission from* ***Morris et al.*** [2012, Fig. 6], *Copyright 2012 Elsevier Ltd.*

This substantial reduction is consistent with strongly reduced PMC observations by the OSIRIS instrument onboard the Odin satellite in the same season [*Gumbel and Karlsson*, 2011]. Observations with the SOFIE instrument on board the AIM satellite later also revealed a significant (more than sevenfold) reduction in PMC occurrence from around 35 % to less than 5 % in the respective years [*Hervig and Stevens*, 2014]. These satellite observations are an independent confirmation of the lidar measurements. These reductions argue for either higher average temperatures at regular PMSE/NLC altitudes, which counteract a long residence time for the ice particles to grow to visibly observable sizes, or for a profound reduction in available water vapour.

First direct temperature observations with the mobile IAP Fe lidar at Davis, Antarctica (69°S) were obtained on 14 December 2010, but only for 1 h. Substantial temperature observations commenced from 18 December 2010 onwards. ***Morris et al.*** [2012] find that the mesopause was unexpectedly high at around 92 km altitude during these first temperature measurements, with average temperatures as low as 116 K (the results are reproduced in the top panel of Figure 34 on page 41). This mesopause altitude is about 4 km higher and the mesopause temperature ~12 K colder than the climatological mean in the NH [*Lübken*, 1999]. In 2007/2008, *Kirkwood et al.* [2008] had also found the SH mesopause to be elevated by 3 km compared to earlier seasons, which coincided with a high PMSE layer.

Mesospheric ice particles usually occur at altitudes around 83 km to 92 km. During common (NH) summer conditions, the mesopause is roughly located at around 88 km, in the centre of the ice particle altitude range. The mesopause altitude at Davis early in the summer season was observed to be elevated to altitudes around 92 km. As the mesopause is the point of lowest temperatures, altitudes below the mesopause are comparatively warmer. At common lapse rates of around $-5\ \mathrm{K\ km^{-1}}$, temperatures at altitudes 4 km below the mesopause will be 20 K warmer than the mesopause. Ice nucleation at regular PMSE altitudes can therefore be reduced by increased temperatures. ***Morris et al.*** [2012] note that this effect alone could explain a large part of the observed anomaly in mesospheric ice particle occurrence.

Furthermore, an altitude increase of 5 km roughly reduces the water vapour available for particle growth by a factor of 10, limiting the growth of all mesospheric ice particles at higher altitudes (see blue lines in the left panel of Figure 36 on page 46). As the optical visibility of NLC ice particles increases with the square of the particle radius, a 5 km increase in altitude, therefore, reduces the optical visibility by two orders of magnitude [***Lübken et al.***, 2014]. The change in average particle sizes resulting from the lower availability of water vapour could explain the observed particular strong reduction of larger ice particles (PMC/NLC) relative to smaller particles observed as PMSE.

16 Stratospheric winds and mesospheric ice particles

Winds in the middle atmosphere control the propagation of gravity waves, thereby influencing the momentum deposition and circulation in the MLT region. The first occurrence of mesospheric ice particles after the winter/summer transition has been associated with the stratospheric polar vortex breakdown (SPVBD). At Davis, the *altitude* of PMSE early in the season strongly correlates with the timing of the SPVBD. However, observations reveal no good correlation of the SPVBD timing with the *first occurrence* of small ice particles.

Ice particles observations have been investigated in both hemispheres to study the variability of the winter to summer transition in the MLT as well as the vertical coupling of the atmospheric layers [e.g., *Woodman et al.*, 1999; *Siskind et al.*, 2003; *Karlsson et al.*, 2007; *Benze et al.*, 2012]. Subsequently, *Gumbel and Karlsson* [2011] note that the very late start of the NLC/PMC season in the SH summer 2010/2011 coincided with a particularly long lasting stratospheric polar vortex. *Karlsson et al.* [2011] investigate the onset of the PMC season in relation to the stratospheric polar vortex breakdown (SPVBD). A good correlation of the timing of the SPVBD and the onset of PMC ice particles as observed by the AIM satellite in the years 2007/2008 to 2009/2010 is found. The correlation is then reproduced with the Canadian Middle Atmosphere Model (CMAM) and explained as being caused by MLT temperature variations through stratospheric wind filtering of gravity waves [*Karlsson et al.*, 2011]. The CMAM simulations show that the mesopause in the SH should be higher, but warmer than in the NH. *Kirkwood et al.* [2008] find this behaviour in analyses of MLS temperature and VHF radar PMSE observations.

Morris et al. [2012] extend the analysis and compare PMSE centroid altitudes during the 2010/2011 summer, as well as the 6 previous summers, with stratospheric zonal wind data from NOAA's "National Center for Environmental Prediction" (NCEP) Reanalysis-1 (Figure 32). Summer seasons which experienced an early SPVBD correspond to years in which the centroid altitude of the PMSE layer was comparatively low, at around 85 km to 87 km throughout the season (blue colours in Figure 32). Summer seasons with a later SPVBD on the other hand show unusually high PMSE centroid altitudes of above 87 km to 90 km early in the season (red colours in Figure 32).

Lübken et al. [2014] present wind analyses of "Modern-Era Retrospective Analysis for Research and Application" (MERRA) data [*Rienecker et al.*, 2011], as well as direct observations of PMSE and temperatures (reproduced in the middle panels of Figures 33 and 34). Contrary to the more qualitative analysis of ***Morris et al.*** [2012], that study uses a more stringent SPVBD criterion at 52 hPa and 69°S, similar to *Karlsson et al.* [2011]. Figure 33 shows several interesting features. First, the SPVBD (red dot) in the first two summer seasons (2010/2011 and 2011/2012) occurred very late in the season around summer solstice, towards the positive standard deviation of the long-term wind observations (black). Second, the zonal-mean zonal wind decreased markedly around 35 days before solstice in 2011/2012 but recovered thereafter (middle panel). ***Lübken et al.*** [2015] call this behaviour a "quasi-late breakdown". Third, in contrast to the first two seasons, the SPVBD occurred unusually early at around 40 days before summer solstice in the summer season 2012/2013 (bottom panel). From 20 days before summer solstice onwards, the winds in 2012/2013 followed typical NH winds (green).

During the 2011/2012 summer season, PMSE with a mean centroid altitude of 86 km first occurred sparsely on 16 November 2011. As Figure 34 shows, the centroid altitude of the PMSE (red line) then follows the temporal development of the mesopause at a distance of around 3 km to 4 km. PMSE in 2010/2011 and 2011/2012 occur at very high centroid altitudes of above 89 km altitude during the SPVBD at around summer solstice. Note that (charged) ice particles cannot be observed as PMSE a lot higher than 94 km because the increasing kinematic viscosity prevents the creation of turbulent structures, eliminating a necessary criterion for radar detection [*Lübken et al.*, 2009].

However, when comparing wind and PMSE data of all three seasons, ***Lübken et al.*** [2015] note that stratospheric winds do not necessarily correlate well with the onset of ice particles after the winter/summer transition of the MLT. In the seasons 2011/2012 and 2012/2013, PMSE were first observed at very similar dates, around 40 days before summer solstice. The final SPVBD, however, occurred almost exactly around summer solstice in 2011/2012 but 40 days earlier in 2012/2013.

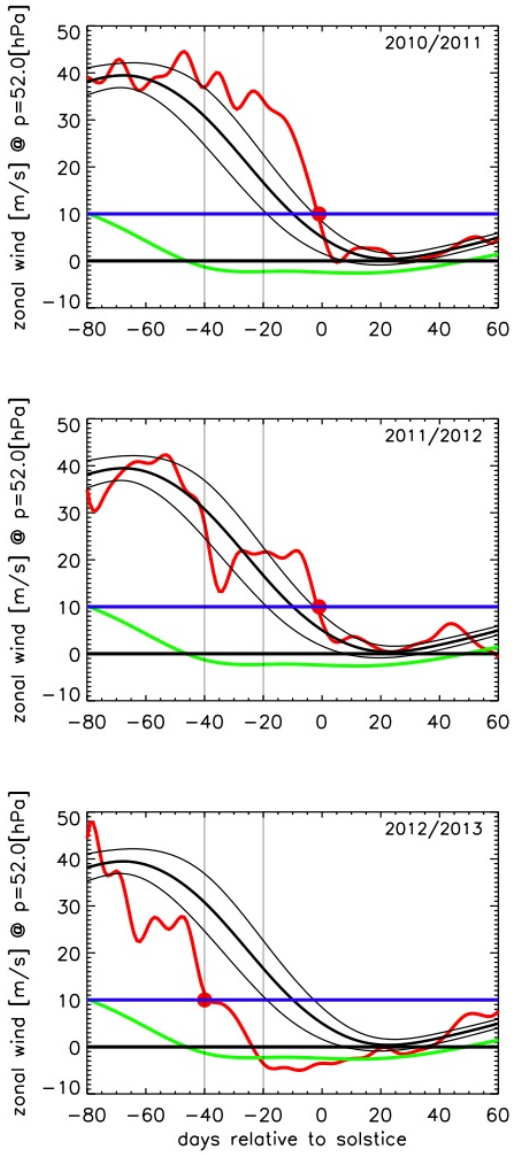

Figure 33: Zonal-mean zonal winds (red) close to 52 hPa at 69°S in the summer months of the years 2010–2013. The stratospheric polar vortex breakdown (SPVBD; red dot) can be characterised to occur when the winds drop below 10 m s^{-1} (blue line). In the years 2010/2011 and 2011/2012, the SPVBD occurred later than the long-term average in the SH (black; mean and standard deviation of anomalies). In contrast, the SPVBD occurred unusually early in 2012/2013. In the NH, average stratospheric winds are less eastward throughout summer (green). *Reprinted with permission from* ***Lübken et al.*** [2015, Fig. 9], *Copyright 2015 John Wiley & Sons, Inc.*

In summary, the observations at Davis, Antarctica find a correlation of PMSE centroid altitudes during the early summer season with the timing of the reversal of stratospheric winds during the winter/summer transition of the SH. It is obvious from Figure 32 that the PMSE centroid altitude is elevated in years with a late SPVBD, i.e. when the zonal wind change from prevailing westerlies to easterlies (from positive to negative values) occurs late in the SH summer season. However, contrary to previous findings by *Karlsson et al.* [2011], the timing of the onset of small ice particles as observed as PMSE by the Davis MST radar does not show a good correlation with the SPVBD. This seems to be strongly related to the different temperature structure of the MLT region in the respective years.

17 Elevated Summer Mesopause

Lidar observations at Davis (69°S) reveal unexpected MLT temperatures during the summer months of some years, while other years resemble conditions in the Northern Hemisphere (NH). Under suitable middle atmospheric wind conditions in the Southern Hemisphere (SH), gravity waves can propagate to unusual altitudes where they deposit their momentum. This high altitude momentum deposition causes an increased summertime polar upwelling, leading to an "Elevated Summer Mesopause" (ESM). An ESM has never been observed in the NH and changes the conditions for ice particle growth in the respective years.

The thermal structure of the summer MLT is significantly influenced by breaking gravity waves and the subsequent residual circulation. The circulation change from the winter to the summer state of the upper polar atmosphere requires gravity waves with eastward phase speeds to break in the MLT. The gravity waves relevant for the momentum deposition predominantly originate in the troposphere and propagate upwards through the middle atmosphere. In the middle atmosphere, gravity waves become unstable or are filtered at critical layers when their phase speed and the background wind speed are equal or differ only slightly [e.g., *Fritts and Alexander*, 2003]. During winter conditions, the persistent stratospheric polar vortex is characterised through strong eastward winds, prohibiting the propagation of gravity waves with eastward phase speeds. Mesospheric winds are weak during winter, setting a further boundary for gravity waves, as wave breaking can result through dynamic instabilities.

Sections 14 to 16 have already discussed the coupling of lower atmospheric layers to the MLT through

gravity wave filtering due to background winds. Differences between the hemispheres originate through different wind patterns and, to a smaller extent, radiative differences. Calculations with the Canadian Middle Atmosphere Model (CMAM) predict the mesopause in the SH to be higher, but simultaneously warmer, than in the NH [*Karlsson et al.*, 2011]. These calculations had been in line with satellite observations of higher average mesopause temperatures in the SH compared to the NH [e.g., *Huaman and Balsley*, 1999].

Observations at Davis

Figure 34 summarises the summer MLT temperature observations by the mobile IAP Fe lidar at Davis in the seasons 2010/2011 to 2012/2013, including the results presented by ***Morris et al.*** [2012] (upper panel), ***Lübken et al.*** [2014] (middle panel), and new results by ***Lübken et al.*** [2015] (lower panel). As previously noted, the mesopause altitude in 2010/2011 was unusually high early in the season and declined thereafter. A similar behaviour was observed in 2011/2012. As expected from similar observations in the NH, temperatures throughout the MLT in 2011/2012 drop by around 20 K at all altitudes during the winter/summer transition about 60 to 40 days before the summer solstice. The mesopause altitude (white line in Figure 34) drops to around 89 km at the beginning of summer. This altitude, as well as the absolute temperatures, are similar to common NH summer conditions. Surprisingly, ***Lübken et al.*** [2014] then observe a very rapid change in mesopause altitude ("mesopause jump"). 20 days after the winter/summer transition of the MLT in 2011/2012, the mesopause altitude increased to nearly 94 km within about 10 days.

Interestingly, the temperatures at these "elevated summer mesopause" (ESM) altitudes were only around 120 K, and hence lower than at common summer mesopause altitudes in both the SH and the NH. Shortly before summer solstice, ***Lübken et al.*** [2014] show lidar temperature observations as low as 100 K (see Figure 36 on page 46).

The surprising behaviour of summer mesopause jumps to an ESM had never been observed in any hemisphere and is in contradiction to previous modelling studies [e.g., *Huaman and Balsley*, 1999; *Lübken and Berger*, 2007; *Karlsson et al.*, 2011]. A likely reason that an ESM in the polar summer MLT had never been observed before is that no observational technique so far had the temporal and spatial resolution of the mobile IAP Fe lidar. This highlights the importance of the technical developments described in Section 3.

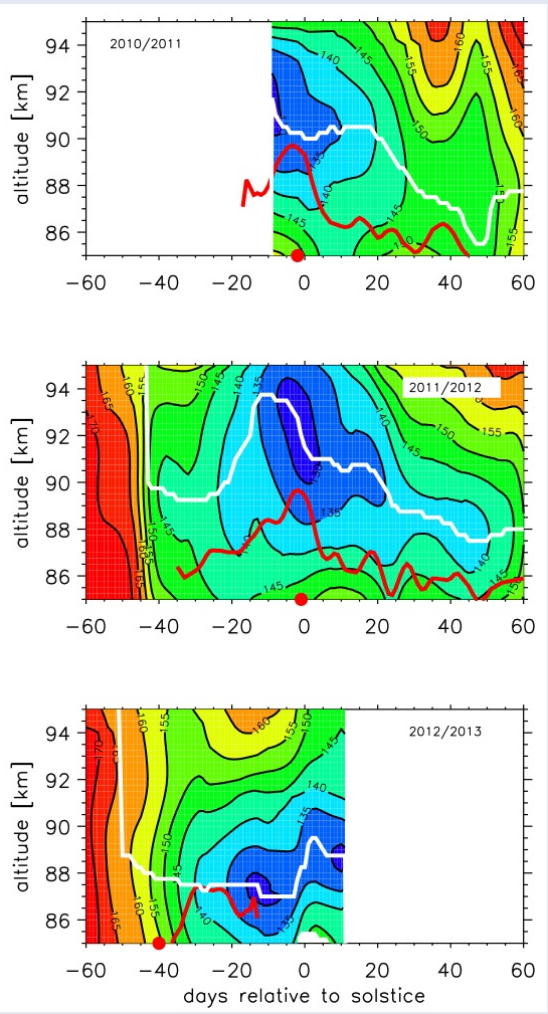

Figure 34: Lidar observations of temperatures (colour scale) in the MLT region at Davis, Antarctica (69°S). The summer mesopause altitude (white line) is elevated shortly before summer solstice when the polar vortex breakdown (red dot) occurs late in the season. The timing of the onset and the mean altitude of PMSE (red line) are also affected by this transition, with PMSE generally following the mesopause altitude. Temperature data are smoothed with Hann filters of 14 days (horizontal) and a 2 km (vertical) width. *Reprinted with permission from* ***Lübken et al.*** [2015, Fig. 3], *Copyright 2015 John Wiley & Sons, Inc.*

After summer solstice, the mesopause altitude steadily decreased in 2010/2011 and 2011/2012, and absolute temperatures were comparable to the NH later in the season [*Lübken*, 1999; ***Lübken et al.***, 2014]. The downward motion of the mesopause can be explained by the effect of interhemispheric cou-

pling in the middle atmospheric circulation [*Körnich and Becker*, 2010; *Becker et al.*, 2015]. Around 60 days after summer solstice, the MLT experiences the autumn transition and temperatures, as well as the mesopause altitude, then rapidly increase to the winter state (not shown).

To explain the observations and the hemispheric differences, ***Lübken et al.*** [2015] investigate zonal MF radar winds obtained at Davis (Figure 35) and compare them to stratospheric winds, as well the correlation with MLT lidar temperatures (Figures 33 and 34). Interestingly, MF radar winds during the ESM period are observed to be much more westward than during non-ESM conditions. Furthermore, westward winds extend to higher altitudes during ESM periods.

Lübken et al. [2015] then use the Kühlungsborn Mechanistic Climate Model (KMCM) by *Becker et al.* [2015] to reproduce the wind fields and temperatures in the MLT. Comparing both hemispheres, as well as control runs without gravity wave interactions, ***Lübken et al.*** [2015] reproduce several features of the MLT temperature structure. The analysis suggests that mesospheric winds above the stratospheric polar vortex change the gravity wave propagation in the years with and without ESM.

Explanation of the ESM

Lübken et al. [2016] have recently presented further correlation analyses of wind fields in the middle atmosphere and MLT temperature changes. In comparing the wave forcing in the SH with the NH, that study provides a comprehensive explanation of the mesopause jumps and the ESM at Davis:

The polar vortex with strong eastward winds is much more persistent in the SH than in the NH and acts as a barrier for gravity waves with eastward phase speeds. The momentum of these waves does not reach the MLT. Occasionally, the SPVBD in the SH occurs as late as 1 or 2 days before summer solstice. Shortly before the SPVBD, gravity waves with large eastward phase speeds can propagate through the stratosphere in the early summer season. Simultaneously, winds in the summer mesosphere are strongly westward. The reduced vertical flux of eastward momentum (compared to mean summer conditions in the NH or later in the SH) results in even stronger westward winds in the upper mesosphere. The strong westward mesospheric winds are a consequence of the reduced gravity wave flux through strong stratospheric winds and the downward control principle [*Haynes et al.*, 1991; *Becker*, 2012; *Becker et al.*, 2015]. Gravity waves with high eastward phase speeds can then pass the mesopause region without breaking because the different signs of phase speed and background wind speed lead to large vertical wavelengths and comparatively stable conditions. The wave amplitude increases further with increasing altitude, breaking only at unusually high altitudes in the lower thermosphere at around 95 km. The relative effect of the momentum deposition is stronger at higher altitudes, inducing even stronger eastward winds, a stronger meridional flow through the Coriolis force, and a subsequently even stronger upwelling to higher altitudes. This causes the very low temperatures of the ESM.

As *Lübken et al.* [2016] note, two important aspects of this explanation are (a) slightly eastward winds which filter gravity waves with low phase speeds, but let waves with high speeds pass to the mesosphere, and (b) strongly westward winds in the mesosphere, enabling the wave propagation to the lower thermosphere. An ESM can therefore only be found if the timing of stratospheric and mesospheric winds is favourable. This condition is never fulfilled in the NH, where the SPVBD occurs early in the season, when mesospheric winds are still in their weak, predominantly eastward winter state. The different stratospheric wind patterns of the hemispheres are therefore responsible for the hemispheric differences observed in the summer polar MLT, including different mesopause altitudes and presumably all observed differences in ice particle occurrence described in Section 15. The importance of gravity waves with large phase speeds for the dynamics of the MLT is in line with the conclusions of ***Kaifler et al.*** [2015] about the selective filtering in the stratosphere (see Section 14).

ESM influence on ice particles

The temperature structure of the summer MLT is highly important for the formation of ice particles. The temporal evolution of temperature around the mesopause is consistent with the findings of Section 15 which showed a strong correlation of PMSE centroid altitudes with stratospheric winds. Below the ESM, the sublimation of ice particles is increased, and ice particles occur in the colder regions at higher altitudes. The increased PMSE

centroid altitudes (Section 15) is, therefore, a manifestation and indication of an ESM in certain years.

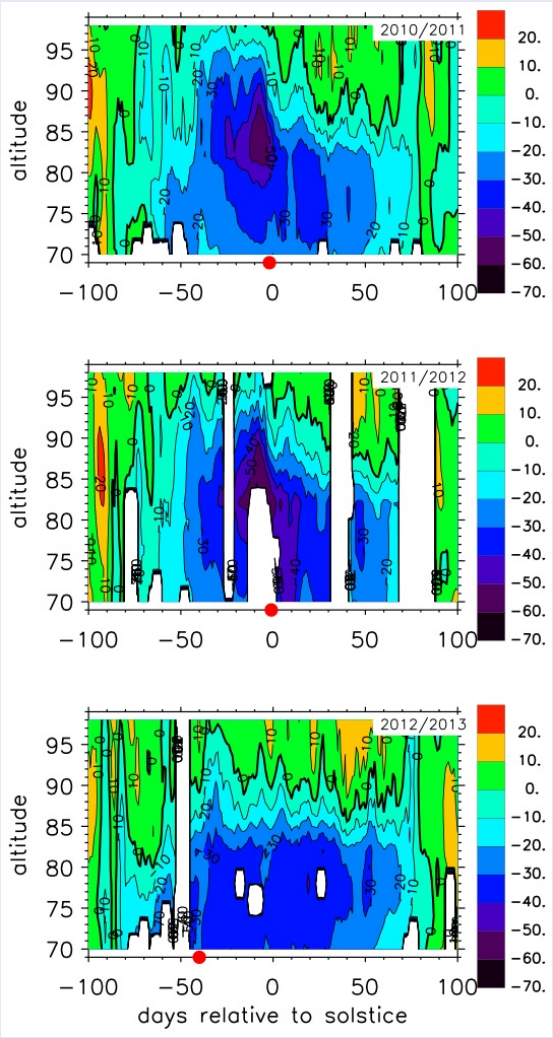

Figure 35: Zonal wind observations in the MLT by the MF radar at Davis, Antarctica (69°S) in the years 2010/2011 to 2012/2013. The red dot marks the stratospheric polar vortex breakdown (SPVBD) around 2, 1, and 40 days before the summer solstice, respectively (see Figure 33). The wind conditions throughout the middle atmosphere influence the gravity wave propagation to the MLT and the subsequent wave breaking and momentum deposition. In years with a late SPVBD, strong negative (westward) winds up to high altitudes can be present in the Southern Hemisphere, leading to a strong summer polar upwelling and very low temperatures. *Reprinted with permission from* ***Lübken et al.*** [2015, Fig. 6]*, Copyright 2015 John Wiley & Sons, Inc.*

As the mesopause altitude decreases to common NH values later in the 2010/2011 season, the temperature lapse rate below the ESM can no longer explain the reduction in ice particle occurrence.

However, ***Morris et al.*** [2012] note that the wind pattern observed by the Davis MF radar suggests a warming by a 2-day wave [*Morris et al.*, 2009]. This, together with strong thermal tides reported by ***Lübken et al.*** [2011] (see Section 12) could increase average temperatures and reduce ice particle growth. It may also be speculated that a change in wind and vertical transport later in the season reduced the available water vapour compared to other seasons. More understanding of these processes is required and might in the future be achieved by comprehensive 3D modelling.

18 Definition of the summer season in the polar MLT

In the Southern Hemisphere, the MLT region temperature transition between winter and summer is coupled to the timing of the polar vortex breakdown. The resulting variability has consequences for some MLT investigations such as the interpretation of trends in ice particle occurrence.

The implications of the traditionally defined seasons based on astronomical parameters (i.e., spring and fall equinox as well as summer and winter solstice) for atmospheric research are seldom considered. When investigating the annual cycle of atmospheric parameters, common analyses include mean winter temperature, seasonal average centroid altitude of a metal layer, or days with ice particle occurrence during the summer season.

However, ***Lübken et al.*** [2015] point out that the astronomical definition of the “Summer Season” may be misleading in certain situations of atmospheric research. As detailed in the preceding Sections, the MLT temperature transition and the occurrence of ice particles depend on the timing of the SPVBD.

This is of particular importance when statistically comparing the occurrence of ice particles of several years [e.g., *DeLand et al.*, 2003, 2007]. If an average is given respective to “all days of summer”, the comparison of various years might lead to incorrect interpretations. For such applications, the beginning of the summer state of the polar MLT in the SH might, therefore, be most accurately defined by the timing of the temperature transition, not by a fixed date in the astronomical calendar.

Further Results and Outlook

The measurement campaigns of the mobile IAP Fe lidar have produced an unprecedented dataset with several unexpected new observations. Not all results have yet been published or fully analysed. The following sections give an overview of some preliminary analyses of important observations.

19 MLT temperature climatology for the austral polar region

Lidar oservations at Davis, Antarctica (69°S) have yielded around 2 900 h of high accuracy temperature measurements in the MLT region. The measurements cover all months of the year and all hours of the day. The resulting dataset is the most comprehensive high-resolution temperature climatology of the austral polar MLT region.

Accurate temperature datasets are essential for understanding Earth's atmosphere. Global reference atmospheres and models provide a broad overview of important aspects [e.g., CIRA-86 and NRLMSISE-00, *Fleming et al.*, 1990; *Picone et al.*, 2002]. However, these references and predictions do not show short term variations, need observational input, and have to be tested for their accuracy.

Existing datasets

Temperature observations in the polar MLT of the Southern Hemisphere (SH) have been obtained by several means, including measurements by satellites, sounding rockets, OH imagers, meteor radars, and resonance lidars. All observations have their respective strenghts and were used for several important studies. However, all observational methods also have their own shortcomings.

Satellite observations such as Aura(EOS)/MLS, TIMED/SABER, and AIM/SOFIE provide a near-global image of MLT temperatures. However, they are particularly limited in their vertical and temporal resolution. For example, the vertical resolution of MLS temperatures in the MLT region is around 14 km [*Schwartz et al.*, 2008]. The error of the SABER temperature retrieval can increase from around 1.5–5 K under favourable conditions to 18 K during the polar summer months [*García-Comas et al.*, 2008]. MLT temperature measurements by the SOFIE experiment are expected to have a precision of ~0.2 K and are obtained during 15 sunsets and sunrises per day [*Gordley et al.*, 2009]. However, the AIM satellite is in a retrograde circular polar orbit and the measurements only take place near the time of local sunrise and sunset [*Russell et al.*, 2009]. Temperature variations by thermal tides in particular can therefore bias the mean, and a warm bias of 10 K has been observed in comparison to other measurements [*Hervig and Gordley*, 2010].

Observations of dynamic features from space are furthermore hampered by the precession of the satellites. In the case of the higher resolution SABER measurements, the precession of the TIMED satellite means that a full 24 h coverage at given point requires and integration of 60 days of observations. Although tidal analysis are still possible with the datasets [e.g., *Zhang et al.*, 2010], none of these techniques allow to resolve waves on shorter time scales or the highly dynamical features in the MLT region as presented in this thesis.

A resonance lidar climatology at the South Pole has been obtained by [*Pan and Gardner*, 2003], covering 26 h of measurements during the crucial summer months November to February (see right panel of Figure 36). With such little data, a potentially strong bias by gravity wave or tidal activity seems likely. Furthermore, ***Lübken et al.*** [2015] point out that those measurements during the summer months did not actually capture the mesopause directly, but interpolated the data above and considerably below the suspected mesopause altitude. Additionally, no observations were made during November at all, leaving quite an important gap of data during the crucial transition time from the winter to the summer state of the Southern Hemisphere. The SH summer months, however, are particularly crucial for many analyses in regards to PMC occurrence or the residual circulation [e.g., *Lübken et al.*, 2016].

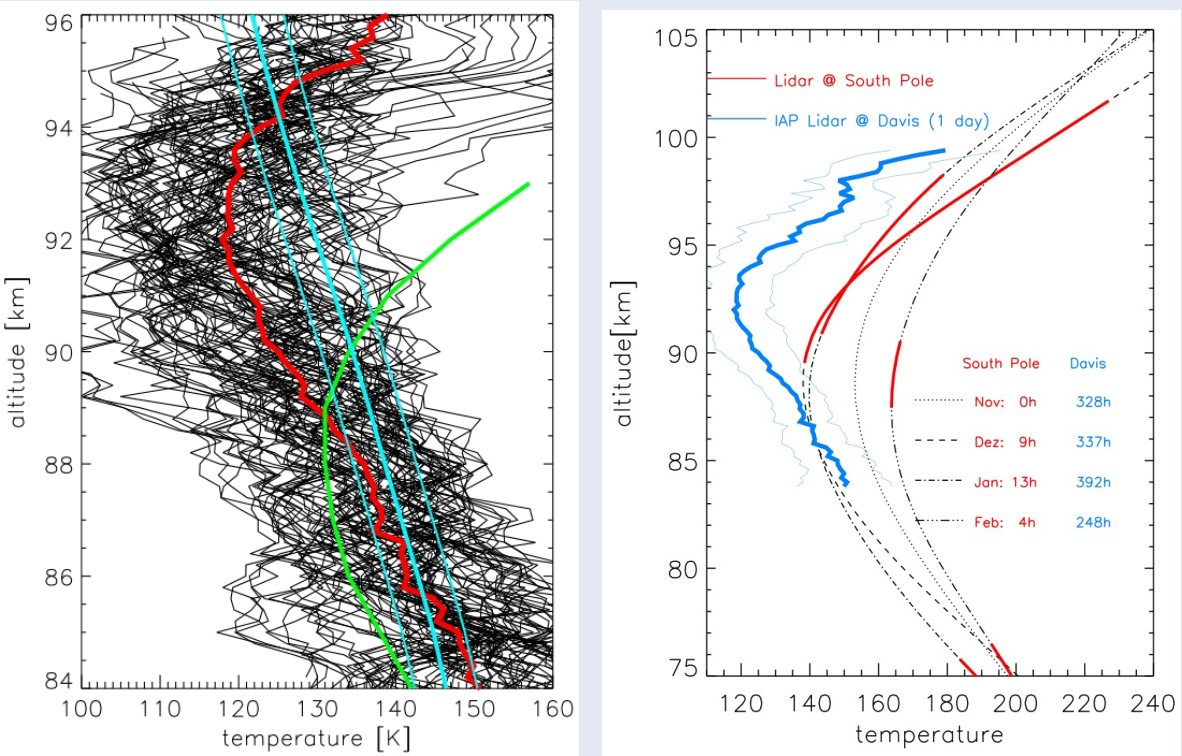

Figure 36: Example measurements of the improved temperature climatology data set obtained by the mobile IAP Fe lidar. (left) 24 h measurement at Davis, Antarctica on 17/18 December 2011: 96 profiles integrated for 1 h every 15 minutes (black), daily mean profile (red) and comparison to climatology of the Northern Hermisphere (green). The mesopause is observed to be high and cold with mean temperatures below the frost point (cyan). Waves cause a high variability throughout the day. (right) Comparison of one day of measurements with the mobile IAP Fe lidar (mean and variance, blue) and previously existing dataset from the South Pole (red). The new dataset contains considerably more hours of measurement throughout the summer months, providing a far more accurate representation of the MLT temperature structure and variability. *Reprinted with permission from* ***Lübken et al.*** [2014, 2015] *Copyright 2014 and 2015 John Wiley & Sons, Inc.*

New dataset

The new climatology obtained by the mobile IAP Fe lidar at Davis, Antarctica (69°S) covers around 2 893 hours of Fe density and temperature measurements. While observations of at least 129 h were obtained during all months of the year, the dynamic summer months November to February were covered particularly well with at least 248 h and up to 392 h (see Figure 42 on page 60). The new temperature climatology contains 50 times more hours of measurement than the existing lidar climatology by *Pan and Gardner* [2003] during the crucial summer months. To date, this is the most comprehensive high-resolution temperature dataset of the MLT region in the SH. The observation of the high altitude of the summer mesopause during some years was unexpected and lead to new insights about the atmospheric coupling (see Section 17 as well as ***Lübken et al.*** [2014, 2015]).

Figure 36 illustrates some features of this dataset. The new observations have revealed some of the lowest temperature measurements ever obtained in the atmosphere as well as a high temperature variability throughout the day. The left panel in Figure 36 shows all lidar measurements (black) obtained during 24 h, the daily mean temperature profile (red), and a comparison to the NH climatology by *Lübken* [1999]. The right panel in Figure 36 compares the data of this one day (blue) to the existing austral lidar climatology (red and black) by *Pan and Gardner* [2003]. The thin blue lines around the daily mean indicate the high variability throughout one day. This shows that temperature variations can be substantial and need to be taken into account.

Parts of the temperature data covering the summer months have already been published in [***Lübken et al.***, 2015]. The full climatology is currently being prepared for publication.

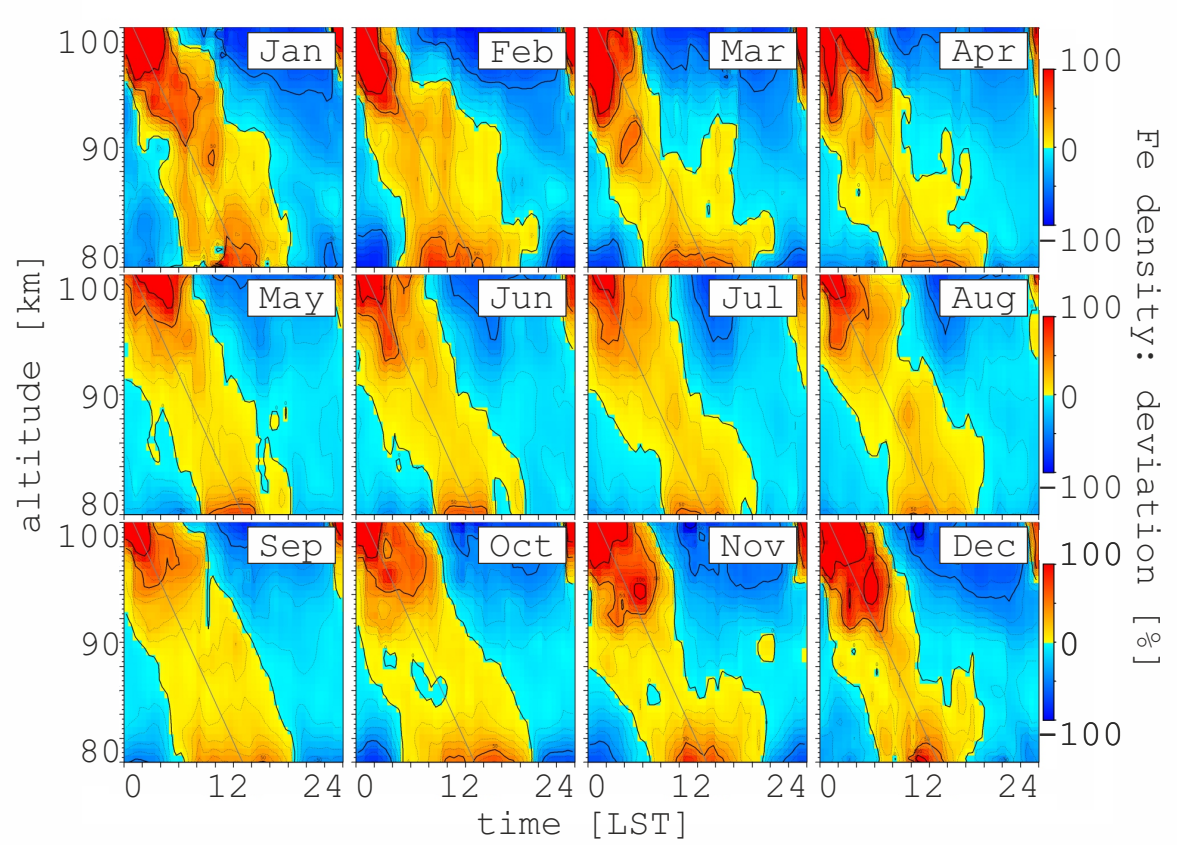

Figure 37: Diurnal deviation from mean Fe density per altitude at Davis, Antarctica (69°S), averaged for all twelve months 12/2010–12/2012. The tidal features in Fe density show the same phase structure throughout the year, despite the pronounced seasonal variability of solar irradiance at polar latitudes. *Preliminary results. Contact author before usage of data. CC BY 4.0*

20 Constant Fe tides in the polar MLT

Fe density measurements at Davis, Antarctica (69°S) have revealed a surprisingly regular tidal structure. All months show the same phase progression, regardless of changes in solar irradiance throughout the year. WACCM-Fe model calculations are currently being analysed to explain these observations.

Observations with the mobile IAP Fe lidar by ***Lübken et al.*** [2011] have revealed strong thermal tides at Davis, Antarctica (69°S). The observed tides had a similar phase progression in temperatures and Fe densities (see Section 12). New analysis shown in Figure 37 surprisingly reveal a very constant tidal signature in Fe densities throughout all months of the year, which has neither been observed before nor predicted by model calculations.

Part of the explanation is presumably the very regular occurrence of sporadic Fe layers (Fe_S) at Davis, which is a further unexpected and new observation: Fe_S were observed to predominantly occur between 18 UT and 22 UT (23 LST and 3 LST). Fe_S are usually first seen at altitudes of around 105 km to 125 km shortly before 18 UT (23 LST), on rare occasions even higher. As are descending in time, they were observed to usually reach an altitude of 100 km at around 19±1 UT (between 23 LST and 1 LST). This probably explains the high densities at the top end of Figure 37.

Furthermore, the strong photolysis of FeOH causes a regular creation of neutral Fe atoms on the bottomside of the Fe layer, centered around local noon (see Section 5). This effect can explain higher densitites at altitudes around 80 km at around 12 LT in Figure 37. However, the sun does not set at Davis during the summer months, so this effect allone cannot explain the behviour. Moreover, the temperature dependence of the neutral Fe layer is strongly reduced during the polar summer months as FeOH is fully depleted (see Section 7). Temperature tides as reported by ***Lübken et al.*** [2011] (see Section 12)

are hence presumbaly not the cause for an enhancement of Fe. The most likely explanation of the constant phase structure in Figure 37 is therefore a tidally driven downward movement of Fe atoms created through the recombination of FeO^+ in regularly occuring Fe_S.

The analyses presented in Section 13 are currently being extended to model runs of WACCM-Fe, including new reaction rates as determined by ***Viehl et al.*** [2016a] (see Section 6). The new analyses will also allow to directly compare the temperature influence on the chemistry.

21 The mesospheric Fe layer in Antarctica and the Arctic

Observations of the mesospheric Fe layer in Antarctica and the Arctic show several common characteristics but also differences. These differences allow to further investigate the physics and chemistry of the MLT region.

Observations with the mobile IAP Fe lidar at Davis (69°S, 78°E) in Antarctica and ALOMAR (69°N, 16°E) in the Arctic allow comparing differences and similarities in Fe density. Figure 38 shows the mesospheric Fe layer at Davis (top) and ALOMAR (bottom), centred around the respective summer solstice. All available observations (listed in Figure 42 in Appendix C) contribute to these plots. Generally, both stations experience higher densities, a larger RMS layer width, and a lower centroid altitude during winter than during summer. However, average densities at Davis are significantly larger during the winter months than at ALOMAR. Furthermore, although densities in the middle of summer are very low at ALOMAR, the extremely low densities observed at Davis have not yet been observed in the NH. Both polar regions show an uplift of the Fe layer towards to and during the summer months. However, the upper edge of the layer is only clearly elevated at Davis. At ALOMAR, a dip at the top edge of the layer is observed.

As mentioned in Section 4, Davis and ALOMAR have been specifically chosen for the observations with the mobile IAP Fe lidar not only because of the good infrastructure and co-located instruments, but also because they are at nearly exactly opposite latitudes of the globe. This allows for particularly valuable interhemispheric comparisons. The distance of both observational sites from the respective Geographic Poles (Davis: 2 381 km, ALOMAR: 2 303 km) differs somewhat less than the different geomagnetic latitudes. Davis is currently located at a distance of about 2 505 km from the South Magnetic Pole, while ALOMAR is slightly further away at around 2 702 km from the North Magnetic Pole. This difference may seem small, but a change of around 200 km means that Davis is located in the active region of the auroral oval more often than ALOMAR. Note that the geomagnetic distances were calculated for 2015 and the North Magnetic Pole currently moves north-east, increasing the distance to ALOMAR by about 1 km to 5 km per year.

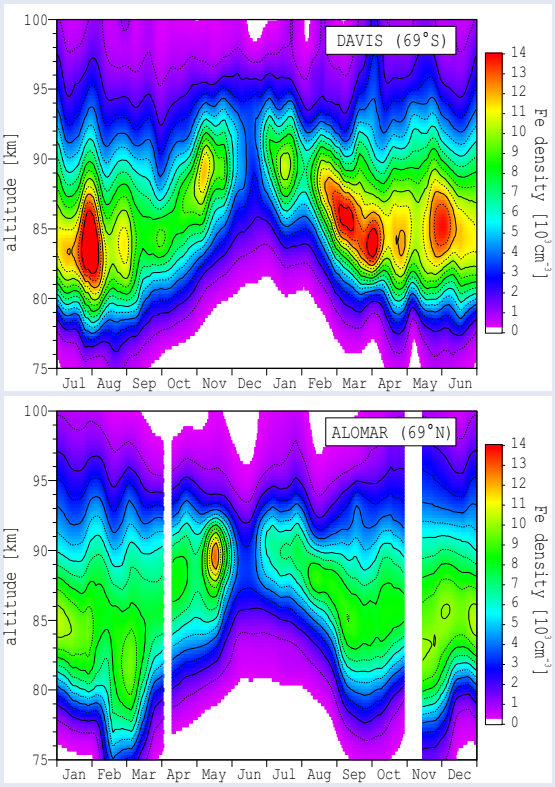

Figure 38: Seasonal variation of the Fe layer at Davis (69°S) and ALOMAR (69°N), centered around the respective summer solstice. Measurements in both hemispheres show an uplift of the layer during the summer months when densities are generally lower than during winter. *CC BY 4.0*

The geomagnetic differences may explain why lower absolute densities are generally observed at ALOMAR compared to Davis, transporting more FeO+ and other ionised species to the site. Furthermore, the recombination process $FeO^+ + e^- \longrightarrow Fe + O$ may be more efficient during more regular (electron) Auroras at Davis.

The meteoric input is roughly anti-symmetric for Davis and ALOMAR, leading to a similar cosmic dust input during the respective seasons [*Fentzke and Janches*, 2008]. However, the also experience differences in the meteoric input function to the respective seasons due to the Earth's orbital position throughout the year and the orbit inclination.

Additionally, the both polar hemispheres experience a different activity (and spectrum) of gravity and planetary waves in the MLT. Further differences of the hemispheres include the occurrence of mesospheric ice particles (PMC/NLC, PMSE), and different pressure altitudes due to a stronger contraction of the atmosphere in the colder middle atmosphere of the Southern Hemisphere. A detailed comparison of the data of the two polar locations in combination with comprehensive 3D atmospheric modelling will allow investigating the physics, chemistry, and meteoric input in more detail. The measurements in the Artic are currently ongoing, filling the data gaps and increasing the measurement statistics at ALOMAR.

22 Intraday variability of the Fe layer and short term influence of ice particles

Previous studies have focused on longer-term investigations of the mesospheric metal layers. Short-term analyses of metal layer variations on time scales of minutes to days allow investigating metal atom transport, interaction with mesospheric ice particles, gravity wave activity, and mixing processes in more detail.

Analyses by ***Viehl et al.*** [2015] have shown that a possible uptake of Fe atoms on ice particles (PMC) has no dominating effect on the seasonal variation of the Fe layer (Section 10). However, ***Viehl et al.*** [2015] note that a very localised uptake during the day as reported by *Plane et al.* [2004] might have a measurable short-term effect in addition to vertical and mean meridional transport processes, as well as all chemical factors, involved [***Viehl et al.***, 2016b]. Although this uptake effect is not large enough to dominate the overall mean density of the layer, a quantification seems necessary to fully understand the variability of the Fe layer, for example to allow for gravity waves analyses.

Figure 39 shows an example of the intra-day variability of the Fe layer (blue) and ice particles observed as PMSE (red) during a measurement at Davis (69°S) shortly before the SH summer solstice. Fe densities below ~2 000 cm^{-3} are observed before 22 UT. After 22 UT, high Fe densities up to 16 000 cm^{-3} are observed in an altitude range between 86 km and 96 km. The area of high Fe density within the Fe layer generally decreases in altitude with time. No NLC were recorded throughout the duration of this measurement. Several interesting points can be drawn from a preliminary of this plot.

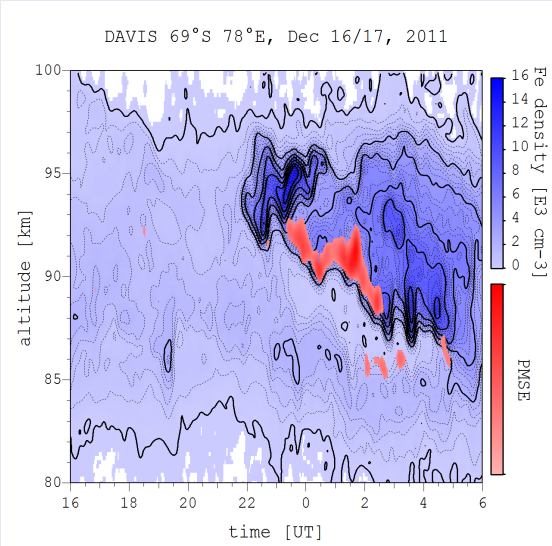

Figure 39: Close-up of the Fe layer (blue) and PMSE (red). The Fe layer shows considerable variation throughout the day with very low densities before 22 UT and high densities thereafter. PMSE occur when high densities are observed and tend to be located at the lower edge of areas with high Fe density. The anti-correlation of low column densities and ice particle occurrence has been analysed by ***Viehl et al.*** [2015, 2016b] on seasonal scales. An analysis of the intra-day variability could help to further understand the interaction of ice particles and metal atoms in the MLT region and quantify heterogeneous uptake. *Preliminary results. Contact author before usage of data. CC BY 4.0*

First, no mesospheric ice particles (neither NLC nor PMSE) were observed during the first part of the measurement. In line with the seasonal observations by ***Viehl et al.*** [2015, 2016b], column densities (not shown) in this example are low although no ice particles are observed. On the other hand, column densities are high throughout the second part of the observation when mesospheric ice particles were detected through PMSE observations.

Second, PMSE were observed between around 87 km and 93 km at the lower edge of the area of high Fe density, and both Fe density and PMSE show considerable variability. This variability could be caused by gravity waves. The main PMSE layer additionally shows a general downward trend. A second layer of weaker PMSE is further observed at around 86 km altitude below the main PMSE layer.

Third, the altitudes above 94 km show a pronounced variability which can most likely only be explained by strong horizontal transport or the recombination of FeO^+ to Fe in sporadic Fe layers (Fe_S). However, it is noteworthy that at altitudes above 94 km PMSE may not be observed due to the increased kinematic viscosity, as the energy dissipation rate required to achieve a certain radar volume reflectivity increases strongly above 90 km altitude [*Lübken*, 2013]. Ice particles could still be present but not cause PMSE. However, the presence of ice is not very likely, as the temperature at this altitude also increases significantly. In fact, the measurements show temperatures above 94 km were generally above the freezing point on this day, see left panel of Figure 36.

In many available observations, PMSE track the lower edge of Fe layer where a high gradient of Fe is observed. However, Fe densities are in general not lower after the local occurrence of PMSE in line with the results by ***Viehl et al.*** [2015]. In fact, the highest densities of the measurement in Figure 39 were observed when PMSE are present. Studies have focussed on the aspect of ice particles necessary for PMSE observation. It might be possible that the combination of metal layer and PMSE observations could also give an insight into the occurrence of turbulence and wave breaking in the MLT. Detailed intra-day analyses of Fe density and PMSE observations will help to understand all short-term variations of the metal density as well as their relation and importance to the occurrence of PMC.

An important point to note is that although lidar and radar measurements have a high vertical and temporal resolution, they only provide a one-dimensional measurement in time. Full 4D modelling of the dependent metal chemistry and transport, as well as aerosol movement, are needed to investigate a potential uptake along the track of PMC particles. Additional 4D observations of the mesospheric Fe layer with tilted lidars could provide a much deeper insight into these processes and other phenomena.

23 Lidar observations of meteor smoke particles

The polymerisation of metallic compounds in the MLT produces meteoric smoke particles (MSP). MSP are important for the nucleation of ice particles in the MLT region and may affect the global climate through interactions in the stratosphere and deposition in the oceans. Observations with the mobile IAP Fe lidar may for the first time have directly measured MSP in the middle atmosphere.

Metallic compounds in the MLT region are presumed to polymerise to meteoric smoke particles (MSP) [*Hunten et al.*, 1980; *Kalashnikova et al.*, 2000]. On the one hand, MSP act as a sink for all mesospheric metals, balancing the input of the meteoric source [*Plane et al.*, 2015]. Their formation is hence important to understand the morphology of the metal layers (e.g., see Section 2.3). On the other hand, MSP are thought to have important impacts not only on the MLT region but also on the atmosphere below and potentially even for the global climate system. It is widely assumed hat MSP are the embryonic particles for heterogeneous nucleation of polar mesospheric clouds [e.g., *Gumbel and Megner*, 2009]. Their abundance or absence can hence influence the nucleation rate of ice particles (PMSE and NLC/PMC) in the MLT region. Furthermore, MSP are thought to interact with sulphuric and nitric acid in the stratosphere [*Saunders et al.*, 2012; *Frankland et al.*, 2015] and might hence also influence catalytic ozone depletion on polar stratospheric clouds. As mentioned in Section 7, MSP may even fertilise phytoplankton and hence have an impact on the biological activity and thus the CO_2 absorbing potential of the oceans [*Johnson*, 2001; *Dhomse et al.*, 2013].

To date, no direct observations of MSP with lidars were successful, as the particles are presumably smaller than 5 nm and their Mie signal is hence very week and difficult to distinguish from the background radiation with ground-based or satellite-borne instruments. A method to detect the Mie signal of very small particles in the stratosphere and mesosphere was introduced by *Viehl* [2010] in a Diplomarbeit (German equivalent of a Master's thesis). Narrowband high power laser sources as operated in the mobile IAP Fe lidar can be used to scan the Mie profile of the MSP. A high resolutive con-

focal Fabry-Perot interferometer (CFPI) with high finesse and a FWHM on the order of the expected Mie spectrum (~5 Mhz, i.e. 0.01 pm at 772 nm) can then be used to deconvolve the spectral components of the Mie scattering as well as the laser and the optical filter components from the retrieved signal. However, even small mechanical vibrations inherent to common lidar instruments or caused by sound waves or wind disturbances will derogate the CFPI's spectrum and require very fast active stabilisation. The necessary fast stabilisation was successfully demonstrated by *Viehl* [2010] using a distributed feedback (DFB) laser stabilised to a compact Rubidium saturation spectroscopy and the Pound-Drever-Hall technique [*Drever et al.*, 1983]. The key for atmospheric MSP detection is to eliminate disturbances on the final detector, which can be achieved by employing a slanting passage through the CFPI and using a pickup mirror for the stabilising DFB laser, hence achieving a sufficient signal-to-noise ratio for the atmospheric signal [*Viehl*, 2010].

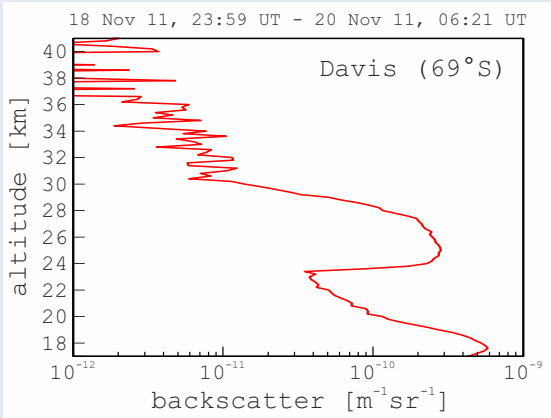

Figure 40: Aerosol measurements with the CFPI of the mobile IAP Fe lidar at Davis, Antarctica. Meteor smoke particles are thought to have been observed at an altitude of 24–30 km above the stratospheric Junge layer. *Preliminary results. Contact author before usage of data. CC BY 4.0*

An aerosol detection branch with a CFPI as described by *Viehl* [2010] was implemented in the detection bench of the mobile IAP Fe lidar in 2010. It has been in parallel operation during most measurements since that time, albeit mostly with reduced capability due to the optimisation of the laser cycle for MLT temperature measurements. Nevertheless, preliminary analysis of mesospheric and upper stratospheric aerosol data obtained with the system at Davis, Antarctica (69°S) indicate faint but lasting aerosols originating at MLT altitudes.

The observed aerosols seem to be primarily created during autumn and descend towards summer. Figure 40 shows an example of measurements with the presumed MSP at altitudes between 24 km and 30 km. A particularity of the measurements of the example shown is that the continuous stratospheric Junge layer had dropped to below 24 km during the days around the observation, enabling to see the presumed MSP very clearly. These results are currently being confirmed and compared to 3D WACCM calculations of MSP creation and transport in cooperation with the School of Chemistry of the University of Leeds.

24 Comparison of Fe lidar and OH spectrometer temperature observations

Temperature measurements of the mobile IAP Fe lidar at Davis, Antarctica are compared to co-located OH(6-2) Czerny-Turner spectrometer measurements. The temporal evolution of the two temperature datasets is strikingly similar but shows a persistent temperature bias. The joint measurements with high precision open up the possibility to investigate the fundamental temperature retrieval of OH* temperature measurements.

Airglow emissions by excited hydroxyl (OH) atoms in the OH layer at around 86 km altitude can be used to observe MLT temperatures remotely. Ground-based spectrometers provide no altitude resolution but can determine temperatures during night-time or deep twilight conditions. These spectrometer measurements can be conducted continuously and have been performed for more than two decades, allowing trend analyses with high precision.

Measurements with the Davis Czerny-Turner spectrometer at the OH(6-2) band near 840 nm have been employed by *French and Klekociuk* [2011] to determine MLT temperature trends at Davis, Antarctica (69°S) between 1995 and 2011. That study found a solar cycle dependence of 4.8±1.0 K/100 SFU and a long-term cooling trend of 1.2±0.9 K/decade (R^2=0.70). Absolute OH temperature measurements require several assumptions about the emission altitude and the transition probabilities of the excited hydroxyl states. The observations at Davis

have been validated by comparison to satellite measurements *French and Mulligan* [2010] using transition probabilities by *Langhoff et al.* [1986].

During the 2011 winter, both the Davis OH(6-2) Czerny-Turner spectrometer and the mobile IAP Fe lidar have obtained full seasonal coverage of MLT observations at the same location. The different operational principles cause a slightly different temporal coverage of the instruments: due to the warm-up process of up to 1 h and general instrument deterioration considerations, the mobile IAP Fe lidar is only ever switched on for measurement windows which are expected to last several hours. The passive OH spectrometer, however, also observes temperatures through thin cloud cover or during short periods of clear sky in otherwise cloudy tropospheric weather conditions. The mobile Fe lidar, on the other hand, can measure during full daylight. The OH spectrometer only measures during periods of darkness or deep twilight. These instrument differences cause a further and even larger deviation in observational hours in early and late winter, when the sun is not entirely below the horizon.

Figure 41 shows temperature observations by the Davis OH(6-2) Czerny-Turner spectrometer (orange) and the mobile IAP Fe lidar during the joint measurements in 2011. Lidar temperatures are calculated as a weighted composite at the altitudes of the OH layer. The mean vertical weighting profile (VERm) was taken from TIMED/SABER observations [*French and Mulligan*, 2010] and calculated for two cases, assuming a peak emission altitude at 85.6 km (green) and 84.5 km (blue), respectively. As can be expected from the winter state of the MLT, lidar temperatures are generally higher at lower altitudes. All temperatures shown are smoothed with a 14-day Hann window.

Two important features emerge from the instrument comparison in Figure 41. First, absolute temperature measurements show an average offset of around 9.2 K and 7.8 K when assuming peak emission altitudes at 85.6 km and 84.5 km, respectively. This bias is significant (error bars not shown). Second, temperature measurements from both instruments show a strikingly similar temporal evolution. When artificially shifting one of the temperature sets by 8 K (grey), similarities and differences can be investigated more easily. Deviations are largest at the beginning and end of winter when the periods of observation differ the most.

The strong similarity of the temporal evolution confirms the observations of the co-located instruments. The significant absolute bias, however, can only be explained by a systematic error in the temperature retrieval of at least one of the instruments.

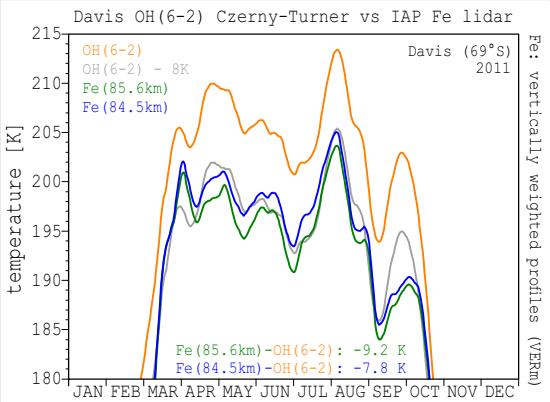

Figure 41: Temperature measurements by the Davis OH(6-2) Czerny-Turner spectrometer (orange) and the mobile IAP Fe lidar at Davis, Antarctica (69°S) during the 2011 winter. OH layer emissions are assumed to peak at around 86 km altitude. Lidar temperatures are calculated for mean OH layer altitude distributions taken from SABER observations (VERm) at around 85.6 km (green) and 84.5 km (blue). The offset between the datasets is significant (error bars not shown). The temperatures agree within the error bars when a bias of 8 K is subtracted (grey). *OH(6-2) data courtesy of Dr W. John R. French, AAD. Preliminary results. Contact author before usage of data. CC BY 4.0*

As described in Section 3, the mobile IAP lidar's temperature retrieval has been validated against other resonance lidars, as well as falling spheres, and can spectrally determine deviations from the LTE or other inconsistencies in the form of the resonance spectrum. Furthermore, if temperatures by the mobile IAP Fe lidar were to be offset by around −8 K to −10 K, temperatures during summer would no longer be in agreement with the observations of mesospheric ice particles. Indeed, PMSE have been observed exactly during the periods and at altitudes of the super-saturated regions shown in the left panel of Figure 36.

The temperature retrieval of the Davis OH(6-2) Czerny-Turner spectrometer has been compared to satellite observations by Aura(EOS)/MLS and TIMED/SABER. *French and Mulligan* [2010] find a systematic trend when comparing against SABER v1.07 data, and a warm bias of around 10 K of OH

temperatures compared to MLS v2.2. However, a comparison of Davis OH(6-2) temperatures with more recent SABER v2.0 and MLS v3.3 datasets shows further improved agreements: the previously reported temperature trend of SABER v1.07 is no longer observable in SABER v2.0, and absolute OH(6-2) temperatures now only have a positive bias of around 2 K compared to MLT v3.3 (*W. John R. French, AAD, personal communication*).

Both instruments, therefore, appear not only to be precise, but accurate in their temperature retrieval. However, as Section 19 briefly mentioned, both TIMED/SABER and Aura(EOS)/MLS temperature climatologies have been successfully used for a range of purposes, but also have limitations in their application due to the low vertical and temporal resolution. A warm temperature bias of OH(6-2) temperature therefore currently seems more likely than a negative temperature bias of the mobile IAP Fe lidar.

Indeed, results by *Noll et al.* [2015, 2016] suggest that OH(6-2) could show a positive temperature bias of more than 5 K due to incorrect Einstein coefficients employed by *Langhoff et al.* [1986] and others. Temperatures determined by the Davis OH(6-2) Czerny-Turner spectrometer could, therefore, be significantly lower when being recalculated using revised transition probabilities. The common volume measurements at Davis could be an experimental confirmation of a revised OH temperature retrieval, achieved by comparing a ground-based OH(6-2) spectrometer, not to a satellite, but a high-resolution resonance lidar.

Theoretical considerations by *Grygalashvyly et al.* [2014] and recent observational results by *Teiser and von Savigny* [2016] for the Northern Hemisphere additionally suggest that the altitude of the OH layer may have previously been determined to high at polar latitudes. These results make a peak OH emission altitude of around 84.5 km or even lower likely during the polar winter.

These results and hypotheses need to be tested further. However, a detailed comparison of lidar and spectrometer data places important constraints to the uncertainties of the existing studies. The further analysis of Fe lidar and OH spectrometer data could, therefore, have a very significant influence on the calculation of all temperatures derived from OH* emissions and the trends derived from their analyses.

25 Outlook

Measurements with the mobile IAP Fe lidar continue in the Artic at ALOMAR (69°N). Further analyses of the obtained datasets with co-located instruments may allow insights into ion-molecule chemistry and sporadic (Fe_S and E_S) layers, the magnetosphere, gravity wave activity, and the mixing of trace species. Attempts are being undertaken to detect additional metallic species such as nickel (Ni) or aluminium(II) oxide (AlO), as well as helium (He) in the upper atmosphere. Ongoing technical developments aim to simplify measurement operations further and enable nearly fully automated remote measurements. A newly developed technique will in the near future allow improved lidar wind observations.

The dataset obtained by the mobile IAP lidar is not yet fully analysed, and the publication of results is still ongoing. Several preliminary results of analyses have been briefly described in Sections 19 to 24. Moreover, the datasets of temperatures, Fe densities, and aerosols in the middle atmosphere are still growing as the measurements of the mobile IAP Fe lidar are continuing at ALOMAR (69°N). As section 4 noted, a host of instruments probing various aspects of the MLT region are operated at Davis and ALOMAR. The analyses of the joint datasets will be subject to future studies.

Comparisons with ionosonde, magnetometer, and riometer data

The observations at Davis have shown a very regular occurrence of sporadic Fe layers (Fe_S) at specific local solar times around 2 LST to 3 LST. Fe_S are thought to be composed of ionic species (Fe^+, Mg^+) and known to be correlated to sporadic *E* layers (E_S) *MacDougall et al.* [2000]; *Delgado et al.* [2012, e.g.,]. These observations underline the high importance of ion-molecule chemistry for the metal layers. Atmospheric tides further cause a strong vertical coupling of the neutral atmosphere and the ionosphere [*England et al.*, 2006]. Lidar observations of mesospheric metals can, therefore, provide insights into the physics and chemistry of E_S.

Measurements of E_S as well as electron densities by an ionosonde are available at Davis. A detailed comparison with Fe lidar data might provide fur-

ther insight into the dynamics of the sporadic layers. Additionally, co-located measurements with a magnetometer and a riometer (SHIRE) at Davis allow the analysis of the geomagnetic influence on the metal layers. Such studies may provide further insights into the ion-molecule chemistry and transport processes, particularly in the polar regions.

Measurement of further species

During the past decades, only a handful of metals and other trace species in the MLT have been successfully probed by lidars on a continuous basis (Fe, Na, K, and Ca/Ca^+). As briefly described in Section 2.4, this is mainly due to a lack of suitable transitions. However, it may be possible to probe some additional species. *Collins et al.* [2015] recently reported first measurements of the mesospheric Ni layer. However, these measurements have not yet been extended to seasonal scales or reproduced by other groups. Additionally, aluminium(II) oxide (AlO) and helium (He) should also have sufficiently large backscatter coefficients at reasonably high number densities. It might be possible to probe the species by ground-based lidars in the near future.

The resonance lines of AlO and Ni are outside the spectral range of the mobile IAP Fe lidar'a alexandrite laser but can be probed with dye lasers. Such observations are interesting for several reasons. First, such analyses allow studying the chemistry of these species. Second, as the knowledge about further metal layers places additional constraints on 3D atmospheric chemistry models, it can improve the overall representation of the MLT. Third, additional metals observations can improve the analysis of the meteoric ablation processes and cosmic dust evolution. Observations of AlO would additionally allow very good estimates of atomic O, which is crucial to the chemistry of the MLT.

Furthermore, the observation of He could allow probing temperatures up to very high altitudes in the thermosphere. Continuous improvements of mobile alexandrite lidars will soon allow the simultaneous measurement of 2–3 species (Fe, K or/and He) as well as an improved detectability of aerosol particles in the mesosphere and stratosphere.

Technical improvements

Continuous technical developments aim at further simplifying the operation of the mobile IAP Fe lidar. With an increasingly higher degree of automation, more measurement hours can be obtained. Additional improvements are performed to increase the reliability of all components, including the infrastructure components, to ensure little downtime and prolonged maintenance intervals. These advantages are particularly important when operating at remote locations.

The recent development of a new diode-pumped alexandrite laser will allow very small, autonomously operating lidar systems capable of probing the MLT region in four dimensions. Such instruments not only allow improved resolution and coverage of the metal layers but also allow to discern chemical and transport processes and directly probe the diffusion of ablating meteors.

Two important aspects of the successful operation of the mobile IAP Fe lidar are the real-time assessment of the laser spectrum and the ultra-fast data compression of the retrieved signal, allowing an instant feedback of the atmospheric signal to the laser. Both techniques have been described in a patent by *Höffner* [2015].

A novel method to determine wind speeds in the middle atmosphere with lidars has recently been submitted as a patent by ***Höffner et al.*** [2016], currently pending in Germany and to be submitted in Europe and the USA. The method will allow significantly improved lidar measurement of winds from the troposphere to the mesosphere due to a drastically increased SNR compared to other techniques. These examples show the technical spin-off capability of basic atmospheric research.

Ongoing measurements

Measurements with the mobile IAP Fe lidar are currently continuing at ALOMAR (69°N). The temperature climatology will complement previous results by *Lübken* [1999] obtained at the same location. Additionally, the co-located instruments at ALOMAR, as well as the sounding rocket facilities at the ASC, will allow an even more detailed analysis of various atmospheric properties. The upcoming measurement campaigns and analyses may well provide further unique insights into the physics and chemistry of the MLT and its role in the global atmosphere.

Appendices

Appendix A: Abbreviations

AAD	Australian Antarctic Division
AIM	Aeronomy of Ice in the Mesosphere
ALOMAR	Arctic Lidar Observatory for Middle Atmosphere Research
ANARE	Australian National Antarctic Research Expeditions
APD	Avalanche Photodiode
ASC	Andøya Space Center
B3LYP	Becke Three-Parameter Lee-Yang-Parr
BMBF	Bundesministerium für Bildung und Forschung
BOM	Bureau of Meteorology (Australia)
CAM	Coulomb-Attenuated Method
CFPI	Confocal Fabry-Perot Interferometer
CIRA	COSPAR International Reference Atmosphere
CODITA	Cosmic Dust in the Terrestrial Atmosphere
COSPAR	Committee on Space Research
DFB	Distributed Feedback
DFG	Deutsche Forschungsgemeinschaft
DFT	Density Functional Theory
ECMWF	European Centre for Medium-Range Weather Forecasts
EOS	Earth Observing System
ERC	European Research Council
ESM	Elevated Summer Mesopause
FOV	Field of View
FWHM	Full Width at Half Maximum
GOMOS	Global Ozone Monitoring by Occultation of Stars
GPS	Global Positioning System
GSWM	Global Scale Wave Model
GWPED	Gravity Wave Potential Energy Density
HF	Hartree-Fock
HF	High Frequency
IAP	Leibniz-Institute of Atmospheric Physics at the University of Rostock
IR	Infrared
KMCM	Kühlungsborn Mechanistic General Circulation Model
LBO	Lithium Triborate
LIDAR	Light Detection and Ranging
LIMA	Leibniz-Institute Middle Atmosphere Model
LST	Local Solar Time
LT	Local Time
LTE	Local Thermodynamic Equilibrium
MAARSY	Middle Atmosphere ALOMAR Radar System
MaTMeLT	Mixing and Transport in the Mesosphere/Lower Thermosphere
MERRA	Modern-Era Retrospective Analysis for Research and Application
MF	Medium Frequency
MLS	Microwave Limb Sounder
MLT	Mesosphere–Lower Thermosphere
MST	Mesosphere, Stratosphere, Troposphere
MSP	Meteor Smoke Particles
NASA	National Aeronautics and Space Administration (US)
NCAS	National Centre for Atmospheric Science (UK)
NCEP	National Center for Environmental Prediction (US)

NH	Northern Hemisphere
NLC	Noctilucent Cloud
NOAA	National Oceanic and Atmospheric Administration (US)
NRL	Naval Research Laboratory (US)
NRLMSISE	NRL Mass Spectrometer and Incoherent Scatter Radar Extended
OSIRIS	Optical Spectrograph and Infrared Imager System
PACOG	Processes and Climatology of Gravity Waves
PMC	Polar Mesospheric Cloud
PMSE	Polar Mesospheric Summer Echoes
PMT	Photomultiplier Tube
RMR	Rayleigh-Mie-Raman
RMS	Root Mean Square
RSV	Research and Supply Vessel
ROMIC	Role of the Middle Atmosphere in Climate
SABER	Sounding of the Atmosphere Using Broadband Emission Radiometry
SCIAMACHY	Scanning Imaging Absorption Spectrometer for Atmospheric Chartography
SFU	Solar Flux Unit
SH	Southern Hemisphere
SHG	Second Harmonic Generation
SHIRE	Southern Hemisphere Imaging Riometer Experiment
SNR	Signal-to-Noise Ratio
SOFIE	Solar Occultation for Ice Experiment
SPVBD	Stratospheric Polar Vortex Breakdown
TIMA	Trends in the Middle Atmosphere
TIMED	Thermosphere Ionosphere Mesosphere Energetics and Dynamics
UT	Universal Time
UV	Ultra-Violett
TD	Time Dependent
VHF	Very High Frequency
WACCM	Whole Atmosphere Community Climate Model

Appendix B: Rate coefficients

	reaction	rate coefficient[a]	source
	Neutral Chemistry		
R1	$Fe + O_3 \longrightarrow FeO + O_2$	$2.9 \times 10^{-10} \exp(-174/T)$	*Helmer et al.* [1998]
R2	$FeO + O \longrightarrow Fe + O_2$	$4.6 \times 10^{-10} \exp(-350/T)$	*Self and Plane* [2003]
R3	$FeO + O_3 \longrightarrow FeO_2 + O_2$	$3.0 \times 10^{-10} \exp(-177/T)$	*Rollason and Plane* [2000]
R4	$FeO + O_2 + M \longrightarrow FeO_3 + M$	$4.4 \times 10^{-30} \exp(T/200)^{0.606}$	*Rollason and Plane* [2000]
R5	$FeO_2 + O \longrightarrow FeO + O_2$	$1.4 \times 10^{-10} \exp(-580/T)$	*Self and Plane* [2003]
R6	$FeO_2 + O_3 \longrightarrow FeO_3 + O_2$	$4.4 \times 10^{-10} \exp(-170/T)$	*Self and Plane* [2003]
R7	$FeO_3 + O \longrightarrow FeO_2 + O_2$	$2.3 \times 10^{-10} \exp(-2310/T)$	*Self and Plane* [2003]
R8	$FeO_3 + H_2O \longrightarrow Fe(OH)_2 + O_2$	5×10^{-12}	*Self and Plane* [2003]
R9	$FeO + H_2O + M \longrightarrow Fe(OH)_2 + M$	$5 \times 10^{-28} \exp(200/T)^{1.13}$	*Rollason and Plane* [2000]
R10	$Fe(OH)_2 + H \longrightarrow FeOH + O_2$	$3.3 \times 10^{-10} \exp(-302/T)$	*Jensen and Jones* [1974]
R11	$FeO_3 + H \longrightarrow FeOH + O_2$	$3 \times 10^{-10} \exp(-796/T)$	*Plane et al.* [1999]
R12a	$FeOH + H \longrightarrow Fe + H_2O$	$2 \times 10^{-12} \exp(-600/T)$	***Viehl et al.*** [2016a]
R12b	$FeOH + H \longrightarrow FeO + H_2$	$6 \times 10^{-11} \exp(-1200/T)$	***Viehl et al.*** [2016a]
R13	$FeOH + FeOH \longrightarrow (FeOH)_2$	9.0×10^{-10}	*Feng et al.* [2013]
R14	$Fe \longrightarrow FePMC$	$4.9 \times T^{0.5} \times VSA^{b}_{PMC}$	*Feng et al.* [2013]
R15	$FeOH \longrightarrow FePMC$	$4.3 \times T^{0.5} \times VSA_{PMC}$	*Feng et al.* [2013]
R16	$Fe(OH)_2 \longrightarrow FePMC$	$3.8 \times T^{0.5} \times VSA_{PMC}$	*Feng et al.* [2013]
R17	$FeO_3 \longrightarrow FePMC$	$3.6 \times T^{0.5} \times VSA_{PMC}$	*Feng et al.* [2013]
	Ion-Molecule Chemistry		
R18	$Fe + NO^+ \longrightarrow Fe^+ + NO$	9.2×10^{-10}	*Rutherford and Vroom* [1972]
R19	$Fe + O_2^+ \longrightarrow Fe^+ + O_2$	1.1×10^{-9}	*Rutherford and Vroom* [1972]
R20	$Fe^+ \longrightarrow FePMC$	$4.9 \times T^{0.5} \times VSA_{PMC}$	*Feng et al.* [2013]
R21	$Fe^+ + O_3 \longrightarrow FeO^+ + O_2$	$7.6 \times 10^{-10} \exp(-241/T)$	*Rollason and Plane* [2000]
R22	$FeO^+ + O \longrightarrow Fe^+ + O_2$	3.0×10^{-11}	*Woodcock et al.* [2006]
R23	$Fe^+ + N_2 + M \longrightarrow Fe^+ \cdot N_2$	$4.1 \times 10^{-30} \exp(T/300)^{-1.52}$	*Vondrak et al.* [2006]
R24	$Fe^+ \cdot N_2 + O \longrightarrow FeO^+ + N_2$	5×10^{-11}	*Rollason and Plane* [1998]
R25	$FeO_2^+ + O \longrightarrow FeO^+ + O_2$	5×10^{-11}	*Rollason and Plane* [1998]
R26	$Fe^+ + O_2 + M \longrightarrow FeO_2^+ + M$	$8.3 \times 10^{-30} \exp(T/300)^{-1.86}$	*Vondrak et al.* [2006]
R29	$FeO^+ + e^- \longrightarrow Fe + O$	5.5×10^{-7}	*Bones et al.* [2015]
R30	$FeO_2^+ + e^- \longrightarrow Fe + O_2$	$3 \times 10^{-7} \exp(T/200)^{0.5}$	*Plane et al.* [1999]
R31	$Fe^+ + e^- \longrightarrow Fe + h\nu$	$6.5 \times 10^{-12} \exp(T/300)^{0.51}$	*Nahar et al.* [1997]
	Photochemical Reactions		
R32	$FeOH + h\nu \longrightarrow Fe + OH$	6×10^{-3}	***Viehl et al.*** [2016a]
R33	$Fe + h\nu \longrightarrow Fe^+ + e^-$	5×10^{-7}	*Bautista et al.* [1998]

Table 1: Important reaction rate and photochemical coefficients of Fe containing species in the MLT region following *Plane et al.* [2015]. [a]Units: unimolecular [s^{-1}], bimolecular [cm^3 $molecule^{-1}$ s^{-1}], termolecular [cm^6 $molecule^{-2}$ s^{-1}]. [b]Volumetric Surface Area of the Polar Mesospheric Cloud.

Appendix C: Measurement statistics

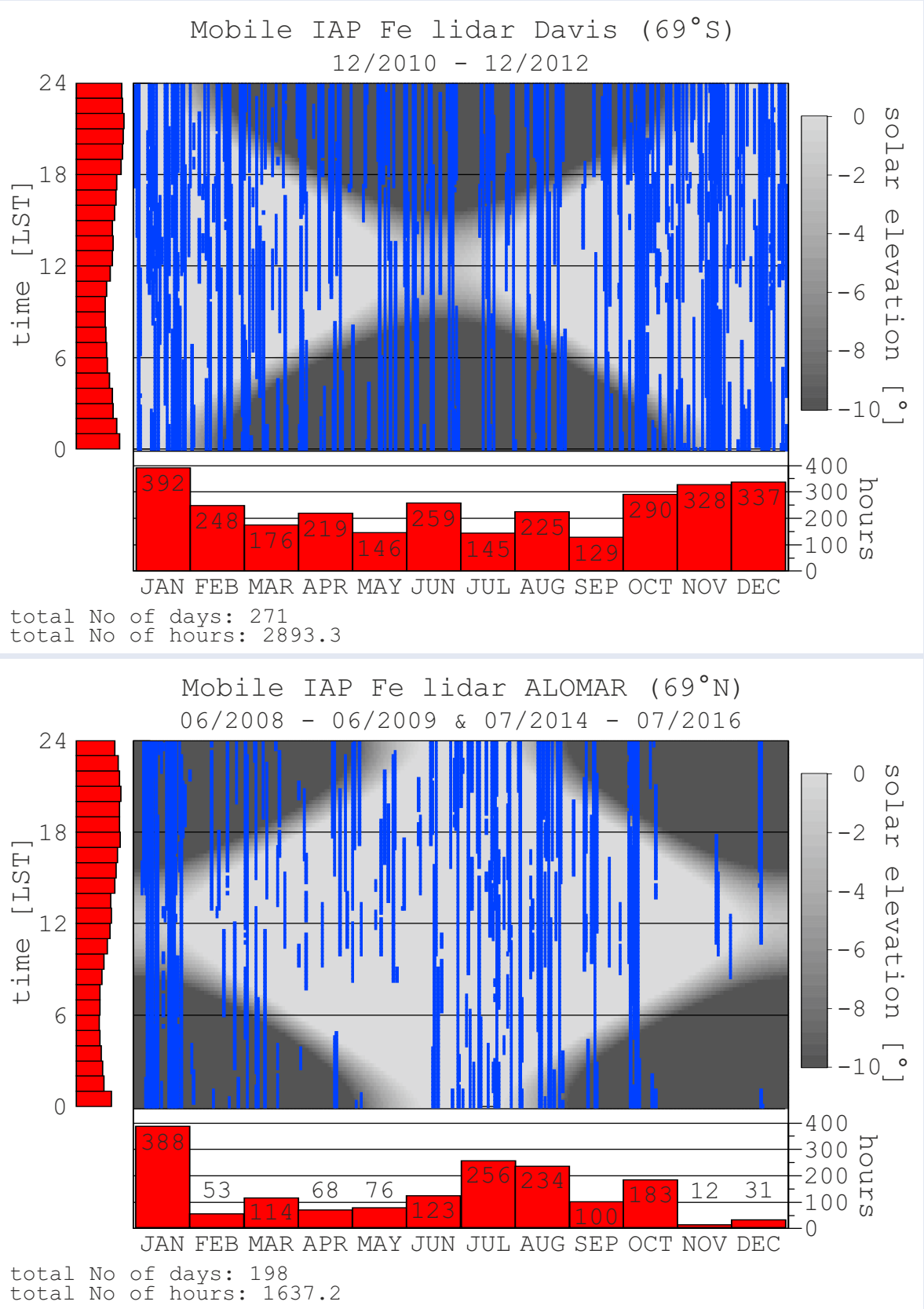

Figure 42: Measurements (blue) of the mobile IAP Fe lidar at Davis, Antarctica and ALOMAR, Norway: combined hours per month (red, lower), and distribution per time of the day (red, left). Polar regions experience periods of 24 h sunlight and darkness. The sun reaches the MLT down to a solar elevation (greyscale) of around -5°.

Appendix D: Copyright licenses

This thesis contains copyrighted material which is reprinted with permission under the licences in the following lists in Tables 2 and 3. All rights reserved by the respective licenced content publishers or authors. Commercial redistribution of the entire thesis or the copyrighted material not permitted. Please refer to the original copyright holder for personal copies of the published manuscripts or reuse of the figures.

The non-commercial publication of this thesis (print and electronic) is permitted for fair-use under the licences in Tables 2 and 3 via the institutional repositories, archives, and websites of the University of Rostock, Germany, the Leibniz-Institute of Atmospheric Physics at the University of Rostock in Kühlungsborn, Germany, and associated organisations. In accordance with section 5 of the *"Ordnung über die Bereitstellung von Pflichtexemplaren im Rahmen von Promotions- und Habilitationsverfahren an der Universität Rostock (Pflichtexemplarordnung)"* in the version of 18 February 2008 and as detailed in the *"Guidelines for the implementation of a doctoral degree procedure at the Faculty of Mathematics and Natural Sciences"* at the University of Rostock, Germany, this specifically includes the University Library of Rostock as well as the German National Library in Frankfurt am Main, Germany, and Leipzig, Germany.

Figure	Licenced content publisher and/or author(s)	Licence, year	Licence No/link
Fig. 1, Fig. 5, Fig. 8,	*Timo P. Viehl*	CC BY 4.0, 2016	CC BY 4.0
Fig. 2	*American Chemical Society*, *Plane et al.* [2015]	ACS AuthorChoice, 2015	ACS AC
Fig. 3, Fig. 7	*Timo P. Viehl*	CC BY-NC 4.0, 2012	CC BY-NC 4.0
Fig. 4	*Copernicus Publications*, *Vondrak et al.* [2008]	CC BY 3.0, 2008	CC BY 3.0
Fig. 6	*John Wiley & Sons Inc.*, *Feng et al.* [2013]	CC BY 3.0, 2013	CC BY 3.0
Fig. 9 (left), Fig. 12	*Dr Josef Höffner*	©print & electronic, 2016	
Fig. 9 (right), Fig. 10	*Timo P. Viehl*	CC BY 4.0, 2016	CC BY 4.0
Fig. 11	*Commonwealth of Australia, Australian Antarctic Data Centre*	CC BY 3.0, 2009	CC BY 3.0
Fig. 13,	*Raimund Wörl*	©print & electronic, 2015	
Fig. 14, Fig. 15, Fig. 16 Fig.,17	*John Wiley & Sons, Inc.* ***Viehl et al.*** [2016a]	©print & electronic, 2016	3811810557417
Fig. 18	*Timo P. Viehl*	CC BY 4.0, 2016	CC BY 4.0
Fig. 19, Fig. 20, Fig. 21	*Elsevier Ltd.*, ***Viehl et al.*** [2015]	©print & electronic, 2015	3811811217212
Fig. 22	*Elsevier Ltd.*, ***Viehl et al.*** [2016b]	©print & electronic, 2016	3811811335652
Fig. 23, Fig. 24, Fig. 25	*John Wiley & Sons, Inc.* ***Lübken et al.*** [2011]	©print & electronic, 2011	3811810418613
Fig. 26, Fig. 27	*John Wiley & Sons, Inc.* ***Feng et al.*** [2015]	CC BY 4.0, 2013	CC BY 4.0
Fig. 28, Fig. 29, Fig. 30	*John Wiley & Sons, Inc.* ***Kaifler et al.*** [2015]	©print & electronic, 2015	3811810781035
Fig. 31, Fig. 32	*Elsevier Ltd.*, ***Morris et al.*** [2012]	©print & electronic, 2012	3811820000346
Fig. 33, Fig. 34, Fig. 35, Fig. 36 (right)	*John Wiley & Sons, Inc.* ***Lübken et al.*** [2015]	©print & electronic, 2015	3811800959462
Fig. 36 (left)	*John Wiley & Sons, Inc.* ***Lübken et al.*** [2014]	©print & electronic, 2014	3811811028998
Fig. 37, Fig. 38, Fig. 39, Fig. 40, Fig. 41, Fig. 42	*Timo P. Viehl*	CC BY 4.0, 2016	CC BY 4.0

Table 2: Copyright licences and licence numbers for the reproduction of the figures in this thesis.

Manuscript	Licensed content publisher	License, year	License No/link
Viehl et al. [2016a]	*John Wiley & Sons, Inc.*	©print & electronic, 2016	3811800826840
Viehl et al. [2015]	*Elsevier Ltd.*	©print & electronic, 2015	3811801433629
Viehl et al. [2016b]	*Elsevier Ltd.*	©print & electronic, 2016	3812390399412
Lübken et al. [2011]	*John Wiley & Sons, Inc.*	©print & electronic, 2011	3811810278605
Feng et al. [2015]	*John Wiley & Sons, Inc.*	CC BY 4.0, 2015	CC BY 4.0
Morris et al. [2012]	*Elsevier Ltd.*	©print & electronic, 2012	3811801347630
Lübken et al. [2014]	*John Wiley & Sons, Inc.*	©print & electronic, 2014	3811800467340
Kaifler et al. [2015]	*John Wiley & Sons, Inc.*	©print & electronic, 2015	3811801162545
Lübken et al. [2015]	*John Wiley & Sons, Inc.*	©print & electronic, 2015	3811800959462

Table 3: Copyright licences and licence numbers for the reproduction of the full manuscripts of the articles reprinted on pages 65 to 126 in this thesis.

Manuscripts

Viehl et al. [2016a]

The photolysis of FeOH and its effect on the bottomside of the mesospheric Fe layer

Viehl, T. P., *J. M. C. Plane, W. Feng, and J. Höffner*

Geophys. Res. Lett., *43*, 1373–1381, (2016)

doi:10.1002/2015GL067241

Viehl et al. [2015]

Summer time Fe depletion in the Antarctic mesopause region

Viehl, T. P., *J. Höffner, F.-J. Lübken, J. M. C. Plane, B. Kaifler, and R. J. Morris*

J. Atmos. Solar-Terr. Phys., 127, 97–102, (2015)

doi:10.1016/j.jastp.2015.04.013

Viehl et al. [2016b]

Corrigendum to: Summer time Fe depletion in the Antarctic mesopause region, by Viehl et al. [2015]
Viehl, T. P., *J. Höffner, F.-J. Lübken, J. M. C. Plane, B. Kaifler, and R. J. Morris*
J. Atmos. Solar-Terr. Phys., 142, 150–151, (2016)

doi:10.1016/j.jastp.2016.02.001

Lübken et al. [2011]

First measurements of thermal tides in the summer mesopause region at Antarctic latitudes
*Lübken, F.-J., J. Höffner, **T. P. Viehl**, B. Kaifler, and R. J. Morris*
Geophys. Res. Lett., *38*, L24806, (2011)

doi:10.1029/2011GL050045

Feng et al. [2015]

Diurnal variation of the potassium layer in the upper atmosphere

Feng, W., J. Höffner, D. R. Marsh, M. P. Chipperfield, E. C. M. Dawkins, ***T. P. Viehl****, and J. M. C. Plane*

Geophys. Res. Lett., *42*, 3619–3626, (2015)

doi:10.1002/2015GL063718

Kaifler et al. [2015]

Lidar observations of gravity wave activity in the middle atmosphere over Davis (69°S, 78°E), Antarctica
Kaifler, B., Lübken, F.-J., J. Höffner, R. J. Morris, and ***T. P. Viehl***
J. Geophys. Res.: Atmos., *120*, 4506–4521, (2015)

doi:10.1002/2014JD022879

Morris et al. [2012]

Experimental evidence of a stratospheric circulation influence on mesospheric temperatures and ice-particles during the 2010–2011 austral summer at 69°S

*R. J. Morris, J. Höffner, F.-J. Lübken, **T. P. Viehl**, B. Kaifler, and A. R. Klekociuk*

J. Atmos. Solar-Terr. Phys., 89, 54–61, (2012)

doi:10.1016/j.jastp.2012.08.007

Lübken et al. [2014]

Winter/summer mesopause temperature transition at Davis (69°S) in 2011/2012
*Lübken, F.-J., J. Höffner, **T. P. Viehl**, B. Kaifler, and R. J. Morris*
Geophys. Res. Lett., 41, 5233–5238, (2014)

doi:10.1002/2014GL060777

Lübken et al. [2015]

Winter/summer transition in the Antarctic mesopause region

Lübken, F.-J., J. Höffner, ***T. P. Viehl****, E. Becker, R. Latteck, B. Kaifler, D. J. Murphy, and R. J. Morris*

J. Geophys. Res.: Atmos., *120*, 12,394–12,409, (2015)

doi:10.1002/2015JD023928

Contribution to the Manuscripts

In accordance with section 4 of the *Guidelines for making a cumulative dissertation at the Faculty of Mathematics and Natural Sciences, University of Rostock* in the version of 3 July 2012, the candidate's individual contributions to the manuscripts submitted in this thesis are detailed in the following.

Viehl et al. [2016a]

The photolysis of FeOH and its effect on the bottomside of the mesospheric Fe layer

***Viehl, T. P.**, J. M. C. Plane, W. Feng, and J. Höffner* *Geophys. Res. Lett.*, *43*, 1373–1381, (2016)

The candidate set up the lidar experiments in Antarctica and the Arctic, performed most of the measurements in Antarctica, maintained the instrument, analysed the lidar data, contributed to analysing the model data, had a major share in discussing the results and drawing conclusions, created Figures 1, 2, and 4, wrote all of the manuscript with exception of Section 3, assisted with writing Section 3, submitted the manuscript, and addressed all reviewer comments.

Viehl et al. [2015]

Summer time Fe depletion in the Antarctic mesopause region

***Viehl, T. P.**, J. Höffner, F.-J. Lübken, J. M. C. Plane, B. Kaifler, and R. J. Morris* *J. Atmos. Solar-Terr. Phys.*, 127, 97–102, (2015)

The candidate set up the lidar experiment in Antarctica, performed most of the measurements, maintained the instrument, analysed the lidar data, had a major share in discussing the results and drawing conclusions, created all figures, wrote all of the manuscript with exception of the second half of Section 3.3, assisted with writing the second half of Section 3.3, submitted the manuscript, and addressed all reviewer comments.

Viehl et al. [2016b]

Corrigendum to: Summer time Fe depletion in the Antarctic mesopause region, by Viehl et al. [2015]

***Viehl, T. P.**, J. Höffner, F.-J. Lübken, J. M. C. Plane, B. Kaifler, and R. J. Morris* *J. Atmos. Solar-Terr. Phys.*, 142, (2016)

The candidate had a large share in discussing the results and drawing conclusions, jointly authored the text of the manuscript with *J. M. C. Plane* and *J. Höffner*, and submitted the manuscript.

Lübken et al. [2011]

First measurements of thermal tides in the summer mesopause region at Antarctic latitudes

*Lübken, F.-J., J. Höffner, **T. P. Viehl**, B. Kaifler, and R. J. Morris* *Geophys. Res. Lett.*, *38*, L24806, (2011)

The candidate set up the lidar experiment in Antarctica, performed most of the measurements, maintained the instrument, had a minor share in discussing the results and drawing conclusions, and assisted with the data analysis. No contribution to the text of the manuscript.

Feng et al. [2015]

Diurnal variation of the potassium layer in the upper atmosphere

*Feng, W., J. Höffner, D. R. Marsh, M. P. Chipperfield, E. C. M. Dawkins, **T. P. Viehl**, and J. M. C. Plane* *GRL*, *42*, (2015)

The candidate assisted with the analysis of lidar and model data shown in Figures 2 and 3 a, b, and had a minor share in discussing the results. Minor comments on the text of the manuscript.

Kaifler et al. [2015]

Lidar observations of gravity wave activity in the middle atmosphere over Davis (69°S, 78°E), Antarctica
*Kaifler, B., Lübken, F.-J., J. Höffner, R. J. Morris, and **T. P. Viehl** J. Geophys. Res.: Atmos.*, *120*, 4506–4521, (2015)

The candidate set up the lidar experiment in Antarctica, maintained the instrument, and performed most of the lidar measurements excluding the winter months 05/2011 to 10/2011. No contribution to the data analysis, discussion of the results, or the text of the manuscript.

Morris et al. [2012]

Experimental evidence of a stratospheric circulation influence on mesospheric temperatures and ice-particles during the 2010–2011 austral summer at 69°
*R. J. Morris, J. Höffner, F.-J. Lübken, **T. P. Viehl**, B. Kaifler, and A. R. Klekociuk J. Atmos. Solar-Terr. Phys.*, 89, 54–61, (2012)

The candidate set up the lidar experiment in Antarctica, performed most of the lidar measurements, assisted with the analysis of lidar data, had a medium share in discussing the results, and assisted with the creation of Figure 3. No contribution to the text of the manuscript.

Lübken et al. [2014]

Winter/summer mesopause temperature transition at Davis (69°S) in 2011/2012
*Lübken, F.-J., J. Höffner, **T. P. Viehl**, B. Kaifler, and R. J. Morris Geophys. Res. Lett.*, *41*, 5233–5238, (2014)

The candidate set up the lidar experiment in Antarctica, performed most of the lidar measurements, assisted with the analysis of lidar data, and had a minor share in discussing the results. Minor comments on the text of the manuscript.

Lübken et al. [2015]

Winter/summer transition in the Antarctic mesopause region
*Lübken, F.-J., J. Höffner, **T. P. Viehl**, E. Becker, R. Latteck, B. Kaifler, D. J. Murphy, and R. J. Morris J. Geophys. Res.: Atmos.*, *120*, 12,394–12,409, (2015)

The candidate set up the lidar experiment in Antarctica, performed nearly all of the lidar measurements presented, assisted with the analysis of the lidar data, and performed a literature review. Some comments on the text of the manuscript. Medium contribution addressing reviewer comments.

Timo P. Viehl
October 2016

Prof. Dr. Franz-Josef Lübken
October 2016

Declaration

I declare that this thesis has been composed by myself and without outside help. I confirm that the work submitted is my own, except where work which has formed part of jointly-authored publications has been included. My contributions to the publications have been explicitly indicated on pages 141 and 142. I confirm that appropriate credit has been given within this thesis where reference has been made to the work of others. I declare that neither the opportunity for this doctoral research nor the completion of any tasks leading to the submission of this thesis have been arranged commercially.

I acknowledge that copyright of published works contained within this thesis resides with the copyright holder(s) of those works. The copyrighted material is reproduced in accordance with the licences on pages 61 and 62. As far as it does not infringe the rights of the original copyright holders, I give permission for the digital version of my thesis to be made available for fair use in scientific and educational context via the repositories, archives, and websites of the University Library of Rostock at the University of Rostock, Germany, the Leibniz-Institute of Atmospheric Physics at the University of Rostock in Kühlungsborn, Germany, and the German National Library in Frankfurt am Main and Leipzig, Germany and associated organisations. Please refer to the original copyright holders via the provided DOIs for personal copies of the full manuscripts submitted with this thesis.

Timo P. Viehl
October 2016

References

Achatz, U. N. Grieger, and H. Schmidt (2008), Mechanisms controlling the diurnal solar tide: Analysis using a GCM and a linear model, *J. Geophys. Res.*, *113*, A08303, doi:10.1029/2007JA012967.

Akmaev, R. A. (2011), Whole atmosphere modeling: connecting terrestrial and space weather, *Rev. Geophys.*, *49*, RG4004, doi:10.1029/2011RG000364.

Allen, S. J., and R. A. Vincent (1995), Gravity wave activity in the lower atmosphere: Seasonal and latitudinal variations, *J. Geophys. Res.*, *100*(D1), 1327–1350, doi:10.1029/94JD02688.

Alexander, M. J., and C. Barnet (2007), Using Satellite Observations to Constrain Parameterizations of Gravity Wave Effects for Global Models, *J. Atmos. Sci.*, *64*, 1652–1665, doi:10.1175/JAS3897.1.

Alexander, S. P., A. R. Klekociuk, and D. J. Murphy (2011), Rayleigh lidar observations of gravity wave activity in the winter upper stratosphere and lower mesosphere above Davis, Antarctica (69°S, 78°E), *J. Geophys. Res.*, *116*, D13109, doi:10.1029/2011JD015164.

Alexander, S. P., D. J. Murphy, and A. R. Klekociuk (2013), High resolution VHF radar measurements of tropopause structure and variability at Davis, Antarctica (69°S, 78°E), *Atmos. Chem. Phys.*, *13*, 3121–3132, doi:10.5194/acp-13-3121-2013.

Alpers, M. (1993b), Untersuchung der mesosphärischen Eisenschicht in polaren und niedrigen geographischen Breiten mittels Lidar, *Dissertation*, University of Bonn, Germany.

Alpers, M., J. Höffner, and U. von Zahn (1990), Iron atom densitites in the polar mesosphere from lidar observations, *Geophys. Res. Lett.*, *17*(12), 2345–2348.

Alpers, M., T. Blix, S. Kirkwood, D. Krankowsky, F.-J. Lübken, S. Lutz, and U. von Zahn (1993a), First Simultaneous Measurements of Neutral and Ionized Iron Densities in the Upper Mesosphere, *J. Geophys. Res.*, *98*(A1), 275–283.

Anders, E., and M. Ebihara (1982), Solar-system abundances of the elements, *Geoch. Cosmoch. Acta*, *46*, 2363–2380.

Baggaley, W. J. (2002), Radar Observations, in *Meteors in the Earth's Atmosphere*, ed. E. Murad and I. P. Williams, Camebridge University Press, 123–148, ISBN 978-0-521-80431-8.

Bailey, S. M., A. W. Merkel, G. E. Thomas, and J. N. Carstens (2005), Observations of polar mesospheric clouds by the Student Nitric Oxide Explorer, *J. Geophys. Res.*, *110*, D13203, doi:10.1029/2004JD005422.

Bailey, S. M., A. W. Merkel, G. E. Thomas, and D. W. Rusch (2007), Hemispheric differences in Polar Mesospheric Cloud morphology observed by the Student Nitric Oxide Explorer, *J. Atmos. Solar-Terr. Phys.*, *69*, 1407–1418, doi:10.1016/j.jastp.2007.02.008.

Baumgarten, G., J. Fiedler, and M. Rapp (2010), On microphysical processes of noctilucent clouds (NLC): observations and modeling of mean and width of the particle size-distribution, *Atmos. Chem. Phys.*, *10*, 6661–6668, doi:10.5194/acp-10-6661-2010.

Baumgarten, G., A. Chandran, J. Fiedler, P. Hoffmann, N. Kaifler, J. Lumpe, A. Merkel, C. E. Randall, D. Rusch, and G. Thomas (2012), On the horizontal and temporal structure of noctilucent clouds as observed by satellite and lidar at ALOMAR (69N), *Geophys. Res. Lett.*, *39*, L01803, doi:10.1029/2011GL049935.

Baumgarten, G., and D. C. Fritts (2014), Quantifying Kelvin-Helmholtz instability dynamics observed in noctilucent clouds: 1. Methods and observations, *J. Geophys. Res. Atmos.*, *119*, 9324–9337, doi:10.1002/2014JD021832.

Baumgarten, G., J. Fiedler, J. Hildebrand, and F.-J. Lübken (2015), Inertia gravity wave in the stratosphere and mesosphere observed by Doppler wind and temperature lidar, *Geophys. Res. Lett.*, *42*, 10,929–10,936, doi:10.1002/2015GL066991.

Bautista, M. A., P. Romano, and A. K. Pradhan (1998), Resonance-averaged photoinization cross sections for astrophysical models, *Astrophys. J. Suppl. Ser.*, *118*, 259–265, doi:10.1086/313132.

Becker, E. (2012), Dynamical Control of the Middle Atmosphere, *Space Sci. Rev.*, *168*(1), 283–314, doi:10.1007/s11214-011-9841-5.

Becker, E., R. Knöpfel, and F.-J. Lübken (2015), Dynamically induced hemispheric differences in the seasonal cycle of the summer polar mesopause, *J. Atmos. Solar-Terr. Phys.*, *129*, 128–141, doi:10.1016/j.jastp.2015.04.014.

Beig, G., P. Keckhut, R. P. Lowe, R. G. Roble, M. G. Mlynczak, J. Scheer, V. I. Formichev, D. Offermann, W. J. R. French, M. G. Shepherd, A. I. Semenov, E. E. Remsberg, C. Y. She, F. J. Lübken, J. Bremer, B. R. Clemesha, J. Stegman, F. Sigernes, and S. Fadnavis (2003), Review of mesospheric temperature trends, *Rev. Geophys.*, *41*, doi:10.1029/2002RG000121.

Benze, S., C. E. Randall, B. Karlsson, V. L. Harvey, M. T. DeLand, G. E. Thomas, and E. P. Shettle (2012), On the onset of polar mesospheric cloud seasons as observed by SBUV, *J. Geophys. Res.*, *117*, D07104, doi:10.1029/2011JD017350.

Berger, U., and F.-J. Lübken (2015), Trends in mesospheric ice layers in the Northern Hemisphere during 1961–2013, *J. Geophys. Res. Atmos.*, *120*, 11,277–11,298, doi:10.1002/2015JD023355.

Bones, D. L., J. M. C. Plane, and W. Feng (2015), Dissociative Recombination of FeO^+ with Electrons: Implications for Plasma Layers in the Ionosphere, *J. Phys. Chem. A*, doi:10.1021/acs/jpca.5b04947.

Bowman, M. R., A. J. Gibson, and M. C. W. Sandford (1969), Atmospheric Sodium measured by a Tuned Laser Radar, *Nature*, *221*, 456–457, doi:10.1038/221456a0.

Brekke, A. (2013), *Physics of the Upper Polar Atmosphere*, 2nd ed., Spinger-Praxis Books in Environmental Sciences, Springer-Verlag Berlin Heidelberg, ISBN 978-3-642-27400-8, doi:10.1007/978-3-642-27401-5.

Butchart, N. (2014), The Brewer-Dobson circulation, *Rev. Geophys.*, *52*, 157–184, doi:10.1002/2013RG000448.

Ceplecha, Z., J. Borovička, W. G. Elford, D. O. Revelle, R. L. Hawkes, V. Porubčan, and M. Šimek (1998) Meteor phenomena and bodies, *Space Science Reviews*, *84*, 327–471.

Charney, J. G., and P. G. Drazin (1961), Propagation of planetary-scale disturbances from the lower into the upper atmosphere, *J. Geophys. Res.*, *66*(1), 83–109, doi:10.1029/JZ066i001p00083.

Chu, X., C. Yamashita, P. J. Espy, G. J. Nott, E. J. Jensen, H.-L. Liu, W. Huang, and J. P. Thayer (2009), Responses of polar mesospheric cloud brightness to stratospheric gravity waves at the South Pole and Rothera, Antarctica, *J. Atmos. Solar-Terr. Phys.*, *71*, 434–445, doi:10.1016/j.jastp.2008.10.002.

Chu, X, W. Huang, W. Fong, Z. Yu, Z. Wang, J. A. Smith, and C. S. Gardner (2011a), First lidar observations of polar mesospheric clouds and Fe temperatures at McMurdo (77.8°S, 166.7°E), Antarctica, *Geophys. Res. Lett.*, *38*, L16810, doi:10.1029/2011GL048373.

Chu, X, Z. Yu, C. S. Gardner, C. Chen, and W. Fong (2011b), Lidar observations of neutral Fe layers and fast gravity waves in the thermosphere (110–155 km) at McMurdo (77.8°S, 166.7°E), Antarctica, *Geophys. Res. Lett.*, *38*, L23807, doi:10.1029/2011GL050016.

Clemesha, B. R., D. M. Simonich, P. P. Batista, and V. W. J. H. Kirchhoff (1982), The diurnal variation of atmospheric sodium, *J. Geophys. Res.*, *87*(A1), 181–186, doi:10.1029/JA087iA01p00181.

Collins, R. L., J. Li, and C. M. Martus (2015), First lidar observation of the mesospheric nickel layer, *Geophys. Res. Lett.*, *42*, 665–671, doi:10.1002/2014GL062716.

Dawkins, E. C. M., J. M. C. Plane, M. P. Chipperfield, W. Feng, J. Gumbel, J. Hedin, J. Höffner, and J. S. Friedman, First global observations of the mesospheric potassium layer, *Geophys. Res. Lett.*, *41*, 5653–5661, doi:10.1002/2014GL060801.

Dawkins, E. C. M., J. M. C. Plane, M. P. Chipperfield, W. Feng, D. R. Marsh, J. Höffner, and D. Janches, Solar cycle response and long-term trends in the mesospheric metal layers, *J. Geophys. Res. Space Physics*, *Accepted for publication*, doi:10.1002/2016JA022522.

DeLand, M. T., E. P. Shettle, G. E. Thomas, and J. J. Olivero (2003), Solar backscattered ultraviolet (SBUV) observations of polar mesospheric clouds (PMCs) over two solar cycles, *J. Geophys. Res.*, *108*(D8), 8445, doi:10.1029/2002JD002398.

DeLand, M. T., E. P. Shettle, G. E. Thomas, and J. J. Olivero (2006), A quarter-century of satellite polar mesospheric cloud observations, *J. Atmos. Solar-Terr. Phys.*, *68*, 9–29, doi:10.1016/j.jastp.2005.08.003.

DeLand, M. T., E. P. Shettle, G. E. Thomas, and J. J. Olivero (2007), Latitude-dependent long-term variations in polar mesospheric clouds from SBUV version 3 PMC data, *J. Geophys. Res.*, *112*, D10315, doi:10.1029/2006JD007857.

DeLand, M. T., and G. E. Thomas (2015), Updated PMC trends derived from SBUV data, *J. Geophys. Res. Atmos.*, *120*, 2140–2166, doi:10.1002/2014JD022253.

Delaval, J. M., C. Dufour, and J. Schamps (1980), Rotational analysis of ultraviolet systems of FeCl, *J. Phys. B: Atom. Molec. Phys.*, *13*, 4757–4769, doi:10.1088/022-3700/13/24/010.

Delgado, R., J. S. Friedman, J. T. Fentzke, S. Raizada, C. A. Tepley, and Q. Zhou (2012), Sporadic metal atom and ion layers and their connection to chemistry and thermal structure in the mesopause region at Arecibo, *J. Atmos. Solar-Terr. Phys.*, *74*, 11–23, doi:10.1016/j.jastp.2011.09.004.

Dhadly, M. S., J. Meriwether, M. Conde, and D. Hampton (2015), First ever cross comparison of thermospheric wind measured by narrow- and wide-field optical Doppler spectroscopy, *J. Geophys. Res. Space Physics*, *120*, 9683–9705, doi:10.1002/2015JA021316.

Dhomse, S. S., R. W. Saunders, W. Tian, M. P. Chipperfield, and J. M. C. Plane (2013), Plutonium-238 observations as a test of modeled transport and surface deposition of meteoric smoke particles, *Geophys. Res. Lett.*, *40*, 4454–4458, doi:10.1002/grl.50840.

Drever, R. W. P., J. L. Hall, F. V. Kowalski, J. Hough, G. M. Ford, A. J. Munley, and H. Ward (1983), Laser Phase and Frequency Stabilization Using an Optical Resonator, *Appl. Phys. B*, *31*, 97–105.

Dunker, T., U.-P. Hoppe, W. Feng, J. M. C. Plane, and D. R. Marsh (2015), Mesospheric temperatures and sodium properties measured with the ALOMAR Na lidar compared with WACCM, *J. Atmos. Solar-Terr. Phys.*, *127*, 111–119, doi:10.1016/j.jastp.2015.01.003.

Eixmann, R., M. Gerding, J. Höffner, and M. Kopp (2015), Lidars with narrow FOV for spectral and daylight measurements, *Trans. Geo. Remote Sens.*, *53*(8), 4548–4553, doi:10.1109/TGRS.2015.2401333.

England, S. L., S. Maus, T. J. Immel, and S. B. Mende (2006), Longitudinal variation of the E-region electric fields caused by atmospheric tides, *Geophys. Res. Lett.*, *33*, L21105, doi:10.1029/2006GL027465.

Eska, V., and J. Höffner (1998), Observed linear and nonlinear K layer response, *Geophys. Res. Lett.*, *25*(15), 2933-2936.

Feng, W., D. R. Marsh, M. P. Chipperfield, D. Janches, J. Höffner, F. Yi, and J. M. C. Plane (2013), A global atmospheric model of meteoric iron, *J. Geophys. Res.*, *118*, doi:10.1002/jgrd.50708.

Feng, W., J. Höffner, D. R. Marsh, M. P. Chipperfield, E. C. M. Dawkins, T. P. Viehl, and J. M. C. Plane (2015), Diurnal variation of the potassium layer in the upper atmosphere, *Geophys. Res. Lett.*, *42*, 3619–3626, doi:10.1002/2015GL063718.

Fentzke, J. T., and C. Janches (2008), A semi-empirical model of the contribution from sporadic meteoroid sources on the meteor input function in the MLT observed at Arecibo, *J. Geophys. Res.*, *113*, A03304, doi:10.1029/2007JA012531.

Feofilov, A. G., and A. A. Kutepov (2012), Infrared Radiation in the Mesosphere and Lower Thermosphere: Energetic Effects and Remote Sensing, *Surv. Geophys.*, *33*, 1231–1280, doi:10.1007/s10712-012-9204-0.

Fiedler, J., G. Baumgarten, U. Berger, A. Gabriel, R. Latteck, F.-J. Lübken (2015), On the early onset of the NLC season 2013 as observed at ALOMAR, *J. Atmos. Solar-Terr. Phys.*, *127*, 73–77, doi:10.1016/j.jastp.2014.07.011.

Fleming, E. L., S. Chandra, J. J. Barnett, and M. Corney (1990), Zonal mean temperature, pressure, zonal wind and geopotential height as functions of latitude, COSPAR International Reference Atmospheres: 1986, Part II: Middle Atmosphere Models, *Adv. Space. Res.*, *10*(12), 11–59, doi:10.1016/0273-1177(90)90230-W.

Flynn, G. J. (2002), Extraterrestrial Dust in the Near-Earth Environment, in *Meteors in the Earth's Atmosphere*, ed. E. Murad and I. P. Williams, Cambridge University Press, 77–94, ISBN 978-0-521-80431-8.

Forbes, J. M., and H. B. Garrett (1979), Theoretical studies of atmospheric tides, *Reviews of Geophysics and Space Physics*, *17*(8), 1951–1981, doi:10.1029/RG017i008p01951.

Forbes, J. M., and D. Wu (2006), Solar Tides as Revealed by Measurements of Mesosphere Temperature by the MLS Experiment on UARS, *J. Atmos. Sci.*, *63*, 1776–1797, doi:10.1175/JAS3724.1.

Frankland, V. L., A. D. James, W. Feng, and J. M. C. Plane (2015), The uptake of HNO_3 on meteoric smoke analogues, *J. Atmos. Solar-Terr. Phys.*, *127*, 150–160, doi:10.1016/j.jastp.2015.01.010.

French, W. J. R., and F. J. Mulligan (2010), Stability of temperatures from TIMED/SABER v1.07 (2002–2009) and Aura/MLS v2.2 (2004–2009) compared with OH(6-2) temperatures observed at Davis Station, Antarctica, *Atmos. Chem. Phys.*, *10*, 11439–11446, doi:10.5194/acp-10-11439-2010.

French, W. J. R., and A. R. Klekociuk (2011), Long-term trends in Antarctic winter hydroxyl temperatures, *J. Geophys. Res*, *116*, D00P09, doi:10.1029/2011JD015731.

Fricke, K. H., and U. von Zahn (1985), Mesopause temperatures derived from probing the hyperfine structure of the D_2 resonance line of sodium by lidar, *J. Atmos. Terr. Phys.*, *47*(5), 499–512.

Fricke-Begemann, C., J. Höffner, and U. von Zahn (2002), The potassium density and temperature structure in the mesopause region (80–105 km) at low latitude (28°N), *Geophys. Res. Lett.*, *29*(22), 2067, doi:10.1029/2002GL015578.

Fricke-Begemann, C., and J. Höffner (2005), Temperature tides and waves near the mesopause from lidar observations at two latitudes, *J. Geophys. Res.*, *110*, D19103, doi:10.1029/2005JD005770.

Frisch, M. J., et al. (2009), Gaussian 09, *Revision A.1*, Gaussian Inc., Wallingford CT.

Fritts, D. C., and R. A. Vincent (1987), Mesospheric Momentum Flux Studies at Adelaide, Australia: Observations and a Gravity Wave-Tidal Interaction Model, *J. Atmos. Sci.*, *44*(3), 605–619.

Fritts, D. C., and J. M. Alexander (2003), Gravity wave dynamics and effects in the middle atmosphere, *Rev. Geophys.*, *41*(1), doi:10.1029/2001RG000106.

Fussen, D., F. Vanhellemont, C. Bingen, E. Kryölä, J. Tamminen, V. Sofieva, S. Hassinen, A. Seppälä, P. Verronen, J.-L. Bertraux, A. Hauchecorne, F. Dalaudier, J.-B. Renard, R. Fraisse, O. Fanton d'Andon, G. Barrot, A. Mangin, B. Théodore, M. Guirlet, R. Koopman, P. Snoeij, and L. Saavedra (2004), Global measurements of the mesospheric sodium layer by the star occultation instrument GOMOS, *Geophys. Res. Lett.*, *31*, L24110, doi:10.1029/2004GL021618.

Fussen, D., F. Vanhellemont, C. Tétard, N. Matheshvili, E. Dekemper, N. Loodts, C. Bingen, E. Kryölä, J. Tamminen, V. Sofieva, A. Hauchecorne, F. Dalaudier, J.-L. Bertraux, G. Barrot, L. Blanot, O. Fanton d'Andon, T. Fehr, L. Saavedra, T. Yuan, and C.-Y. She (2010), A global climatology of the meospheric sodium layer from GOMOS data during the 2002–2008 period, *Atmos. Chem. Phys.*, *10*, 9225–9236, doi:10.5194/acp-10-9225-2010.

Garcia, R. R., and S. Solomon (1985), The Effect of Breaking Gravity Waves on the Dynamics and Chemical Composition of the Mesosphere and Lower Thermosphere, *J. Geophys. Res.*, *90*(D2), 3850–3868.

Garcia, R. R., F. Stordal, S. Solomon, and J. T. Kiehl (1992), A new numerical model of the middle atmosphere, 1, Dynamics and transport of tropospheric source gases, *J. Geophys. Res.*, *97*, 12,967–12,991, doi:10.1029/92JD00960.

García-Comas, M., M. López-Puertas, M. T. Marshall, P. P. Wintersteiner, B. Funke, D. Bermejo-Pantaleón, C. J. Mertens, E. E. Remsberg, L. L. Gordley, M. G. Mlynczak, and J. M. Russell III (2008), Errors in Sounding of the Atmosphere using Broadband Emission Radiometry (SABER) kinetic temperature caused by non-local-thermodynamic-equilibrium model parameters, *J. Geophys. Res*, *113*, D24106, doi:10.1029/2008JD010105.

Gardner, C. S. (2004), Performance capabilities of middle-atmosphere temperature lidars: comparison of Na, Fe, K, Ca, Ca^+, and Rayleigh systems, *Applied Optics*, *43*(25), 4941–4956, doi:10.1364/AO.43.004941.

Gardner, C. S., J. M. C. Plane, W. Pan, T. Vondrak, B. J. Murray, and X. Chu (2005), Seasonal variations of the Na and Fe layers at the South Pole and their implications for the chemistry and general circulation of the polar mesosphere, *J. Geophys. Res.*, *110*, D10302, doi:10.1029/2004JD005670.

Gardner, C. S., X. Chu, P. J. Espy, and J. M. C. Plane, D. R. Marsh, and D. Janches (2011), Seasonal variations of the mesospheric Fe layer at Rothera, Antarctica (67.5°S, 68.0°W), *J. Geophys. Res.*, *116*, D02304, doi:10.1029/2010JD014655.

Gardner, C. S., A. Z. Liu, D. R. Marsh, W. Feng, and J. M. C. Plane (2014), Inferring the global cosmic dust influx to the Earth's atmosphere from lidar observations of the vertical flux of mesospheric Na, *J. Geophys. Res.*, *119*, 7870–7879, doi:10.1002/2014JA020383.

Geller, M. A. (1983), Dynamics of the middle atmosphere, *Space Sci. Rev.*, *34*, 359–375, doi:10.1007/BF00168828.

Gerding, M., J. Höffner, J. Lautenbach, M. Rauthe, and F.-J. Lübken (2008), Seasonal variation of nocturnal temperatures between 1 and 105 km altitude at 54°N observed by lidar, *Atmos. Chem. Phys.*, *8*, 7465–7482, doi:10.5194/acp-8-7465-2008.

Gibson, A. J., L. Thomas, and S. K. Bhattachacharyya (1979), Laser observations of the ground-state hyperfine structure of sodium and of temperatures in the upper atmosphere, *Nature*, *281*, 131–132, doi:10.1038/281131a0.

Goméz-Martín, J. C., S. A. Garraway, and J. M. C. Plane (2015), Reaction Kinetics of Meteoric Sodium Reservoirs in the Upper Atmosphere, *J. Phys. Chem. A*, doi:10.1021/acs.jpca.5b00622.

Gordley, L. L., M. E. Hervig, C. Fish, J. M. Russell III, S. Bailey, J. Cook, S. Hansen, A. Shumway, G. Paxton, L. Deaver, T. Marshall, J. Burton, B. Magill, C. Brown, E. Thompson, and J. Kemp (2009), The solar occultation for ice experiment, *J. Atmos. Solar-Terr. Phys.*, *71*, 300–315, doi:10.1016/j.jastp.2008.07.012.

Grygalashvyly, M., G. R. Sonnemann, F.-J. Lübken, P. Hartogh, and U. Berger (2014), Hydroxyl layer: Mean state and trends at midlatitudes, *J. Geophys. Res. Atmos.*, *119*, 12,391–12,419, doi:10.1002/2014JD022094.

Gumbel, J., and L. Megner (2009), Charged meteoric smoke as ice nuclei in the mesosphere: Part 1—A review of basic concepts, *J. Atmos. Solar-Terr. Phys.*, *71*, 1225–1235, doi:10.1016/j.jastp.2009.04.012.

Gumbel, J., and B. Karlsson (2011), Intra- and interhemispheric coupling effects on polar summer mesosphere, *Geophys. Res. Lett.*, *38*, L14804, doi:10.1029/2011GL047968.

Gurubaran, S., R. Rajaram, T. Nakamura, and T. Tsuda (2005), Interannual variability of diurnal tide in the tropical mesopause region: A signature of the El Nino-Southern Oscillation (ENSO), *Geophys. Res. Lett.*, *32*, L13805, doi:10.1029/2005GL022928.

Hagan, M. E., and J. M. Forbes (2002), Migrating and nonmigrating diurnal tides in the middle and upper atmosphere excited by tropospheric latent heat release, *J. Geophys. Res.*, *107*(D24), 4754, doi:10.1029/2001JD001236.

Hagan, M. E., and J. M. Forbes (2003), Migrating and nonmigrating semidiurnal tides in the upper atmosphere excited by tropospheric latent heat release, *J. Geophys. Res.*, *108*, 1062, doi:10.1029/2002JA009466.

Haldoupis, C., D. Pancheva, and N. J. Mitchell (2004), A study of tidal and planetary wave periodicities present in midlatitude sporadic *E* layers, *J. Geophys. Res.*, *109*, A02302, doi:10.1029/2003JA010253.

Hansen, G., M. Serwazi, and U. von Zahn (1989), First detection of a noctilucent cloud by lidar, *Geophys. Res. Lett.*, *16*(12), 1445–1448, doi:10.1029/GL016i012p01445.

Haynes, P. H., C. J. Marks, M. E. McIntyre, T. G. Shepherd, and K. P. Shine (1991), On the "Downward Control" of Extratropical Diabatic Circulations by Eddy-Induced Mean Zonal Forces, *J. Amtos. Sci.*, *48*(4), 651–678, doi:10.1175/1520-0469.

Helmer, M., J. M. C. Plane, J. Qian, and C. S. Gardner (1998), A model of meteoric iron in the upper atmosphere, *J. Geophys. Res.*, *103*(D9), 10,913–10,925, doi:10.1029/97JD03075.

Hervig, M., R. E. Thompson, M. McHugh, L. L. Gordley, J. M. Russell III, and M. E. Summers (2001), First confirmation that water ice is the primary component of polar mesospheric

clouds, *Geophys. Res. Lett.*, *28*(6), 971–974, doi:10.1029/2000GL012104.

Hervig, M. E., L. L. Gordley, J. M. Russell III, and S. M. Bailey (2009), SOFIE PMC observations during the northern summer of 2007, *J. Atmos. Solar-Terr. Phys.*, *71*, 331–339, doi:10.1016/j.jastp.2008.08.010.

Hervig, M. E., and L. L. Gordley (2010), Temperature, shape, and phase of mesospheric ice from Solar Occultation for Ice Experiment observations, *J. Geophys. Res.*, *115*, D15208, doi:10.1029/2010JD013918.

Hervig, M. E., and M. H. Stevens (2014), Interpreting the 35 year SBUV PMC record with SOFIE observations, *J. Geophys. Res. Atmos.*, *119*, 12,689–12,705, doi:10.1002/2014JD021923.

Hervig, M. E., U. Berger, and D. E. Siskind (2016), Decadal variability in PMCs and implications for changing temperature and water vapor in the upper mesosphere, *J. Geophys. Res. Atmos.*, *121*, 2383–2392, doi:10.1002/20015JD024439.

Hildebrand, J., G. Baumgarten, J. Fiedler, U.-P. Hoppe, B. Kaifler, F.-J. Lübken, and B. P. Williams (2012), Combined wind measurements by two different lidar instruments in the Arctic middle atmosphere, *Atmos. Meas. Tech.*, *5*, 2433–2445, doi:10.5194/amt-5-2433-2012.

Hoffmann, P., E. Becker, W. Singer, and M. Placke (2010), Seasonal variation of mesospheric waves at northern middle and high latitudes, *J. Atmos. Solar-Terr. Phys.*, *72*, 1068–1079, doi:10.1016/j.jastp.2010.07.002.

Höffner, J. (1994), Metallschichten in der Mesosphäre: Beobachtungen und Modellierung, *Dissertation*, University of Bonn, Germany.

Höffner, J. (2015), Method and device for determining and calculating a scattered radiation spectrum and method for compressing data, *Patent*, DE 102 012 221 862.9 (DE 10 2012 221 862 A1), PCT/EP2013/074781 (WO 2014/083014 A2), EP 13805791.4 (EP 2 926 163 A0), US 14/648,010 (US 2015/0323386 A1).

Höffner, J., U. von Zahn, W. J. McNeil, and E. Murad (1999), The 1996 Leonid shower as studied with a potassium lidar: Observations and inferred meteoroid sizes, *J. Geophys. Res.*, *104*(A2), 2633–2643, doi:10.1029/1998JA900063.

Höffner, J., and J. S. Friedman (2004), The mesospheric metal layer topside: a possible connection to meteoroids, *Atmos. Chem. Phys.*, *4*, 801–808, doi:10.5194/acp-4-801-2004.

Höffner, J., and J. S. Friedman (2005), The mesospheric metal layer topside: Examples of simultaneous metal observations, *J. Atmos. Solar-Terr. Phys.*, *67*, 1226–1237, doi:10.1016/j.jastp.2005.06.010.

Höffner, J., and C. Fricke-Begemann (2005), Accurate lidar temperatures with narrowband filters, *Opt. Lett.*, *30*(8), 890–892.

Höffner, J., J. Lautenbach, C. Fricke-Begemann, and F.-J. Lübken (2006), Polar mesosphere temperature observations by lidar and falling sphere at 78°N, *Reviewed and Revised Papers Presented at the 23rd International Laser Radar Conference 24–28 July 2006, Nara, Japan*, *ISBN 4-9902916-0-3*.

Höffner, J., and F.-J. Lübken (2007), Potassium lidar temperatures and densities in the mesopause region at Spitsbergen (78°N), *J. Geohpys. Res.*, *112*, D20114, doi:10.1029/2007JD008612.

Höffner, J., and J. Lautenbach (2009), Daylight measurements of mesopause temperature and vertical wind with the mobile scanning iron Lidar, *Opt. Lett.*, *34*, 1351–1353.

Höffner, J., T. P. Viehl, and R. Eixmann (2016), Method and device for determining the wind speed, Verfahren und Vorrichtung zur Bestimmung der Windgeschwindigkeit, *Patent pending EU/US/GER*, DE 102 015 122 201.9, *unpublished July 2016*.

Holton, J. R. (1982), The Role of Gravity Wave Induced Drag and Diffusion in the Momentum Budget of the Mesosphere, *J. Atmos. Science*, *39*, 791–799.

Holton, J. R. (1983), The Influence of Gravity Wave Breaking on the General Circulation of the Middle Atmosphere, *J. Atmos. Science*, *40*, 2497–2507, doi:10.1175/1520-0469(1983)040<2497:TIOGWB>2.0.CO;2.

Holton, J. R. (2004), *An Introduction to Dynamic Meteorology*, 4th ed., International Geophysics Series, Elsevier Academic Press, ISBN 978-0-12-354015-7.

Houghton, J. T. (2002), *The Physics of Atmospheres*, 3rd ed., Reprinted 2005, Camebridge University Press, ISBN 0-521-01122-1.

Huaman, M. M., and B. B. Balsley (1999), Differences in near-mesopause summer winds, temperatures, and water vapor at northern and southern latitudes as possible causal factors for interhemispheric PMSE differences, *Geophys. Res. Lett.*, *26*(11), 1529–1532, doi:10.1029/1999GL900294.

Huang, W., X. Chu, C. S. Gardner, J. D. Carrillo-Sanchez, W. Feng, J. M. C. Plane, and D. Nesvorny (2015), Measurements of the vertical fluxes of atomic Fe and Na at the mesopause: Implications for the velocity of cosmic dust entering the atmosphere, *Geophys. Res. Lett.*, *42*, 169–175, doi:10.1002/2014GL062390.

Hunten, D. M. (1954), A study of sodium in twilight. I. Theory, *J. Atmos. Terr. Phys.*, *5*, 44–56, doi:10.1016/0021-9169(54)90006-9.

Hunten, D. M., and W. L. Godson (1967), Upper-Atmospheric Sodium and Stratospheric Warmings at High Latitudes, *J. Atmos. Sci.*, *24*, 80–87.

Hunten, D. M., R. P. Turco, and O. B. Toon (1980), Smoke and Dust Particles of Meteoric Origin in the Mesosphere and Stratosphere, *J. Atmos. Sci.*, *37*, 1342–1357, doi:10.1175/1520-0469.

Jensen, D. E., and G. A. Jones (1974), Catalysis of radical recombination in flames by iron, *J. Chem. Phys.*, *60*, 3421–3425, doi:10.1063/1.1681554.

Jesse, O., (1896), Die Höhe der leuchtenden Nachtwolken, *Astron. Nachrichten*, *140*(3347), 161–168.

Johnson, K. S. (2001), Iron supply and demand in the upper ocean: Is extraterrestrial dust a significant source of bioavailable iron?, *Global Biogeochem. Cycles*, *15*(1), 61–63, doi:10.1029/2000GB001295.

Kaifler, B., (2014), Thermal Structure and Gravity Waves in the Antarctic Middle Atmosphere Observed by Lidar, *Dissertation*, University of Rostock, Germany.

Kaifler, B., F.-J. Lübken, J. Höffner, R. J. Morris, and T. P. Viehl (2015), Lidar observations of gravity wave activity in the middle atmosphere over Davis (69°S, 78°E), Antarctica, *J. Geophys. Res. Atmos.*, *120*, doi:10.1002/2014JD022879.

Kaifler, N., G. Baumgarten, J. Fiedler, and F.-J. Lübken (2013), Quantification of waves in lidar observations of noctilucent clouds at scales from seconds to minutes, *Atmos. Chem. Phys.*, *13*, 11757–11768, doi:10.5194/acp-13-11757-2013.

Kalashnikova, O., M. Horanyi, G. E. Thomas, and O. B. Toon (2000), Meteoric smoke production in the atmosphere, *Geophys. Res. Lett.*, *27*(20), 3293–3296, doi:10.1029/1999GL011338.

Karlsson, B., H. Körnich, and J. Gumbel (2007), Evidence for interhemispheric stratosphere-mesosphere coupling derived from noctilucent cloud properties, *Geophys. Res. Lett.*, *34*, L16806, doi:10.1029/2007GL030282.

Karlsson, B., C. E. Randall, T. G. Shepherd, V. L. Harvey, J. Lumpe, K. Nielsen, S. M. Bailey, M. Hervig, and J. M. Russell III (2011), On the seasonal onset of polar mesospheric clouds and the breakdown of the stratospheric polar vortex in the Southern Hemisphere, *J. Geophys. Res.*, *116*, D18107, doi:10.1029/2011JD015989.

Kiliani, J., G. Baumgarten, F.-J. Lübken, and U. Berger (2015), Impact of particle shape on the morphology of noctilucent clouds, *Atmos. Chem. Phys.*, *15*, 12897–12907, doi:10.5194/acp-15-12897-2015.

Kinnison, D. E., G. P. Brasseur, S. Walters, R. R. Garcia, D. R. Marsh, F. Sassi, V. L. Harvey, C. E. Randall, L. Emmons, J. F. Lamarque, P. Hess, J. J. Orlando, X. X Tie, W.Randel, L. L. Pan, A. Gettelman, C. Granier, T. Diehl, U. Niemeier, and A. J. Simmons (2007), Sensitivity of chemical tracers to meteorological parameters in the MOZART-3 chemical transport model, *J. Geophys. Res.*, *112*(D20), 2156–2202, doi:10.1029/2006JD007879.

Kirkwood, S., I. Wolf, H. Nilsson, P. Dalin, D. Mikhaylova, and E. Belova (2007), Polar mesosphere summer echoes at Wasa, Antarctica (73°S): First observations and comparison with 68°N, *Geophys. Res. Lett.*, *34*, L15803, doi:10.1029/2007GL030516.

Kirkwood, S., H. Nilsson, R. J. Morris, A. R. Klekociuk, D. A. Holdsworth, and N. J. Mitchell (2008), A new height for the summer mesopause: Antarctica, December 2007, *Geophys. Res. Lett.*, *35*, L23810, doi:10.1029/2008GL035915.

Klekociuk, A. R., R. J. Morris, and J. L. Innis (2008), First Southern Hemisphere common-volume

measurements of PMC and PMSE, *Geophys. Res. Lett.*, *35*, L24804, doi:10.1029/2008GL035988.

Körnich, H., and E. Becker (2010), A simple model for the interhemispheric coupling of the middle atmosphere circulation, *Adv. Space Res.*, *45*, 661–668, doi:10.1016/j.asr.2009.11.001.

Kopp, M., M. Gerding, J. Höffner, and F.-J. Lübken (2015), Tidal signatures in temperatures derived from daylight soundings above Kühlungsborn (54°N, 12°E), *J. Atmos. Solar-Terr. Phys.*, *127*, 37–50, doi:10.1016/j.jastp.2014.09.002.

Langhoff, S. R., H.-J. Werner, and P. Rosmus (1986), Theoretical Transition Probabilities for the OH Meinel System, *J. Mol. Spectrosc.*, *118*(2), 507–529, doi:10.1016/0022-2852(86)90186-4.

Langowski, M. P., C. von Savigny, J. P. Burrows, W. Feng, J. M. C. Plane, D. R. Marsh, D. Janches, M. Sinnhuber, A. C. Aikin, and P. Liebing (2015), Global investigation of the Mg atom and ion layers using SCIAMACHY/Envisat observations between 70 and 150 km altitude and WACCM-Mg model results, *Atmos. Chem. Phys.*, *15*, 273–295, doi:10.5194/acp-15-273-2015.

Latteck, R., W. Singer, R. J. Morris, D. A. Holdsworth, and D. J. Murphy (2007), Observation of polar mesosphere summer echoes with calibrated VHF radars at 69° in the Northern and Southern hemispheres, *Geophys. Res. Lett.*, *34*, L14805, doi:10.1029/2007GL030032.

Lautenbach, J., and J. Höffner (2004), Scanning iron temperature lidar for mesopause temperature observation, *Appl. Opt.*, *43*(23), 4559–4563, doi:10.1364/AO.43.004559.

Lautenbach, J., J. Höffner, P. Menzel, and P. Keller (2005), The new scanning iron lidar, current state and future developments, *Proceedings of the 17th ESA Symposium on European Rocket and Balloon Programmes and Related Research*, Sandefjord, Norway, (ESA SP-590, August 2005).

Lautenbach, J., J. Höffner, F.-J. Lübken, and M. Zecha (2008), The thermal structure at the topside and above of polar mesosphere summer echoes over Spitsbergen 78°N, *Ann. Geophy.*, *26*, 1083–1088, doi:10.5194/angeo-26-1083-2008.

Lei, J., and P. J. Dagdigian (2000), Molecular beam study of the $^6\Pi$–$X^6\Delta$ electronic transition in FeCl, *J. Chem. Phys.*, *112*, 10221–10227, doi:10.1063/1.481664.

Leslie, R. J. (1885), Sky glows, *Nature*, *33*, 245–246, doi:10.1038/032245a0.

Lindzen, R. S. (1981), Turbulence and Stress Owing to Gravity Wave and Tidal Breakdown, *J. Geophys. Res.*, *86*(C10), 9707–9714, doi:10.1029/JC086iC10p09707.

Lindzen, R. S., and S. Chapman (1969), Atmospheric Tides, *Space Science Reviews*, *10*, 3–188.

Lübken, F.-J. (1997), Seasonal variation of turbulent energy dissipation rates at high latitudes as determined by in situ measurements of neutral density fluctuations, *J. Geophys. Res.*, *102*(D12), 13,441–13,456, doi:10.1029/97JD00853.

Lübken, F.-J. (1999), Thermal structure of the Arctic summer mesosphere, *J. Geophys. Res.*, *104*(D8), 9135–9149, doi:10.1029/1999JD900076.

Lübken, F.-J. (2013), Turbulent scattering for radars: A summary, *J. Atmos. Solar-Terr. Phys.*, *107*, 1–7, doi:10.1016/j.jastp.2013.10.015.

Lübken, F.-J., and U. von Zahn (1991), Thermal Structure of the Mesopause Region at Polar Latitudes, *J. Geophys. Res.*, *96*(D11), 20,841–20,857, doi:10.1029/91JD02018.

Lübken, F.-J., and J. Höffner (2004), Experimental evidence for ice particle interaction with metal atoms at the high latitude summer mesopause region, *Geophys. Res. Lett.*, *31*, L08103, doi:10.1029/2004GL019586.

Lübken, F.-J., A. Müllemann, and M. J. Jarvis (2004), Temperatures and horizontal winds in the Antarctic summer mesosphere, *J. Geophys. Res.*, *109*, D24112, doi:10.1029/2004JD005133.

Lübken, F.-J., and U. Berger (2007), Interhemispheric comparsion of mesospheric ice layers from the LIMA model, *J. Atmos. Solar-Terr. Phys.*, *69*, 2292–2308, doi:10.1016/j.jastp.2007.07.006.

Lübken, F.-J., U. Berger, and G. Baumgarten (2009), Stratospheric and solar cycle effects on long-term variability of mesospheric ice clouds, *J. Geophys. Res.*, *114*, D00I06, doi:10.1029/2009JD012377.

Lübken, F.-J., and U. Berger (2011), Latitudinal and interhemispheric variation of stratospheric effects on mesospheric ice layer trends, *J. Geophys. Res.*, *116*, D00P03, doi:10.1029/2010JD015258.

Lübken, F.-J., J. Höffner, T. P. Viehl, B. Kaifler, and R. J. Morris (2011), First measurements of thermal tides in the summer mesopause region at Antarctic latitudes, *Geophys. Res. Lett.*, *38*, doi:10.1029/2011GL050045.

Lübken, F.-J., J. Höffner, T. P. Viehl, B. Kaifler, and R. J. Morris (2014), Winter/summer mesopause temperature transition at Davis (68°S) in 2011/2012, *Geophys. Res. Lett.*, *41*, 5233–5238, doi:10.1002/2014GL060777.

Lübken, F.-J., J. Höffner, T. P. Viehl, E. Becker, R. Latteck, B. Kaifler, D. J. Murphy, and R. J. Morris (2015), Winter/summer transition in the Antarctic mesopause region, *J. Geophys. Res. Atmos.*, *120*, 12,394–12,409, doi:10.1002/2015JD023928.

Lübken, F.-J., G. Baumgarten, J. Hildebrand, F. J. Schmidlin (2016), Simultaneous and co-located wind measurements in the middle atmosphere by lidar and rocket-borne techniques, *Atmos. Meas. Tech.*, *9*, 3911–2919, doi:10.5194/amt-2016-106.

Lübken, F.-J., R. Latteck, E. Becker, J. Höffner, and D. J. Murphy (2016), Using polar mesosphere summer echoes and stratospheric/mesospheric winds to explain summer mesopause jumps in Antarctica, *J. Atmos. Solar-Terr. Phys.*, *In Press, Corrected Proof, available online 28 July 2016*, doi:10.1016/j.jastp.2016.06.008.

MacDougall, J. W., J. M. C. Plane, P. C. Jayachandran (2000), Polar cap Sporadic-E: part 2, modeling, *J. Atmos. Solar-Terr. Phys.*, *62*, 1169–1176, doi:10.1016/S1364-6826(00)00092-4.

Marsh, D. R., M. J. Mills, D. E. Kinnison, J.-F. Lamarque, N. Calvo, and L. M. Polvani (2013a), Climate Change from 1850 to 2005 Simulated in CESM1(WACCM) *J. Climate*, *26*, 7372–7391, doi:10.1175/JCLI-D-12-00558.1.

Marsh, D. R., D. Janches, W. Feng, and J. M. C. Plane (2013b), A global model of meteoric sodium, *J. Geophys. Res.*, *118*, 11,442–11,452, doi:10.1002/jgrd.50870.

Mayr, H. G., J. G. Mengel, E. R. Talaat, H. S. Porter, and K. L. Chan (2005a), Mesospheric non-migrating tides generated with planetary waves: I. Characteristics, *J. Atmos. Solar-Terr. Phys.*, *67*, 959–980, doi:10.1016/j.jastp.2005.03.002.

Mayr, H. G., J. G. Mengel, E. R. Talaat, H. S. Porter, and K. L. Chan (2005b), Mesospheric non-migrating tides generated with planetary waves: II. Influence of gravity waves, *J. Atmos. Solar-Terr. Phys.*, *67*, 981–991, doi:10.1016/j.jastp.2005.03.003.

McLandress, C. (1998), On the importance of gravity waves in the middle atmosphere and their parameterization in general circulation models, *J. Atmos. Solar-Terr. Phys.*, *60*, 1357–1383, doi:10.1016/S1364-6826(98)00061-3.

McLandress, C. (2002), The Seasonal Variation of the Propagating Diurnal Tide in the Mesosphere and Lower Thermosphere. Part I: The Role of Gravity Waves and Planetary Waves, *J. Atmos. Sci.*, *59*(5), 893–906, doi:10.1175/1520-0469(2002)059<0893:TSVOTP>2.0.CO;2.

Megner, L., and J. Gumbel (2009), Charged meteoric smoke as ice nucei in the mesosphere: Part 2—A feasibility study, *J. Atmos. Solar-Terr. Phys.*, *71*, 1236–1244, doi:10.1016/j.jastp.2009.05.002.

Merkel, A. W., D. R. Marsh, A. Gettelman, and E. J. Jensen (2009), On the relationship of polar mesospheric cloud ice water content, particle radius and mesospheric temperature and its use in multi-dimensional models, *Atmos. Chem. Phys.*, *9*, 8889–8901, doi:10.5194/acp-9-8889-2009.

Mills, M. J., O. B. Toon, V. Vaida, P. E. Hintze, H. G. Kjaergaard, D. P. Schofield, and T. W. Robinson (2005), Photolysis of sulfuric acid vapor by visible light as a source of the polar stratospheric CN layer, *J. Geophys. Res.*, *110*, D08201, doi:10.1029/2004JD005519.

Morris, R. J., D. J. Murphy, I. M. Reid, D. A. Holdsworth, and R. A. Vincent (2004), First polar mesosphere summer echoes observed at Davis, Antarctica (68.6°),*Geophys. Res. Lett.*, *31*, L16111, doi:10.1029/2004GL020352.

Morris, R. J., M. B. Terkildsen, D. A. Holdsworth, and M. R. Hyde (2005), Is there a causal relationship between cosmic noise absorption and PMSE?, *Geophys. Res. Lett.*, *32*, L24809, doi:10.1029/2005GL024568.

Morris, R. J., D. J. Murphy, R. A. Vincent, D. A. Holdsworth, A. R. Klekociuk, and I. M. Reid (2006), Characteristics of the wind, temperature and PMSE field above Davis, Antarctica, *J. Atmos. Solar-Terr. Phys.*, *68*, 418–435, doi:10.1016/j.jastp.2005.04.011.

Morris, R. J., A. R. Klekociuk, R. Latteck, W. Singer, D. A. Holdsworth, and D. J. Murphy (2009), Interhemispheric asymmetry in polar mesosphere summer echoes and temperature at 69° latitude, *J. Atmos. Solar-Terr. Phys.*, *71*, 464–469, doi:10.1016/j.jastp.2008.09.042.

Morris, R. J., J. Höffner, F.-J. Lübken, T. P. Viehl, B. Kaifler, and A. R. Klekociuk (2012), Experimental evidence of a stratospheric circulation influence on mesospheric temperatures and ice-particles during the 2010–2011 austral summer at 69°S, *J. Atmos. Solar-Terr. Phys.*, *89*, 54–61, doi:10.1016/j.jastp.2012.08.007.

Mote, P. W., K. H. Rosenlof, M. E. McIntyre, E. S. Carr, J. C. Gille, J. R. Holton, J. S. Kinnersley, H. C. Pumphrey, J. M. Russell III, and J. W. Waters (1996), An atmospheric tape recorder: The imprint of tropical tropopause temperatures on stratospheric water vapor, *J. Geophys. Res.*, *101*(D2), 3989–4006, doi:10.1029/95JD03422.

Murphy, D. J., J. M. Forbes, R. L. Walterscheid, M. E. Hagan, S. K. Avery, T. Aso, G. J. Fraser, D. C. Fritts, M. J. Jarvis, A. J. McDonald, D. M. Riggin, M. Tsutsumi, and R. A. Vincent (2006), A climatology of tides in the Antarctic mesosphere and lower thermospere, *J. Geophys. Res.*, *111*, D23104, doi:10.1029/2005JD006803.

Murphy, D. J., S. P. Alexander, and R. A. Vincent (2012), Interhemispheric dynamical coupling to the southern mesosphere and lower thermosphere, *J. Geophys. Res.*, *117*, D08114, doi:10.1029/2011JD016865.

Murray, B. J., and J. M.C. Plane (2005), Uptake of Fe, Na and K atoms on low-temperature ice: implications for metal atom scavenging in the vicinity of polar mesospheric clouds, *Phys. Chem. Chem. Phys.*, *7*, 3970–3979, doi:10.1039/b508846a.

Nahar, S. N., M. A. Bautista, and A. K. Pradhan (1997), Electron-ion recombination of neutral iron, *Astrophys. J.*, *479*, 497–503, doi:10.1086/303874.

Neuber, R., P. von der Gathen, and U. von Zahn (1988), Altitude and temperature of the mesopause at 69°N latitude in winter, *J. Geophys. Res.*, *93*, D9, 11093–11101, doi:10.1029/JD093iD09p11093.

Nesvorný, D., P. Jenniskens, H. F. Levison, W. F. Bottke, D. Vokrouhlický, and M. Gounelle (2010), Cometary origin of the zodiacal cloud and carbonaceous micrometeorites. Implications for hot debris disks, *Astrophys. J.*, *713*, 816–836, doi:10.1088/0004-637X/713/2/816.

Nicolls, M. J., R. H. Varney, S. L. Vadas, P. A. Stamus, C. J. Heinselman, R. B. Cosgrove, and M. C. Kelley (2010), Influence of an inertia-gravity wave on mesospheric dynamics: A case study with the Poker Flat Incoherent Scatter Radar, *J. Geophys. Res.*, *115*(D3), D00N02, 2156–2202, doi:10.1029/2010JD014042.

Noll, S., W. Kausch, S. Kimeswenger, S. Unterguggenberger, and A. M. Jones (2015), OH populations and temperatures from simultaneous spectroscopic observations of 25 bands, *Atmos. Chem. Phys.*, *15*, 3647–3669, doi:10.5194/acp-15-3647-2015.

Noll, S., W. Kausch, S. Kimeswenger, S. Unterguggenberger, and A. M. Jones (2016), Comparison of VLT/X-shooter OH and O_2 rotational temperatures with consideration of TIMED/SABER emission and temperature profiles, *Atmos. Chem. Phys.*, *16*, 5021–5042, doi:10.5194/acp-16-5021-2016.

Oberheide, J., Q. Wu, T. L. Killeen, M. E. Hagan, and R. G. Roble (2006), Diurnal nonmigrating tides from TIMED Doppler Interferometer wind data: Monthly climatologies and seasonal variations, *J. Geophys. Res.*, *111*, A10S03, doi:10.1029/2005JA011491.

Pan, W., and C. S. Gardner (2003), Seasonal variations of the atmospheric temperature structure at South Pole, *J. Geophys. Res.*, *108*(D18), 4564, doi:10.1029/2002JD003217.

Pancheva, D., et al. (2002), lobal-Scale tidal structure in the mesosphere and lower Thermosphere during the PSMOS Campaign of June-August 1999 and Comparisons with the global scale wave model, *J. Atmos. Solar-Terr. Phys.*, *64*, 1011–1035, doi:10.1016/S1364-6826(02)00054-8.

Pedatella, N. M., K. Raeder, J. L. Anderson, and H.-L. Liu (2014), Ensemble data assimilation in the Whole Atmosphere Community Climate Model, *J. Geophys. Res.*, *119*, 9793–9809, doi:10.1002/2014JD021776.

Picone, J. M., A. E. Hedin, D. P. Drob, and A. C. Aikin (2002), NRLMSISE-00 empirical model of the atmosphere: Statistical comparisons and scientific issues, *J. Geophys. Res.*, *107*(A12), 1468, doi:10.1029/2002JA009430.

Pignalberi, A., M. Pezzopane, and E. Zuccheretti (2014), Sporadic E layer at mid-latitudes: average properties and influence of atmospheric tides, *Ann. Geophys.*, *32*, 1427–1440, doi:10.5194/angeo-32-1427-2014.

Plane, J. M. C. (1991), The chemistry of meteoric metals in the Earth's upper atmosphere, *Int. Rev. Phys. Chem.*, *10*(1), 55–106, doi:10.1080/01442359109353254.

Plane, J. M. C., R. M. Cox, and R. J. Rollason (1999), Metallic Metal Layers in the Mesopause and Lower Thermosphere Region, *Adv. Space Res.*, *24*(11), 1559–1570, doi:10.1016/S0273-1177(99)00880-7.

Plane, J. M. C. (2003), Atmospheric Chemistry of Meteoric Metals, *Chem. Rev.*, *103*(12), 4963–4984, doi:10.1021/cr0205309.

Plane, J. M. C. (2004), A time-resolved model of the mesospheric Na layer: constraints on the meteor input function, *Atmos. Chem. Phys.*, *4*(3), 627–638, doi:10.5194/acp-4-627-2004.

Plane, J. M. C., B. J. Murray, X. Chu, and C. S. Gardner (2004), Removal of Meteoric Iron on Polar Mesospheric Clouds, *Science*, *304*, *16 April 2005*, 426–428.

Plane, J. M. C. (2012), Cosmic dust in the earth's atmosphere, *Chem. Soc. Rev.*, *41*, 6507–6518, doi:10.1039/c2cs35132c.

Plane, J. M. C., W. Feng, E. M. C. Dawkins, M. P. Chipperfield, J. Höffner, D. Janches, and D. R. Marsh (2014), Resolving the strange behavior of extraterrestrial potassium in the upper atmosphere, *Geophys. Res. Lett.*, *41(13)*, 4753–4760, doi:10.1002/2014GL060334.

Plane, J. M. C., W. Feng, and E. M. C. Dawkins (2015), The Mesosphere and Metals: Chemistry and Changes, *Chem. Rev.*, *115(10)*, 4497–4541, doi:10.1021/cr500501m.

Raizada, S., M. Rapp, F.-J. Lübken, J. Höffner, M. Zecha, and J. M. C. Plane (2007), Effect of ice particles on the mesospheric potassium layer at Spitsbergen (78°N), *J. Geophys. Res.*, *112*, D08307, doi:10.1029/2005JD006938.

Rapp, M., and F.-J. Lübken (2004), Polar mesosphere summer echoes (PMSE): review of observations and current understanding, *Atmos. Chem. Phys.*, *4*, 2601–1633, doi:10.5194/acp-4-2601-2004.

Rapp, M., and G. E. Thomas (2006), Modeling the microphysics of mesospheric ice particles: Assessment of current capabilities and basic sensitivities, *J. Atmos. Solar-Terr. Phys.*, *68*, 715–744, doi:10.1016/j.jastp.2005.10.015.

Rapp, M., J. M. C. Plane, B. Strelnikov, G. Stober, S. Ernst, J. Hedin, M. Friedrich, and U.-P. Hoppe (2012), In situ observations of meteor smoke particles (MSP) during the Geminids 2010: constraints on MSP size, work function and composition, *Ann. Geophys.*, *30*, 1661–1673, doi:10.5194/angeo-30-1661-2012.

Rees, M. H. (1989), *Physics and chemistry of the upper atmosphere*, Camebridge University Press, ISBN 0-521-32305-3.

Ridder, C., G. Baumgarten, J. Fiedler, F.-J. Lübken, and G. Stober (2016), Analysis of small-scale structures in lidar observations of noctilucent clouds, *J. Atmos. Solar-Terr. Phys.*, *submitted*.

Rienecker, M. M., et al. (2011), MERRA: NASA's Modern-Era Retrospective Analysis for Research and Applications, *J. Climate*, *24*, 3624–3648, doi:10.1175/JCLI-D-11-00015.1.

Rietmeijer, F. J. M. (2001), Identification of Fe-rich meteoric dust, *Planet. Space Sci.*, *49*, 71–77, doi:10.1016/S0032-0633(00)00094-5.

Rollason, R. J., and J. M. C. Plane (1998), A study of the reactions of Fe^+ with O_3, O_2 and N_2, *J. Chem. Soc. Faraday Trans.*, *94*, 3067–3075, doi:10.1039/A805140B.

Rollason, R. J., and J. M. C. Plane (2000), The reactions of FeO with O_3, H_2, H_2O, O_2 and

CO_2, *Phys. Chem. Chem. Phys.*, *2*, 2335–2343, doi:10.1039/B000877J.

Rumminger, M. D., D. Reinelt, V. Babushok, and G. T. Linteris (1999), Numerical study of the inhibition of premixed and diffusion flames by iron pentacarbonyl, *Combust. Flame*, *116(1-2)*, 207–219, doi:10.1016/S0010-2180(98)00033-9.

Russell III, J. M., S. M. Bailey, L. L. Gordley, D. W. Rusch, M. Horanyi, M. E. Hervig, G. E. Thomas, C. E. Randall, D. E. Siskind, M. H. Stevens, M. E. Summers, M. J. Taylor, C. R. Englert, P. J. Espy, W. E. McClintock, and A. W. Merkel (2009), The Aeronomy of Ice in the Mesosphere (AIM) mission: Overview and early science results, *J. Atmos. Solar-Terr. Phys.*, *71*, 289–299, doi:10.1016/j.jastp.2008.08.011.

Rutherford, J. A., and D. A. Vroom (1972), Formation of iron ions by charge transfer, *J. Chem. Phys.*, *57*, 3091, doi:10.1063/1.1678724.

Saunders, R. W., and J. M. C. Plane (2003), A laboratory study of meteor smoke analogues: Composition, optical properties and growth kinetics, *J. Atmos. Solar-Terr. Phys.*, *68*, 2182–2202, doi:10.1016/j.jastp.2006.09.006.

Saunders, R. W., O. Möhler, M. Schnaiter, S. Benz, R. Wagner, H. Saathoff, P. J. Connolly, R. Burgess, B. J. Murray, M. Gallagher, R. Wills, and J. M. C. Plane (2010), An aerosol chamber investigation of the heterogeneous ice nucleating potential of refractory nanoparticles, *Atmos. Chem. Phys.*, *10*, 1227–1247, doi:10.5194/acp-10-1227-2010.

Saunders, R. W., S. Dhomse, W. S. Tian, M. P. Chipperfield, and J. M. C. Plane (2012), Interactions of meteoric smoke particles with sulphuric acid in the Earth's stratosphere, *Atmos. Chem. Phys.*, *12*, 4387–4398, doi:10.5194/acp-12-4378-2012.

Scalmani, G., M. J. Frisch, B. Menucci, J. Tomasi, R. Cammi, and V. Barone (2006), Geometries and properties of excited states in the gas phase and in solution: Theory and application of a time-dependent density functional theory polarizable continuum model, *J. Chem. Phys.*, *124(9):094107*, doi:10.1063/1.217325.

Scharringhausen, M., A. C. Aikin, J. P. Burrows, and M. Sinnhuber (2008), Global column density retriebals of mesospheric and thermospheric Mg I and Mg II from SCIAMACHY limb and nadir radiance data, *J. Geophys. Res.*, *113*, D13303, doi:10.1029/2007JD009043.

Schmitz, S. (1994), Entwicklung eines schmalbandigen und durchstimmbaren Alexandrit Lasers für ein mobiles Na-Temperatur-Lidar, *Dissertation*, University of Bonn, Germany.

Schmitz, S., U. von Zahn, J. C. Walling, and D. Heller (1995), Alexandrite lasers for temperature sounding of the sodium layer, *12th ESA Symposium on European rocket and balloon programmes and related research*, Edited by T. A. Blix.

Schöch, A., G. Baumgarten, and J. Fiedler (2008), Polar middle atmosphere temperature climatology from Rayleigh lidar measurements at ALOMAR (69°N), *Ann. Geophys.*, *26*, 1681–1698, doi:10.5194/angeo-26-1681-2008.

Schröder, D. (2008), Gaseous Rust: Thermochemistry of Neutral and Ionic Iron Oxides and Hydroxides in the Gas Phase, *J. Phys. Chem. A*, *112*, 13215–13224, doi:10.1021/jp8030804.

Schumann, U. (*Editor*) (2012), *Atmospheric Physics*, Research Topics in Aerospace, Springer-Verlag Berlin Heidelberg, ISBN 978-3-642-30182-7, doi:10.1007/978-3-642-30183-4.

Schwartz, M. J., et al. (2008), Validation of the Aura Microwave Limb Sounder temperature and geopotential height measurements, *J. Geophys. Res.*, *113*(D15S11), 2156–2202, doi:10.1029/2007JD008783.

Self, D. E., and J. M. C. Plane (2003), A kinetic study of the reactions of iron oxides and hydroxides relevant to the chemistry of iron in the upper mesosphere, *Phys. Chem. Chem. Phys.*, *5*(7), 1407–1418, doi:10.1039/b211900e.

Senf, F., and U. Achatz (2011), On the impact of middle-atmosphere thermal tides on the propagation and dissipation of gravity waves, *J. Geophys. Res.*, *116*, D24110, doi:10.1029/2011JD015794.

She, C. Y., J. R. Yu, and H. Chen (1993), Observed thermal structure of a midlatitude mesopause, *Geophys. Res. Lett.*, *20*(7), 567–570, doi:10.1029/93GL00808.

She, C. Y., B. P. Williams, P. Hoffman, R. Latteck, G. Baumgarten, J. D. Vance, J. Fiedler, P. Acott, D. C.

Fritts, and F.-J. Lübken (2006), Simultaneous observations of sodium atoms, NLC and PMSE in the summer mesopause region above ALOMAR, Norway (69°N, 12°E), *J. Atmos. Solar-Terr. Phys.*, *68*, 93–101, doi:10.1016/j.jastp.2005.08.014.

Shepherd, M., and C. Fricke-Begemann (2004), Study of the tidal variations in mesospheric temperature at low and mid latitudes from WINDII and potassium lidar observations, *Ann. Geophys.*, *22*, 1513–1528, doi:10.5194/angeo-22-1513-2004.

Simonich, D. M., and B. R. Clemesha (1983), Resonant extinction of lidar returns from the alkali metal layers in the upper atmosphere, *Appl. Opt.*, *22*(9), 1387–1389, doi:10.1364/AO.22.001387.

Sinnhuber, M., H. Nieder, and N. Wieters. (2012), Energetic Particle Precipitation and the Chemistry of the Mesosphere/Lower Thermosphere, *Surv. Geophys.*, *33*, 1281–1334, doi:10.1007/s10712-012-9201-3.

Siskind, D. E., S. D. Eckermann, J. P. McCormack, M. J. Alexander, and J. T. Bacmeister (2003), Hemispheric differences in the temperature of the summertime stratosphere and mesosphere, *J. Geophys. Res.*, *108*(D2), 4051, doi:10.1029/2002JD002095.

Slipher, V. M. (1929), Emissions in the spectrum of the light of the night sky, *Publ. Astron. Soc. Pacific*, *41*, 262–265.

Smith, A. K. (2003a), The origin of stationary planetary waves in the upper mesosphere, *J. Atmos. Sci.*, *60*, 3033–3041, doi:10.1175/1520-0469(2003)060<3033:TOOSPW>2.0.CO;2.

Smith, A. K. (2012), Global Dynamics of the MLT, *Surv. Geophys.*, *33*, 1177–1230, doi:10.1007/s10712-012-9196-9.

Smith, A. K., D. R. Marsh, A. C. Szymczak (2003b), Interaction of chemical heating and tides in the mesosphere, *J. Geophys. Res.*, *108*(D5), 4164, doi:10.1029/2002JD002664.

Stevens, M. H., L. E. Deaver, M. E. Hervig, J. M. Russell III, D. E. Siskind, P. E. Sheese, E. J. Llewellyn, R. L. Gattinger, J. Höffner, and B. T. Marshall (2012), Validation of upper mesospheric and lower thermospheric temperatures measured by the Solar Occultation for Ice Experiment, *J. Geophys. Res*, *117*, D16304, doi:10.1029/2012JD017689.

Suzuki, S., F.-J. Lübken, G. Baumgarten, N. Kaifler, R. Eixmann, B. P. Williams, T. Nakamura (2013), Vertical propagation of a mesoscale gravity wave from the lower to the upper atmosphere, *J. Atmos. Solar-Terr. Phys.*, *97*, 29–36, doi:10.1016/j.jastp.2013.01.012.

Teiser, G., and C. von Savigny (2016), Variability of OH(3-1) and OH(6-2) emission altitude and volume emission rate from 2003 to 2011, *submitted to J. Atmos. Solar-Terr. Phys.*.

Thayer, J. P., and W. Pan (2006), Lidar observations of sodium density depletions in the presence of polar mesospheric clouds, *J. Atmos. Solar-Terr. Phys.*, *68*, 85–92, doi:10.1016/j.jastp.2005.08.012.

Thomas, G. E. (1991), Mesospheric clouds and the physics of the mesopause region, *Rev. Geophys.*, *29*(4), 553–575, doi:10.1029/91RG01604.

Thomas, G. E. (1996), Is the polar mesosphere the miner's canary of global change?, *Adv. Space Res.*, *18*(3), (3)149–(3)158, doi:10.1016/0273-1177(95)00855-9.

Tobiska, W. K., T. Woods, F. Eparvier, R. Viereck, L. Floyd, D. Bouwer, G. Rottman, and O. R. White (2000), The SOLAR2000 empirical solar irradiance model and forecast tool, *J. Atmos. Solar-Terr. Phys.*, *62*, 1233–1250, doi:10.1016/S1364-6826(00)00070-5.

Turco, R. P., O. B. Toon, R. C. Whitten, R. G. Keesee, and D. Hollenbach (1982), Noctilucent clouds: simulation studies of their genesis, properties and global influences, *Planet. Space Sci.*, *30*(11), 1147–1181, doi:10.1016/0032-0633(82)90126-X.

van de Hulst, H. C. (1981), *Light Scattering by Small Particles*, Dover Publications, Inc., unabridged corrected republication of the work originally published in 1957 by John Wiley & Sons, Inc., ISBN 0-486-64228-3.

Viehl, T. P., (2010), Spektral hochaufgelöste Messungen von Aerosolen in der mittleren Atmosphäre, *Diplomarbeit*, University of Rostock, Germany.

Viehl, T. P., J. Höffner, F.-J. Lübken, J. M. C. Plane, B. Kaifler, and R. J. Morris (2015), Summer time Fe depletion in the Antarctic mesopause region, *J. Atmos. Solar-Terr. Phys.*, *127*, 97–102, doi:10.1016/j.jastp.2015.04.013.

Viehl, T. P., J. M. C. Plane, W. Feng, and J. Höffner (2016a), The photolysis of FeOH and its effect on the bottomside of the mesospheric Fe layer, *Geophys. Res. Lett.*, *43*, 1373–1381, doi:10.1002/2015GL067241.

Viehl, T. P., J. Höffner, F.-J. Lübken, J. M. C. Plane, B. Kaifler, and R. J. Morris (2016b), Corrigendum to "Summer time Fe depletion in the Antarctic mesopause region", *J. Atmos. Solar-Terr. Phys.*, *142*, 150–151, doi:10.1016/j.jastp.2016.02.001.

Vondrak, T., K. R. Woodcock, and J. M. C. Plane (2006), A kinetic study of the reactions of Fe^+ with N_2O, N_2, O_2, CO_2 and H_2O, an the ligand switching reactions $Fe^+ \cdot X + Y \longrightarrow Fe^+ \cdot Y + X$ (X=N_2, O_2, CO_2; Y=O_2, H_2O), *Phys. Chem. Chem. Phys.*, *8*, 503–512, doi:10.1039/B508922K.

Vondrak, T., J. M. C. Plane, S. Broadley, and D. Janches (2008), A chemical model of meteoric ablation, *Atmos. Chem. Phys.*, *8*, 7015–7031, doi:10.5194/acp-8-7015-2008.

von der Gathen, P. (1990), Sättigungseffekte bei Messungen mit einem Na-Temperatur-Lidar sowie Temperaturen und Schwerewellenaktivität in der polaren Hochatmosphäre, *Dissertation*, University of Bonn, Germany.

von Zahn, U., and J. Höffner (1996a), Mesopause temperature profiling by potassium lidar, *Geophys. Res. Lett.*, *23*(2), 141–144, doi:10.1029/95GL03688.

von Zahn, U., J. Höffner, V. Eska, and M. Alpers (1996b), The mesopause altitude: Only two distinctive levels worldwide?, *Geophys. Res. Lett.*, *23*(22), 3231–3234, doi:10.1029/96GL03041.

von Zahn, U., and J. Höffner, and W. J. McNeil (2002), Meteor Trails as studied by ground-based Lidar, in *Meteors in the Earth's Atmosphere*, ed. E. Murad and I. P. Williams, Cambridge University Press, 149–187, ISBN 978-0-521-80431-8.

Wilson, R., M. L. Chanin, A. Hauchercorne (1991), Gravity waves in the middle atmosphere observed by Rayleigh lidar: 2. Climatology, *J. Geophys. Res.*, *93*(D3), 5169–5183, doi:10.1029/90JD02610.

Woodcock, K. R., T. Vondrak, S. R. Meech, and J. M. C. Plane (2006), A kinetic study of the reactions $FeO^+ + O$, $Fe^+ \cdot N_2 + O$, $Fe^+ \cdot O_2 + O$ and $FeO^+ + CO$: Implications for sporadic *E* layers in the upper atmosphere, *Atmos. Chem. Phys.*, *8*, 7015–7031, doi:10.1039/b518155k.

Woodman, R. F., B. B. Balsely, F. Aquino, L. Flores, E. Vazquez, M. Sarango, M. M. Huaman, and H. Soldi (1999), First observations of polar mesosphere summer echoes in Antarctica, *J. Geophys. Res.*, *104*(A10), 22,577–22,590, doi:10.1029/1999JA90226.

Yamashita, C., X. Chu, H.-L. Liu, P. J. Espy, G. J. Nott, and W. Huang (2009), Stratospheric gravity wave characteristics and seasonal variations observed by lidar at the South Pole and Rothera, Antarctica, *J. Geophys. Res.*, *114*, D12101, doi:10.1029/2008JD011472.

Yanai, T., D. Tew, and N. C. Handy (2004), A new hybrid exchange-correlation functional using the Coulomb-attenuating method (CAM-B3LYP), *Chem. Phys. Lett.*, *292*, 51–57, doi:10.1016/j.cplett.2004.06.011.

Yu, Z., X. Chu, W. Huang, W. Fong, and B. R. Roberts (2012), Seasonal variations of the Fe layer in the mesosphere and lower thermosphere: Four season variability and solar effects on the layer bottomside at McMurdo (77.8°S, 166.7°E), Antarctica, *J. Geophys. Res.*, *117*, D22303, doi:10.1029/2012JD018079.

Zhang, F. (2004), Generation of Mesoscale Gravity Waves in Upper-Tropospheric Jet-Front Systems, *J. Atmos. Sci.*, *61*, 440–457, doi:10.1175/1520-0469(2004)061<0440:GOMGWI>2.0.CO;2.

Zhang, X., J. M. Forbes, and M. E. Hagan (2010), Longitudinal variation of tides in the MLT region: 2. Relative effects of solar radiative and latent heating, *J. Geophys. Res.*, *115*, A06317, doi:10.1029/2009JA014898.

Zhou, Q., S. Raizada, C. A. Tepley, and J. M. C. Plane (2008), Seasonal and diurnal variation of electron and iron concentrations at the meteor heights above Arecibo, *J. Atmos. Solar-Terr. Phys.*, *70*, 49–60, doi:10.1016/j.jastp.2007.09.012.

Acknowledgment

The lidar observations and the expedition to Antarctica were funded by the Leibniz-Institute of Atmospheric Physics (IAP) and the Australian Antarctic Division (AAD) under projects No 2325 *"VHF Radar Studies of the Antarctic Mesosphere, Stratosphere and Troposphere"* and No 4025 *"Gravity wave drag parameterization in climate models"*. Analyses of lidar observations were co-funded by the Leibniz Association under project *"Mixing and Transport in the Mesosphere/Lower Thermosphere"* (MaTMeLT). Publications were partly supported by Australian Antarctic science projects No 674 *"Dynamical coupling in the Antarctic middle atmosphere"* and No 737 *"Lidar studies of atmospheric dynamics, composition and climatology"*, the *"Trends in the Middle Atmosphere"* (TIMA) project of the BMBF research initiative *"Role of the Middle Atmosphere in Climate"* (ROMIC), and the *"Processes and Climatology of Gravity Waves"* (PACOG) project of the DFG. The modelling work was funded by ERC grant No 291332 *"Cosmic Dust in the Terrestrial Atmosphere"* (CODITA).

I thank Prof. Franz-Josef Lübken for offering and supervising my doctoral research position, for initiating the successful collaboration with the AAD under which most of the results presented in this thesis have been obtained and which enabled me to visit Antarctica twice for a total of 22 months, and for embedding IAP into a framework of national and international cooperations which allows to work in a stimulating environment among top researchers.

I am most grateful to have been closely working with Dr Josef Höffner, who has not only designed and built the main parts of our instrument, written most of the code to analyse the data, worked around the clock to keep the project going, and has always been an endless fountain of knowledge. He has also constantly been available to help solve urgent or not so urgent problems, especially while being on the other side of the world during my 2012 winter at Davis, answering the phone or emails even at 3 am on a Sunday morning. The measurement campaigns and this thesis would not have been possible without Josef. Thank you for all your work and friendship.

Science is a collaborative effort, and the contribution of those in the background is often overlooked. I thank all colleagues at IAP for a harmonious and productive work environment, scientific input, and long discussions at the lunch table. I especially thank all members of the Optical Soundings Department for their cooperative attitude and friendship. I want to emphasise the role of all technical and administrative staff, supporting the maintenance and further development of the instrument and prioritising yet another urgent order for spare parts placed at the last minute. I particularly thank Torsten Köpnick for years of developments on the mobile IAP Fe lidar's electronics systems, and Michael Priester for helping out with all forgotten and unplanned tasks and errands.

The scientific campaign in Antarctica would not have been successful without the relentless efforts of many unsung heroes working in administrative and supportive roles at the AAD and on board the RSV Aurora Australis. I want to express my gratitude for all your contributions. I especially thank the members of the "Antarctica and the Global System" aka "Climate Processes and Change" aka "Atmospheric and Space Physics" group Dr Ray J. Morris, Dr Andrew R. Klekociuk, Dr Damian J. Murphy, Dr W. John R. French, and Dr Simon P. Alexander for welcoming us into their team, making the joint measurements possible, and for happily helping out with many smaller and larger problems. I also thank Dr Ray J. Morris and Dr Bernd Kaifler for supporting and continuing the measurements throughout the 2011 winter.

I thank all expeditioners of the 64th – 66th Australian National Antarctic Research Expeditions who have made the campaign possible, helped out with uncountable little things, and have made Antarctica genuinely feel like home — especially Ashley Miskelly, Charmaine Alford, Hannah Taylor, and the 2012 winterers at Davis: Adam Christensen, Dr Alison Dean, Brigid Dwyer, Cathie Young, Chris Hill, Darryl Seidel, Emily, Greg Wilson, Dr Jan Wallace, Joseph Glacken, Jose Campos, Lincoln Mainsbridge, Mark Baker, Mark Coade, Melanie Ho, Dr Nick Chang, Rob Cullen, Scott Beardsley, Stephanie MacDonald, Steve Edwards, and Tom Luttrell. You truly became a second family during this memorable time. Let us also remember those who have suffered injury or died for the scientific expeditions to Antarctica, in particular our dear friends Bob Heath, Mike Denton, and Perry Anderson.

I thank Raimund Wörl, Rory MacDougall, and the staff of the Andøya Space Center in Andenes, Norway for their help in setting up the mobile IAP Fe lidar at ALOMAR. I thank the ALOMAR staff, Dr Josef Höffner, Raimund Wörl, and several summer students for their work to maintain the instrument and continue the measurements in the Arctic.

Science thrives from the exchange of knowledge and interdisciplinary approaches. I thank all members of Prof. John M. C. Plane's Atmospheric and Planetary Chemistry group at the University of Leeds for warmly welcoming me as their guest on several occasions. I further thank the School of Earth and Environment at the University of Leeds and the NCAS for hosting me during my stay. I especially thank Prof. John M. C. Plane and Dr Wuhu Feng for most valuable discussions about Fe chemistry and atmospheric modelling.

Any big pile of words comes with a bunch of errors and confusions. I thank Dr Josef Höffner, Dr Alison Dean, Dr Erin C. M. Dawkins, Mark Baker, Dr Jens Hildebrand, Dr Jeff Cumpston, Raimund Wörl, Dr Michael Gerding, and Dr Gerd Baumgarten for proofreading and valuable comments on this thesis. Peter Schubert and Dr Jens Hildebrand have developed the source code for the LaTeX-layout. I further thank all co-authors as well as the anonymous reviewers at *Geophysical Research Letters*, the *Journal of Geophysical Research*, and the *Journal of Atmospheric and Solar-Terrestrial Physics* for their contribution and input to the papers of this thesis.

I am grateful for a very supportive family and a great mob of friends who have shared many adventures in Europe, Australia, and Antarctica. Thank you for helping me to keep my sanity with endlessly engaging discussions about sports, arts, gardening, good coffee, and all other truly meaningful things in life.

Finally, I am most grateful for my partner Anna-Christina who has borne nearly all of the weight of looking after our daughter Caroline while giving me as much time as possible to work on this thesis. Thank you for being the most supportive, mindful, and happy best friend anyone could hope for. And Caroline: your desire to explore the world and your boundless joy make me smile every single day.

Timo P. Viehl
October 2016